博士論文

# Development of Label-free Molecule Detection Method for Nanofluidics and Realization of Analytical Device Using $10^1$ nm Space

# （ナノ流体デバイスにおける無標識分子検出法の開発と $10^1$ nm 空間を利用した極限分析デバイスの実現）

Yoshiyuki Tsuyama

津山　慶之

School of Engineering
The University of Tokyo

# Contents

# Chapter 1. Introduction

## 1.1 Background

### 1.1.1 Micro/Nanofluidic Device

*Development of Microfluidics*

The advent of microfluidic devices (microfluidics) which miniaturize and integrate conventional experimental procedures such as mixing, reaction, separation, and detection in a palm-top-sized chip revolutionized chemical/biological analyses.[1,2] The history of microfluidics dates back to over 40 years ago. In 1979, S. C. Terry et.al realized a miniaturized gas chromatography system on a silicon wafer for the first time, although it was a "gas fluidic" device.[3] In 1990, A. Manz et.al for the first time realized a high-pressure liquid chromatography system in a silicon and glass device and proposed the concept of miniaturized total analysis system (μ-TAS) which enables high reaction/separation efficiency, fast analysis time, and small consumption of reagents.[4,5] With the progress of fabrication technology, the concept of μ-TAS attracted much attention from researchers. Several miniaturized chemical/biological analyses have been developed in the 1990's such as electrophoretic separation, polymerase chain reaction, and DNA sequencing by several groups: A. Manz, D. Jed Harrison, M. Ramsay, S. Quake, and R. A. Mathies.[6–11]

After the establishment of microfluidics, there have been two major advancements in this research field: device materials and integration methodologies. As a material for microfluidics, silicon and glass were mainly used in the early days of microfluidics. However, the fabrication process was complicated and expensive. To overcome these problems, G. Whitesides and other researchers developed polymer-based microfluidic devices, especially Polydimethylsiloxane (PDMS).[12–14] The advantage of PDMS such as easy fabrication, optically transparent, deformability, and easy surface modification

lowered the threshold of microfluidics and greatly expanded the field. As a further cost-effective and simple microfluidics, functionalized papers were also developed as a substrate to construct disposable microfluidic devices for use in rapid diagnostic tests.[15–17] In this concept, hydrophilic/hydrophobic patterned papers work as analytical devices. The simple and cheap analytical devices are suitable for mass production and have opened up the commercial use of microfluidics.[18,19]

Another part of advancement is the integration methodologies of several chemical/biological processes on a chip. In 2002, T. Kitamori et.al proposed the concept of continuous-flow chemical processing (CFCP) as shown in Fig. 1-1.[20] In the concept of CFCP, each bulk chemical process such as mixing, reaction, and extraction was miniaturized by microfabrication technologies as micro-unit operation (MUO). Then, these MUOs were integrated on a chip and connected by a pressure-driven fluidic control system. The concept of CFCP enabled complex chemical/ biological analyses on

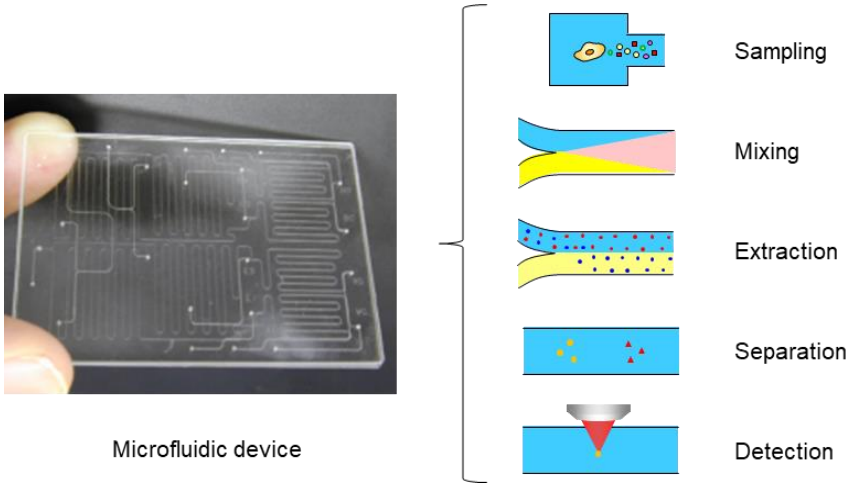


*Figure 1-1. Concept of continuous flow chemical processing (CFCP). Bulk scale chemical processes are miniaturized and integrated into a microfluidic device.*

microfluidic devices. For example, the solvent extraction of metal ions was performed by multiple-phase flow formed in microchannels. Another approach of system integration is segmented-flow microfluidics. In this approach, water droplets in oil or air work as a separator, container, reaction chamber, and so on.[21,22] Furthermore, microdroplets can be manipulated by utilizing the electro-wetting effect, which is called digital microfluidics.[23,24] The easy handling of multiple small droplets has realized complicated yet high-throughput analyses on microfluidics. Unlike continuous-flow microfluidics, droplet-based microfluidics allows for independent control of each droplet, providing microreactors that can be individually transported, mixed, and analyzed.[25,26] Above integration methodologies enable further complex operations on a single device and expanded the range of applications.

With the advancement of device materials and integration methodologies, several notable techniques and applications of microfluidics have been developed in the last few years. For example, C.T Lim et.al realized label-free isolation of circulating tumor cells from blood by utilizing spiral microfluidics.[27] Due to inertial and Dean drag forces in a spiral microfluidic device, larger circulating tumor cells were focused apart from the smaller blood cells. M. He et.al developed a multiplexed exosome detection chip for cancer diagnosis.[28] By the integration of continuous-flow mixing, immune-magnetic isolation, and immunoassay, they realized multiplexed detection of the three tumor proteins in 20 μL of human plasma within 40 minutes. D. A. Weitz et.al developed droplet barcoding for single-cell transcriptomics.[29] Each cell was encapsulated in droplets with hydrogels containing barcoded DNA primers. After cell lysis, reverse transcription reaction, and linear amplification, single-cell sequence and analysis were realized. A. Koh et.al developed a wearable microfluidic sensor for sensing sweat.[30] By wireless

communication electronics and colorimetric sensing, they realized quantitation of sweat rate, total sweat loss, pH, and concentration of chloride and lactate. As described above, microfluidics has been unleashing its potential in response to the rising demand for chemical, biological, medical, and diagnostic tools.[31]

*Development of Nanofluidics*

As the progress of microfluidics, further miniaturization of chemical/biological analyses to $10^2$−$10^3$ nm space has attracted attention, opening the field of nanofluidic devices (Nanofluidics).[32–35] The size of nanochannels is smaller than cells and embraces a wide range of nanoscale objects such as viruses, exosomes, and lipid vesicles. Furthermore, the ultra-high surface to volume ratio enables strong interaction between molecules/nanoparticles and channel wall surface. Thus, nanofluidics provides novel chemical/biological analyses that cannot be realized in microfluidics.

The development of nanofluidics has proceeded with the progress of fabrication technologies such as electron beam lithography, nanoimprint lithography, focused ion etching, and surface modification.[36,37] Furthermore, fluidic control systems such as flow injector, valves, and pumps for nanofluidics has been developed for the manipulation of the ultra-small volume of samples in nanochannels.[38–40] Utilizing the advantage of nanofluidics, novel chemical/biological processing at pL−fL sample volume has been realized. For example, P. E. Boukany et.al realized the delivery of precise amounts of biomolecules into living cells by nanochannels.[41] By applying the electric field to a nanochannel, transfection agents were electrophoretically carried to the cell cytoplasm via the nanochannel without affecting cell viability. L. Lin et.al realized sampling from a single living cell by nanochannels.[42] By the fusion of the single cells in single-cell

chambers and vesicle-modified nanochannels, 39 fL of the cytoplasm of a living single human aortic endothelial cell was realized without killing cells. For separation and purification technologies, R. Ishibashi et.al demonstrated reversed-phase chromatographic separations by nanochannels with 910 nm width and 220 nm depth which walls were modified with ODS.[43] The calculated minimum injection volume was 180 aL, and the theoretical plate number was calculated to be $10^5$ plates/m. Q. Wu et.al realized micro-RNA separation by nanopillars with a 250-nm diameter and 100-nm height.[44] By utilizing nanopillars as sieve matrix, 20 ms and 100 ms isolation of miRNA from DNA fragments and nucleic acids were realized. Y. Kazoe et.al developed a femtoliter solvent extraction system by partial hydrophobic surface modification of nanochannels.[45] Utilizing high surface to volume ratio of nanochannels, lipids and amino acids in 4 fL samples were successfully separated within 1 ms.

Furthermore, several chemical/biological analyses by integrated nanofluidic analytical devices have been realized by the combination of microfluidic technologies and nanofluidic technologies. For example, K. Shirai et.al realized single-molecule ELISA in nanochannels.[46] By more than 1,000 times collision to capture antibody modified on the channel wall surface, target antigens were captured with almost 100% efficiency. By measuring the concentration of colored substrates confined in the nanochannel, signals derived from single or countable antigens were successfully obtained. T. Nakao et.al developed a living single-cell protein analysis device based on micro/nanofluidics.[47] More than 10 unit operations (e.g. cell stimulation, volumetry, enzymatic reaction) were integrated on a single glass substrate, and IL-6 molecules from single B cells were analyzed at the limit of detection of 5.27 molecules. These results show that nanofluidics has the potential to provide chemical/biological analyses at a

single or countable molecular level.

In recent years, the size of nanochannels is reaching $10^1$–$10^2$ nm space due to the further progress of fabrication technologies, and $10^1$ nm fluidic devices have attracted much attention. This size region is almost comparable to DNAs, viruses, and proteins; unique analyses and applications utilizing such ultra-small channels have been demonstrated. For example, J. Han and H. G. Craighead realized the separation of long DNA molecules by the entropic trap array with less than 100 nm depth.[48] By utilizing the difference of interaction between DNA molecules and the entrance of a thin region, longer DNA molecules showed higher mobility in the channel. G. Desmet et.al succeeded in performing chromatographic separations in channels less than 100 nm depth.[49] By the shear-driven flow, a high flow velocity (7 mm/sec) and a high theoretical plate number ($10^3$–$10^4$ plates) were realized. C. Duan et.al realized label-free electrical detection of enzymatic reactions in 50 nm deep nanochannels.[50] By coating poly-L-lysine on the surface of nanochannels, enzymatic reaction of single trypsin molecule was monitored.

In addition to the above applications, several unique liquid phenomena in ultra-small space have been reported. Although it has been revealed that water confined in less than 1 nm space shows unique properties due to the confinement at a single or countable molecular level,[51,52] water confined $10^1$–$10^2$ nm space also shows unique liquid properties such as high proton mobility, low dielectric constant, high viscosity, and ion concentration polarization.[53–57] These unique phenomena are explained by the structure change of molecular assembly and overlap of the electric double layer. These unique phenomena make nanofluidics different from microfluidics and bulk spaces.

The summary of analytical space and micro/nanofluidic devices is shown in Fig. 1-2. As mentioned above, $10^1$–$10^2$ nm space is a novel research area in terms of both

scientific insights and application to chemical/biological analyses. However, it is still in the early stage of development, and numerous challenges remain to be solved. Currently, most $10^1$–$10^2$ nm fluidic devices still focus on a single function or operation which can be accomplished by simple sample introduction and measurement. To fully understand and utilize $10^1$–$10^2$ nm fluidic devices, the implementation of multi-step analytical processes in $10^1$–$10^2$ nm channels is essential. However, integration of multiple functions into $10^1$–$10^2$ nm channels by well-designed nanofluidic circuit and precise fluidic control has yet to be difficult, despite it is the advantage of nanofluidics compared with other nanostructures such as nanopores or nanomembranes.[58,59] For the further development of nanofluidics, a highly sensitive yet versatile detection methodology for nanochannels is essential, which is one of the most important fundamental technologies for chemical/biological analyses.

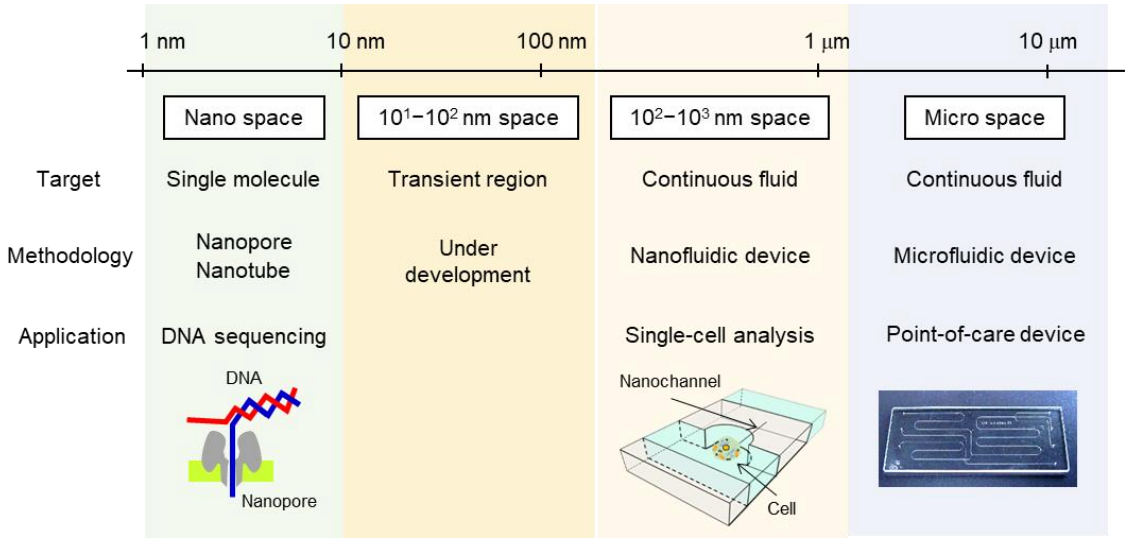


*Figure 1-2.Analytical space and micro/nanofluidic devices.*

### 1.1.2 Detection Technologies for Micro/Nanofluidic Device

*Conventional Detection Technologies*

As described above, micro/nanofluidic devices have attracted much attention in fundamental sciences and applications to chemical/biological analyses. However, molecular detection in ultra-small channels is challenging due to the ultra-small volume and ultra-small number of molecules. For example, 1 nM solution in 1 fL detection volume corresponds to less than a single molecule. Therefore, an ultra-sensitive molecule detection method is essential for micro/nanofluidic devices. Laser-induced fluorescence (LIF) is one of the most widely used molecule detection methods due to the high sensitivity and selectivity. The first report of single-molecule detection by LIF and its application to the ultra-small volume of samples dates back to the 1990s.[60] The detection performance was further improved by several techniques such as confocal systems, total internal reflection fluorescence,[61] and zero-mode waveguides.[62] In recent years, several papers have reported single-molecule detection and observation in micro/nanofluidic devices by LIF.[63] However, few molecules have native-fluorescence, and tedious labeling or tagging procedure is inevitable for a wide range of applications.[64] To tackle this issue, a label-free non-fluorescent molecule/nanoparticle detection method has been developed. Light scattering is a long-standing label-free detection method for micro/nanoparticles and large molecules. By the combination of light scattering detection and interferometric optical systems, M. Piliarik1 and V. Sandoghdar realized single protein molecule observation,[65] and A. Mitra et.al realized the detection and classification of individual viruses flowing in nanochannels.[66] However, the sensitivity and selectivity are still insufficient for a wide range of applications. Resonance-based detection such as surface plasmon resonance (SPR) or micro/nanocavity is also known as sensitive label-free

molecule detection methods.[67,68] In resonance-based detection methods, adsorption of molecules to a sensing area is measured as resonance shift, which provides ultra-sensitive molecule detection at a single-molecule level. A. M. Armani et.al developed a whispering gallery mode waveguide and realized the observation of single protein molecule adsorption to the surface of a ring resonator.[69] Electrical/electrochemical detection is another widely used label-free detection method. For example, C. Duan et.al monitored enzyme reaction in nanochannels by measuring the electrical resistance of nanochannels.[50] By resistive pulse sensing, W. Li et.al detected single protein molecules passing through nanopores.[70] Although the above detection methods realized label-free detection with high sensitivity, these methods require complicated fabrication of nanostructures; a non-invasive yet highly sensitive detection method is strongly required for integrated nanofluidic devices.

*Photothermal spectroscopy (PTS)*

Photothermal spectroscopy (PTS) provides label-free molecule detection without complicated structures or surface adsorption.[71] PTS utilizes light absorption and thermal relaxation by target molecules called "Photothermal effect". A minute temperature change or thermal expansion by heat is selectively measured by frequency-modulated synchronized detection, which enables label-free analyses with high sensitivity. The photothermal effect is common to almost all molecules, thus PTS has wide applicability. Around 1960−1980, several kinds of PTS were developed such as photothermal radiometry, photoacoustic detection, photothermal deflection, and thermal lens detection.[72–75] Around 1980−2000, these methods were applied to various analyses such as chromatography,[76] surface/depth profiling,[77] and evaluation of physical properties.[78] In

recent years, engineered nanomaterials having a suitable photothermal effect for applications have been developed and utilized for photothermal therapy and drug delivery.[79,80] Also, PTS has been utilized for nanoparticle imaging and in vivo imaging.[81,82]

One of the notable PTS for chemical/biological analyses is thermal lens spectroscopy (TLS) which has high sensitivity at a single molecular level.[83] The thermal lens effect was first reported by Gordon et.al in 1965.[84] The principle of the thermal lens effect is as follows. Molecules in the medium absorb the laser with Gaussian intensity distribution, followed by the generation of temperature distribution around the laser focus. The temperature distribution generates refractive index distribution which works like a concave lens against the laser, called “Thermal lens”. Thus, molecules in the medium can be detected by measuring the refraction of the laser. Based on the thermal lens effect, Dovichi et.al established TLS and developed time-resolved mode and dual beam mode (probe and excitation).[85,86] However, the optical setup was large and complicated. In the 1990s, T. Kitamori, T. Sawada, and their coworkers introduced TLS to a microscope and developed a thermal lens microscope (TLM) as shown in Fig.1-3.[87] The TLM realized a simplified setup with a collinear configuration of dual lasers, which further expanded the application of TLS. Kitamori’s group applied the TLM to various analyses utilizing microfluidics such as immunoassay,[88] metal ion extraction,[20] and imaging of cells.[89] The TLM also realized sub-yoctomole Pb(II) octa-ethyl porphyrin detection in a benzene solution, which corresponds to 0.4 molecules in the detection volume of 7 fL.[90] Furthermore, Microchannel-assisted thermal lens spectroscopy was developed as a wavelength-tunable TLM.[91] The difference in thermal properties between a solution and a glass substrate realized the thermal lens effect without focusing the excitation beam.

These results show that PTS is a suitable detection technology for microfluidics.

Although TLM works as a detector for chemical/ biological analyses utilizing microfluidics, it cannot be applied to less than 10 μm channels. The TLM is based on the geometric optics: lens-like refractive index distribution formed in solutions. However, smaller channels hinder the formation of desired temperature distribution by the rapid thermal conduction of a glass substrate, which largely degrades detection performance. To overcome this limitation, Shimizu et.al developed a differential interference contrast thermal lens microscope (DIC-TLM) as shown in Fig.1-3 by the introduction of a differential interference contrast to the TLM.[92] In the DIC-TLM, a probe laser is separated into two beams by a DIC prism. An excitation laser is superposed on one of the probe beams by adjusting the polarization plane. By the photothermal effect of target molecules, a minute phase difference is generated between two probe beams, which is measured as an interference light intensity change at a detection position. The DIC-TLM is based on the wave optics (interference effect) and lens-like refractive index distribution is unnecessary, thus applicable to much smaller channels without the degradation of detection performance. The principle of the DIC-TLM is different from TLM, and this detection technology is also called photothermal optical phase shift (POPS) detection. By the DIC-TLM, label-free protein molecule detection in 21 μm × 900 nm channel was achieved with a limit of detection (LOD) of 600 molecules.[93] The DIC-TLM was also used as a detector for immunoassay and chromatography utilizing $10^2$ nm channels.[46,94] These results show that the DIC-TLM can be applied to sub-micron channels with high sensitivity. However, it was revealed that the sensitivity of DIC-TLM rapidly decreases for smaller channels than 800 nm due to thermal diffusion to glass substrates.[93] The effect of thermal diffusion to glass substrates becomes dominant for smaller channels. For

example, thermal diffusion length at 1 kHz excitation laser modulation is calculated to be almost 7 μm in water, which is one or two orders of magnitude larger than the size of nanochannels. Therefore, most of the heat generated by the photothermal effect does not contribute to the signal. Furthermore, as shown in the next chapter, the thermal diffusion to glass substrates causes a cancelation effect for the DIC-TLM. This physical limitation hinders the DIC-TLM from applying to $10^1$–$10^2$ nm channels. In this way, the lack of versatile detection methodology hinders the development of $10^1$–$10^2$ nm fluidic devices despite the potential for a novel research field. Thus, a novel detection principle that can overcome this limitation and can be applied to $10^1$–$10^2$ nm channels is strongly required.

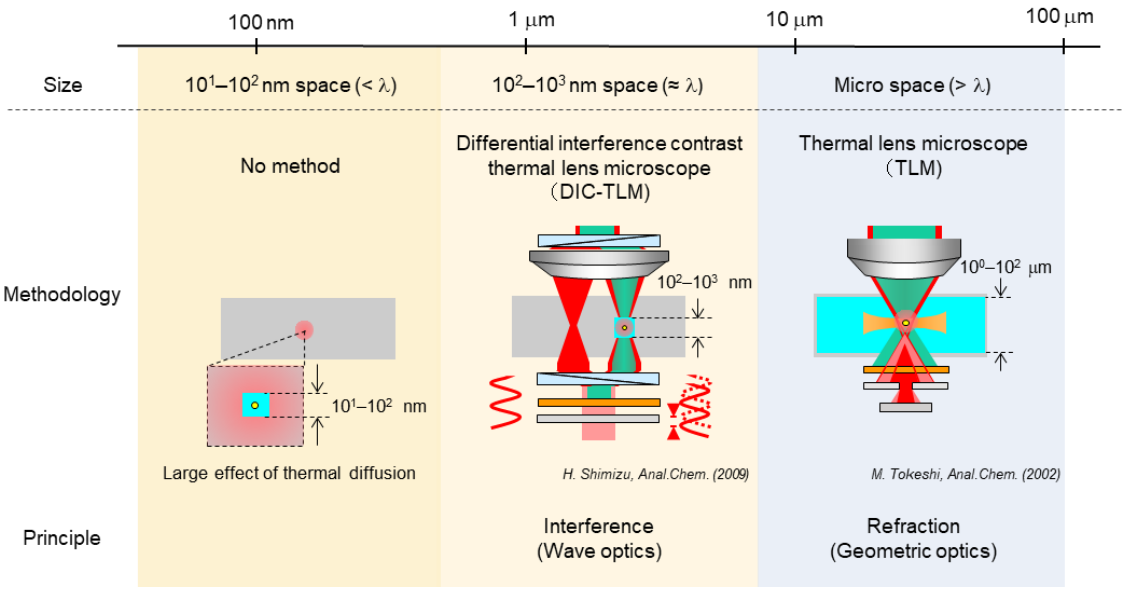


*Figure 1-3. Photothermal detection methods for micro/nano fluidic devices.*

## 1.2 Objectives

This doctoral thesis aims to develop a label-free sensitive molecule/nanoparticle detection method for $10^1$–$10^2$ nm fluidic devices. The objectives of each chapter are described below.

*Proposal and Verification of Photothermal Optical Diffraction (Chapter 2)*

In chapter. 2, a novel photothermal detection method for nanofluidics: photothermal optical diffraction (POD) is developed to overcome the physical limitation of conventional PTS. The detection principle of the POD is proposed, and the experimental setup is constructed. Optical diffraction by a single nanochannel is investigated by theoretical calculations and experiments. The detection principle is verified, and the detection of non-fluorescent molecules in nanochannels is demonstrated. The signal generation mechanism is investigated in detail and elucidated.

*Concentration Determination in $10^1$ nm space (Chapter 3)*

In chapter. 3, concentration determination by the POD is verified, and the detection performance is evaluated. First, experimental conditions of the POD are optimized for the concentration determination. Then, calibration curves for different channel sizes are measured and compared with those for the conventional photothermal detection method (DIC-TLM). Next, the detection performance of the POD is further improved by the solvent enhancement effect. Finally, concentration determination in $10^1$ nm channels is demonstrated.

*Nanoparticle Counting (Chapter 4)*

In chapter 4, detection and characterization of individual nanoparticles in nanochannels is demonstrated by the counting-mode POD. First, the detection principle of the counting-mode POD is verified. Then, experimental conditions are optimized, and the detection performance such as sensitivity and counting efficiency is evaluated. Finally, absorption-based size classification of individual nanoparticles is demonstrated.

*Application to Nanofluidic Analytical Device (Chapter 5)*

In chapter 5, the proof-of-concept for $10^1$ nm fluidic devices is demonstrated by the POD. First, the POD is applied to chemical/biological analyses in $10^2$ nm channels to show its applicability to nanofluidic analytical devices. Enzyme-linked immunosorbent assay and normal-phase chromatography are demonstrated, and the analytical performance is evaluated. Then, separation analysis in $10^1$ nm channels is demonstrated by the integration of sequential analytical processes including pressure-driven pinched injection, normal-phase chromatography, and label-free detection by the POD.

## 1.3 References of Chapter 1


1. Whitesides, G. M. The origins and the future of microfluidics. *Nature* **442**, 368–373 (2006).
2. Arora, A., Simone, G., Salieb-Beugelaar, G. B., Kim, J. T. & Manz, A. Latest developments in micro total analysis systems. *Anal. Chem.* **82**, 4830–4847 (2010).
3. Terry, S. C., Herman, J. H. & Angell, J. B. A Gas Chromatographic Air Analyzer Fabricated on a Silicon Wafer. *IEEE Trans. Electron Devices* **26**, 1880–1886 (1979).
4. Manz, A. *et al.* Design of an Open-tubular Column Liquid Cbromatograpb Using Silicon Chip Technology. *Sensors Actuators B. Chem.* **1**, 249–255 (1990).
5. Manz, A., Graber, N. & Widmer, H. M. Miniaturized Total Chemical Analysis Systems: a Novel Concept for Chemical Sensing. *Sensors Actuators B. Chem.* **1**, 244–248 (1990).
6. Harrison, D. J. *et al.* Micromachining a miniaturized capillary electrophoresis-based chemical analysis system on a chip. *Science.* **261**, 895–897 (1993).
7. Hadd, A. G., Raymond, D. E., Halliwell, J. W., Jacobson, S. C. & Ramsey, J. M. Microchip Device for Performing Enzyme Assays. *Anal. Chem.* **69**, 3407–3412 (1997).
8. Kopp, M. U., De Mello, A. J. & Manz, A. Chemical amplification: Continuous-flow PCR on a chip. *Science.* **280**, 1046–1048 (1998).
9. Li, P. C. H. & Harrison, D. J. Transport, Manipulation, and Reaction of Biological Cells On-Chip Using Electrokinetic Effects. *Anal. Chem.* **69**, 1564–1566 (1997).
10. Chou, H. P., Spence, C., Scherer, A. & Quake, S. A microfabricated device for sizing and sorting DNA molecules. *Proc. Natl. Acad. Sci. U. S. A.* **96**, 11–13 (1999).
11. Woolley, A. T. & Mathies, R. A. Ultra-High-Speed DNA Sequencing Using Capillary Electrophoresis Chips. *Anal. Chem.* **67**, 3676–3680 (1995).
12. Duffy, D. C., McDonald, J. C., Schueller, O. J. A. & Whitesides, G. M. Rapid prototyping of microfluidic systems in poly(dimethylsiloxane). *Anal. Chem.* **70**, 4974–4984 (1998).
13. Mcdonald, J. C., Duffy, D. C., Anderson, J. R. & Chiu, D. T. Review General Fabrication of microfluidic systems in poly ( dimethylsiloxane ). *Electrophoresis*

**21**, 27–40 (2000).
14. Xia, Y. & Whitesides, G. M. Soft lithography. *Annu. Rev. Mater. Sci.* **28**, 153–184 (1998).
15. Martinez, A. W., Phillips, S. T., Butte, M. J. & Whitesides, G. M. Patterned paper as a platform for inexpensive, low-volume, portable bioassays. *Angew. Chemie - Int. Ed.* **46**, 1318–1320 (2007).
16. Yetisen, A. K., Akram, M. S. & Lowe, C. R. Paper-based microfluidic point-of-care diagnostic devices. *Lab Chip* **13**, 2210–2251 (2013).
17. Cate, D. M., Adkins, J. A., Mettakoonpitak, J. & Henry, C. S. Recent developments in paper-based microfluidic devices. *Anal. Chem.* **87**, 19–41 (2015).
18. Chin, C. D., Linder, V. & Sia, S. K. Commercialization of microfluidic point-of-care diagnostic devices. *Lab Chip* **12**, 2118–2134 (2012).
19. Volpatti, L. R. & Yetisen, A. K. Commercialization of microfluidic devices. *Trends Biotechnol.* **32**, 347–350 (2014).
20. Tokeshi, M. *et al.* Continuous-flow chemical processing on a microchip by combining microunit operations and a multiphase flow network. *Anal. Chem.* **74**, 1565–1571 (2002).
21. Teh, S. Y., Lin, R., Hung, L. H. & Lee, A. P. Droplet microfluidics. *Lab Chip* **8**, 198–220 (2008).
22. Guo, M. T., Rotem, A., Heyman, J. A. & Weitz, D. A. Droplet microfluidics for high-throughput biological assays. *Lab Chip* **12**, 2146–2155 (2012).
23. Srinivasan, V., Pamula, V. K. & Fair, R. B. An integrated digital microfluidic lab-on-a-chip for clinical diagnostics on human physiological fluids. *Lab Chip* **4**, 310–315 (2004).
24. Cho, S. K., Moon, H. & Kim, C. J. Creating, transporting, cutting, and merging liquid droplets by electrowetting-based actuation for digital microfluidic circuits. *J. Microelectromechanical Syst.* **12**, 70–80 (2003).
25. Brouzes, E. *et al.* Droplet microfluidic technology for single-cell high-throughput screening. *Proc. Natl. Acad. Sci. U. S. A.* **106**, 14195–14200 (2009).
26. Song, H., Chen, D. L. & Ismagilov, R. F. Reactions in droplets in microfluidic channels. *Angew. Chemie - Int. Ed.* **45**, 7336–7356 (2006).
27. Warkiani, M. E. brahim. *et al.* Ultra-fast, label-free isolation of circulating tumor cells from blood using spiral microfluidics. *Nat. Protoc.* **11**, 134–148 (2016).
28. Zhao, Z., Yang, Y., Zeng, Y. & He, M. A microfluidic ExoSearch chip for multiplexed exosome detection towards blood-based ovarian cancer diagnosis.

*Lab Chip* **16**, 489–496 (2016).
29. Klein, A. M. *et al.* Droplet barcoding for single-cell transcriptomics applied to embryonic stem cells. *Cell* **161**, 1187–1201 (2015).
30. Koh, A. *et al.* A soft, wearable microfluidic device for the capture, storage, and colorimetric sensing of sweat. *Sci. Transl. Med.* **8**, 1–14 (2016).
31. Convery, N. & Gadegaard, N. 30 Years of Microfluidics. *Micro Nano Eng.* **2**, 76–91 (2019).
32. Abgrall, P. & Nguyen, N. T. Nanofluidic devices and their applications. *Anal. Chem.* **80**, 2326–2341 (2008).
33. Napoli, M., Eijkel, J. C. T. & Pennathur, S. Nanofluidic technology for biomolecule applications: A critical review. *Lab Chip* **10**, 957–985 (2010).
34. Mawatari, K., Kazoe, Y., Shimizu, H., Pihosh, Y. & Kitamori, T. Extended-nanofluidics: Fundamental technologies, unique liquid properties, and application in chemical and bio analysis methods and devices. *Anal. Chem.* **86**, 4068–4077 (2014).
35. Xu, Y. Nanofluidics: A New Arena for Materials Science. *Adv. Mater.* **30**, 1–17 (2018).
36. Mijatovic, D., Eijkel, J. C. T. & Van Den Berg, A. Technologies for nanofluidic systems: Top-down vs. bottom-up - A review. *Lab Chip* **5**, 492–500 (2005).
37. Duan, C., Wang, W. & Xie, Q. *Review article: Fabrication of nanofluidic devices*. *Biomicrofluidics* vol. 7 (2013).
38. Ishibashi, R., Mawatari, K., Takahashi, K. & Kitamori, T. Development of a pressure-driven injection system for precisely time controlled attoliter sample injection into extended nanochannels. *J. Chromatogr. A* **1228**, 51–56 (2012).
39. Kneller, A. R., Haywood, D. G. & Jacobson, S. C. AC Electroosmotic Pumping in Nanofluidic Funnels. *Anal. Chem.* **88**, 6390–6394 (2016).
40. Kazoe, Y. *et al.* Femtoliter nanofluidic valve utilizing glass deformation. *Lab Chip* **19**, 1686–1694 (2019).
41. Boukany, P. E. *et al.* Nanochannel electroporation delivers precise amounts of biomolecules into living cells. *Nat. Nanotechnol.* **6**, 747–754 (2011).
42. Lin, L. *et al.* Micro/extended-nano sampling interface from a living single cell. *Analyst* **142**, 1689–1696 (2017).
43. Ishibashi, R., Mawatari, K. & Kitamori, T. Highly efficient and ultra-small volume separation by pressure-driven liquid chromatography in extended nanochannels. *Small* **8**, 1237–1242 (2012).
44. Wu, Q. *et al.* A millisecond micro-RNA separation technique by a hybrid

structure of nanopillars and nanoslits. *Sci. Rep.* **7**, 1–7 (2017).
45. Kazoe, Y., Ugajin, T., Ohta, R., Mawatari, K. & Kitamori, T. Parallel multiphase nanofluidics utilizing nanochannels with partial hydrophobic surface modification and application to femtoliter solvent extraction. *Lab Chip* **19**, 3844–3852 (2019).
46. Shirai, K., Mawatari, K., Ohta, R., Shimizu, H. & Kitamori, T. A single-molecule ELISA device utilizing nanofluidics. *Analyst* **143**, 943–948 (2018).
47. Nakao, T. *et al.* Cytokine analysis on a countable number of molecules from living single cells on nano fl uidic. *Analyst* **144**, 7200–7208 (2019).
48. Han, J. & Craighead, H. G. Separation of long DNA molecules in a microfabricated entropic trap array. *Science.* **288**, 1026–1029 (2000).
49. De Bruyne, S. *et al.* Exploring the speed limits of liquid chromatography using shear-driven flows through 45 and 85 nm deep nano-channels. *Analyst* **138**, 6127–6133 (2013).
50. Duan, C. *et al.* Label-Free Electrical Detection of Enzymatic Reactions in Nanochannels. *ACS Nano* **10**, 7476–7484 (2016).
51. Fumagalli, L. *et al.* Anomalously low dielectric constant of confined water. *Science.* **360**, 1339–1342 (2018).
52. Sugahara, A. *et al.* Negative dielectric constant of water confined in nanosheets. *Nat. Commun.* **10**, 1–7 (2019).
53. Chinen, H. *et al.* Enhancement of proton mobility in extended-nanospace channels. *Angew. Chemie - Int. Ed.* **51**, 3573–3577 (2012).
54. Morikawa, K., Kazoe, Y., Mawatari, K., Tsukahara, T. & Kitamori, T. Dielectric constant of liquids confined in the extended nanospace measured by a streaming potential method. *Anal. Chem.* **87**, 1475–1479 (2015).
55. Li, L., Kazoe, Y., Mawatari, K., Sugii, Y. & Kitamori, T. Viscosity and wetting property of water confined in extended nanospace simultaneously measured from highly-pressurized meniscus motion. *J. Phys. Chem. Lett.* **3**, 2447–2452 (2012).
56. Ahmed, Z., Bu, Y. & Yobas, L. Conductance Interplay in Ion Concentration Polarization across 1D Nanochannels: Microchannel Surface Shunt and Nanochannel Conductance. *Anal. Chem.* **92**, 1252–1259 (2020).
57. Kim, S. J., Wang, Y. C., Lee, J. H., Jang, H. & Han, J. Concentration polarization and nonlinear electrokinetic flow near a nanofluidic channel. *Phys. Rev. Lett.* **99**, 1–4 (2007).
58. Long, Z. *et al.* Recent Advances in Solid Nanopore/Channel Analysis. *Anal. Chem.* **90**, 577–588 (2018).

59. Zhang, Z., Wen, L. & Jiang, L. Bioinspired smart asymmetric nanochannel membranes. *Chem. Soc. Rev.* **47**, 322–356 (2018).
60. Shera, E. B., Seitzinger, N. K., Davis, L. M., Keller, R. A. & Soper, S. A. Detection of single fluorescent molecules. *Chem. Phys. Lett.* **174**, 553–557 (2000).
61. Mashanov, G. I., Tacon, D., Knight, A. E., Peckham, M. & Molloy, J. E. Visualizing single molecules inside living cells using total internal reflection fluorescence microscopy. *Methods* **29**, 142–152 (2003).
62. Uemura, S. *et al.* Real-time tRNA transit on single translating ribosomes at codon resolution. *Nature* **464**, 1012–1017 (2010).
63. Joo, C., Balci, H., Ishitsuka, Y., Buranachai, C. & Ha, T. Advances in Fluorescence Methods for Molecular Biology. *Annu. Rev. Biochem.* **77**, 51–76 (2008).
64. Szöko, É. & Tábi, T. Analysis of biological samples by capillary electrophoresis with laser induced fluorescence detection. *J. Pharm. Biomed. Anal.* **53**, 1180–1192 (2010).
65. Piliarik, M. & Sandoghdar, V. Direct optical sensing of single unlabelled proteins and super-resolution imaging of their binding sites. *Nat. Commun.* **5**, 1–8 (2014).
66. Mitra, A., Deutsch, B., Ignatovich, F., Dykes, C. & Novotny, L. Nano-optofluidic detection of single viruses and nanoparticles. *ACS Nano* **4**, 1305–1312 (2010).
67. Homola, J. Surface plasmon resonance sensors for detection of chemical and biological species. *Chem. Rev.* **108**, 462–493 (2008).
68. Vollmer, F. & Arnold, S. Whispering-gallery-mode biosensing: Label-free detection down to single molecules. *Nat. Methods* **5**, 591–596 (2008).
69. Armani, A. M., Kulkarni, R. P., Fraser, S. E., Flagan, R. C. & Vahala, K. J. Label-free, single-molecule detection with optical microcavities. *Science.* **317**, 783–787 (2007).
70. Li, W. *et al.* Single protein molecule detection by glass nanopores. *ACS Nano* **7**, 4129–4134 (2013).
71. Bialkowski, S. E. *Photothermal Spectroscopy Methods for Chemical Analysis*. (John Wiley & Sons, 1995).
72. Boccara, A. C., Fournier, D. & Badoz, J. Thermo-optical spectroscopy: Detection by the 'mirage effect'. *Appl. Phys. Lett.* **36**, 130–132 (1980).
73. Parker, W. J., Jenkins, R. J., Butler, C. P. & Abbott, G. L. Flash method of determining thermal diffusivity, heat capacity, and thermal conductivity. *J. Appl. Phys.* **32**, 1679–1684 (1961).

74. Kreuzer, L. B. Ultralow gas concentration infrared absorption spectroscopy. *J. Appl. Phys.* **42**, 2934–2943 (1971).
75. Jackson, W. B., Amer, N. M., Boccara, A. C. & Fournier, D. Photothermal deflection spectroscopy and detection. *Appl. Opt.* **20**, 1333–1344 (1981).
76. Yu, M. & Dovichi, N. J. Attomole Amino Acid Determination by Capillary Zone Electrophoresis with Thermooptical Absorbance Detection. *Anal. Chem.* **61**, 37–40 (1989).
77. Milner, T. E., Goodman, D. M., Tanenbaum, B. S. & Nelson, J. S. Depth profiling of laser-heated chromophores in biological tissues by pulsed photothermal radiometry. *J. Opt. Soc. Am. A* **12**, 1479 (1995).
78. Fischer, M. & Georges, J. Fluorescence quantum yield of rhodamine 6G in ethanol as a function of concentration using thermal lens spectrometry. *Chem. Phys. Lett.* **260**, 115–118 (1996).
79. Huang, X., El-Sayed, I. H., Qian, W. & El-Sayed, M. A. Cancer cell imaging and photothermal therapy in the near-infrared region by using gold nanorods. *J. Am. Chem. Soc.* **128**, 2115–2120 (2006).
80. Chen, Q. *et al.* Photothermal therapy with immune-adjuvant nanoparticles together with checkpoint blockade for effective cancer immunotherapy. *Nat. Commun.* **7**, 1–13 (2016).
81. Galanzha, E. I., Kim, J. W. & Zharov, V. P. Nanotechnology-based molecular photoacoustic and photothermal flow cytometry platform for in-vivo detection and killing of circulating cancer stem cells. *J. Biophotonics* **2**, 725–735 (2009).
82. A. Gaiduk, M. Yorulmaz, P. V. Ruijgrok, M. O. Room-Temperature Detection of a Single Molecule's Absorption by Photothermal Contrast. *Science.* **330**, 353–356 (2010).
83. Snook, R. D. & Lowe, R. D. Thermal lens spectrometry. *Analyst* **120**, 2051–2068 (1995).
84. You, A. *et al.* Long-Transient Effects in Lasers with Inserted Liquid Samples. *J. Appl. Phys.* **3**, 3–8 (1964).
85. Dovichl, N. J. & Harris, J. M. Time-resolved thermal lens calorimetry. *Anal. Chem.* **53**, 106–109 (1981).
86. Weimer, W. A. & Dovichi, N. J. Multichannel Crossed-Beam Thermal Lens Measurements for Absolute Absorbance Determination with Pulsed Laser Excitation. *Anal. Chem.* **60**, 662–665 (1988).
87. Harada, M., Iwamoto, K., Kitamori, T. & Sawada, T. Photothermal Microscopy with Excitation and Probe Beams Coaxial Under the Microscope and its

Application to Microparticle Analysis. *Anal. Chem.* **65**, 2938–2940 (1993).
88. Sato, K. *et al.* Microchip-based enzyme-linked immunosorbent assay (microELISA) system with thermal lens detection. *Lab Chip* **4**, 570 (2004).
89. Tamaki, E. *et al.* Single-cell analysis by a scanning thermal lens microscope with a microchip: Direct monitoring of cytochrome c distribution during apoptosis process. *Anal. Chem.* **74**, 1560–1564 (2002).
90. Tokeshi, M., Uchida, M., Hibara, A., Sawada, T. & Kitamori, T. Determination of subyoctomole amounts of nonfluorescent molecules using a thermal lens microscope: Subsingle-molecule determination. *Anal. Chem.* **73**, 2112–2116 (2001).
91. Tamaki, E., Hibara, A., Tokeshi, M. & Kitamori, T. Microchannel-assisted thermal-lens spectrometry for microchip analysis. *J. Chromatogr. A* **987**, 197–204 (2003).
92. Shimizu, H., Mawatari, K. & Kitamori, T. Development of a differential interference contrast thermal lens microscope for sensitive individual nanoparticle detection in liquid. *Anal. Chem.* **81**, 9802–9806 (2009).
93. Shimizu, H., Miyawaki, N., Asano, Y., Mawatari, K. & Kitamori, T. Thermo-optical Characterization of Photothermal Optical Phase Shift Detection in Extended-Nano Channels and UV Detection of Biomolecules. *Anal. Chem.* **89**, 6043–6049 (2017).
94. Shimizu, H., Mawatari, K. & Kitamori, T. Femtoliter-scale separation and sensitive detection of nonfluorescent samples in an extended-nano fluidic device. *Analyst* **139**, 2154–2157 (2014).

# Chapter 2. Proposal and Verification of Photothermal Optical Diffraction

## 2.1 Introduction

As mentioned in chapter 1, conventional photothermal detection methods cannot be applied to $10^1$–$10^2$ nm channels due to the thermal diffusion to glass substrates and sensitivity decrease. This effect is inevitable for ultra-small channels and hinders the application of PTS to nanofluidics, although PTS enables label-free sensitive molecule/nanoparticle detection. To overcome this physical limitation, a new detection principle is essential which is not affected by thermal diffusion and can be applied to nanofluidics.

In this chapter, a novel photothermal detection method for nanofluidics: photothermal optical diffraction (POD) is developed to overcome the above limitation. The detection principle of the POD utilizes optical diffraction by a single nanochannel and photothermal effect of target analytes. Different from other photothermal detection methods, the heat diffusion to substrates also contributes to the POD signal; the POD enables a sensitive non-fluorescent molecule detection in nanochannels. First, the detection principle of the POD is proposed, and the experimental setup is constructed. Next, optical diffraction by a single nanochannel is investigated by theoretical calculations and experiments. Finally, the detection principle is verified, and the detection of non-fluorescent molecules in nanochannels is demonstrated. The signal generation mechanism is elucidated from several designed experiments.

## 2.2 Principle and Experimental

### 2.2.1 Principle of Photothermal Optical Diffraction

The detection principle of the POD is shown in Fig. 2-1. The width of nanochannels ($10^1$–$10^2$ nm) is smaller than the focused probe laser spot (~μm), and part of the probe laser passes through a glass substrate. After passing through the channel, a relative phase difference is generated by the difference of refractive index between water ($n$ = 1.33) and glass ($n$ = 1.46), which distort the wavefront of the probe laser. This wavefront distortion is observed as optical diffraction in the far-field. The intensity of the diffracted light ($P_D$) depends on the refractive index difference between water and glass ($\Delta n$). The intensity-modulated excitation laser (continuous wave mode) is focused on the nanochannel. The periodic excitation laser absorption and heat generation of target molecules in the nanochannel (photothermal effect) induces the periodic temperature rise of both water

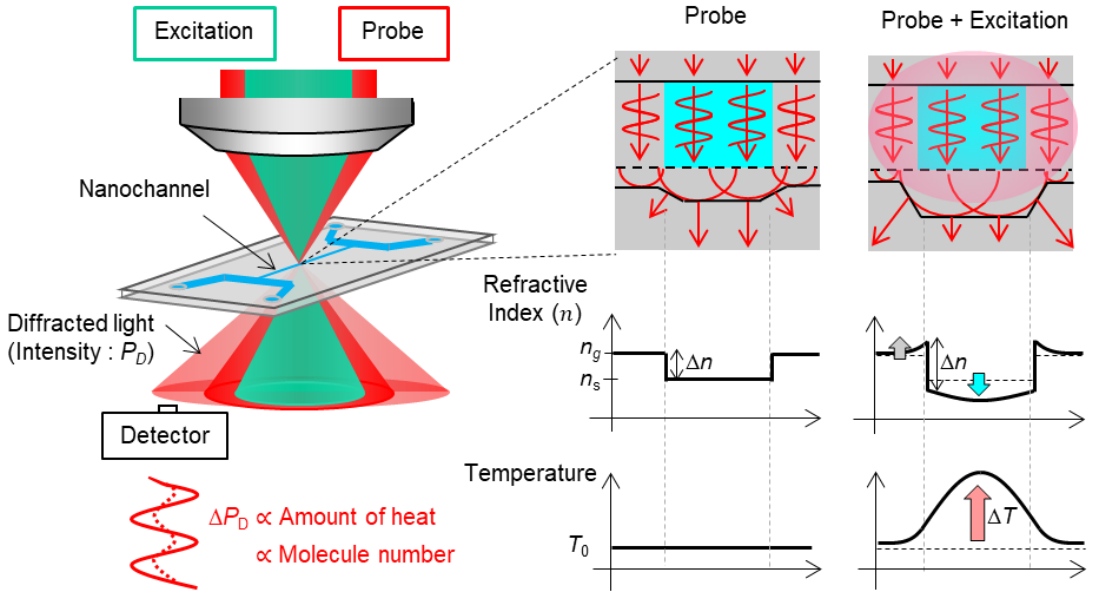


*Figure 2-1. Principle of Photothermal Optical Diffraction (POD).*

and glass substrates. The temperature coefficient of the refractive index ($dn/dT$) of water is $-9.1 \times 10^{-5}$, and $dn/dT$ of glass is $9.8 \times 10^{-6}$. Therefore, $\Delta n$ periodically increases by temperature rise, which leads to periodic diffracted light intensity change ($\Delta P_D$). The $\Delta P_D$ is proportional to the amount of heat: the number of molecules in the laser focus. Thus, the number of target molecules in the nanochannel (concentration) is measured from $\Delta P_D$.

The important feature of the POD is that the detection principle enables to utilize the heat diffusing to the glass substrate. Figure 2-2 shows the comparison of the effect of heat diffusion on the DIC-TLM and the POD. In the DIC-TLM, the signal is derived from the phase difference of two probe beams in a vertical direction.[1] Therefore, the DIC-TLM signal correlates to the sum of the refractive index change of water and glass substrates. The heat diffusion to glass substrates leads to a thermal loss and a cancelation effect due to the opposite sign of $dn/dT$, which decreases the sensitivity of the DIC-TLM and makes it difficult to apply to $10^1$–$10^2$ nm channels.[2] In the POD, however, the signal is derived from the phase difference of a single probe beam in a horizontal direction. Therefore, the POD signal correlates to the difference of the refractive index change of water and glass substrates. The heat diffusion to glass substrates increases $\Delta n$ which increases the sensitivity of the POD. The heat diffusion to glass substrates is inevitable in $10^1$–$10^2$ nm channels. Thus, the detection principle of the POD is essential for analyses utilizing ultra-small channels.

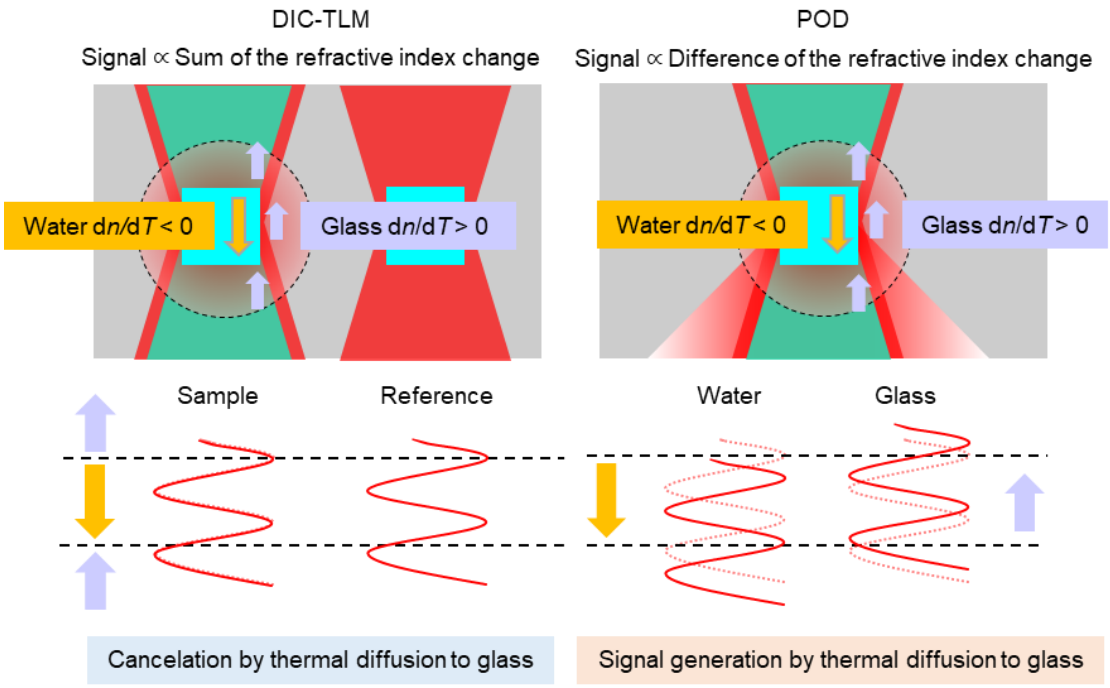


*Figure 2-2. Comparison of the effect of thermal diffusion* on the DIC-TLM and the POD.

### 2.2.2 Experimental Setup

Figure 2-3 (a) shows the schematic diagram of the POD. A 532 nm solid-state laser (Verdi-5M, Coherent Inc.) was used as an excitation laser. The intensity of the excitation laser was modulated by a mechanical light chopper (5584A, NF Corporation, Japan) at a modulation frequency of 1.1 kHz. A 633 nm He−Ne laser (25-LHP-925, Melles Griot Inc.) or a 660 nm solid-state laser (gem660, Laser Quantum Ltd., England) was used as a probe laser. These lasers were superpositioned by a dichroic mirror and focused on a nanochannel through an objective lens (magnification: 20×; NA, 0.45) which was attached to a microscope (BX51, Olympus Corporation, Japan). For precise position control of the nanochannel, the nanofluidic device was fixed on a 2-D stage (BIOS-235S, SigmaKoki Co., Ltd., Japan) which had 100 nm steps for each direction. The calculated spot diameter of the probe laser (approximately ~2 μm) was larger than the width of the nanochannel, and the focused lasers were diffracted by the nanochannel. After passing through the nanofluidic device, both probe and excitation lasers were converted into parallel lights by a collection lens (NA = 0.90). The excitation laser was cut by a color filter and an interference filter. The diffracted probe laser was separated from the transmitted probe laser by a slit (1–5 mm width and 10 mm height). The diffracted light intensity ($P_D$) was measured by a photodiode with a 400 μm aperture pinhole (ET-2030, Electro-Optics Technology Inc.). The $P_D$ was fed into a lock-in amplifier (LI5660, NFCorporation, Japan), and the component synchronized to the chopper frequency, the diffracted light intensity change ($\Delta P_D$) was extracted. The time constant (signal averaging time) of the lock-in amplifier was set to 1 sec. All experiments were conducted under the experimental conditions described above unless otherwise mentioned.

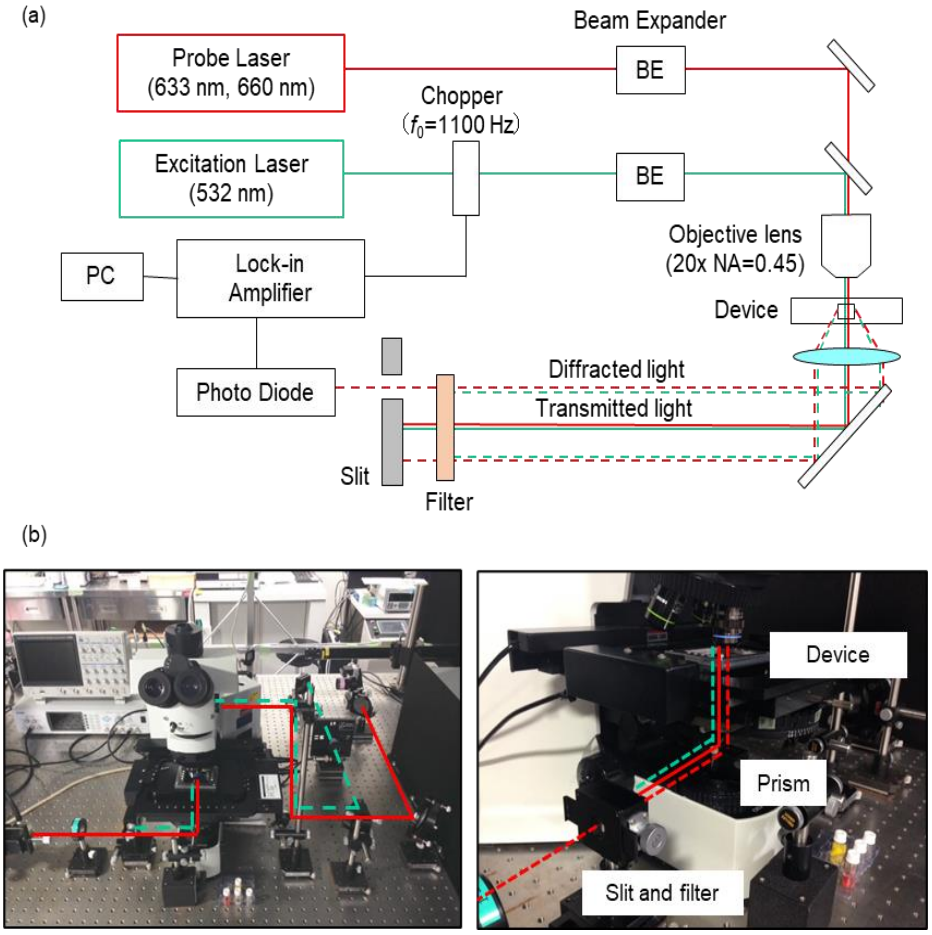


*Figure 2-3. Experimental setup of the POD: (a) Schematic diagram. (b) Photograph of the constructed experimental setup.*

The details of the signal measurement system by the lock-in amplifier are shown in Fig. 2-4. Since the temperature rise by the photothermal effect is μK–mK, $\Delta P_D$ is almost $10^3$ times smaller than $P_D$. Thus, the signal-to-background ratio (S/B) is less than 1/1000, and $\Delta P_D$ cannot be measured without additional procedures. To overcome this problem, the lock-in amplifier multiplies a measured signal with a reference signal from the light chopper and extracts a DC component by a low-pass filter, which means the selective measurement of the component that oscillates at the same frequency as the modulation

frequency.[3] By modulating the excitation laser intensity, $\Delta P_D$ also oscillates at the same modulation frequency, leading to the selective measurement by the lock-in amplifier. Note that this procedure cannot eliminate the component of $P_D$ which oscillates at the same frequency as the modulation frequency.

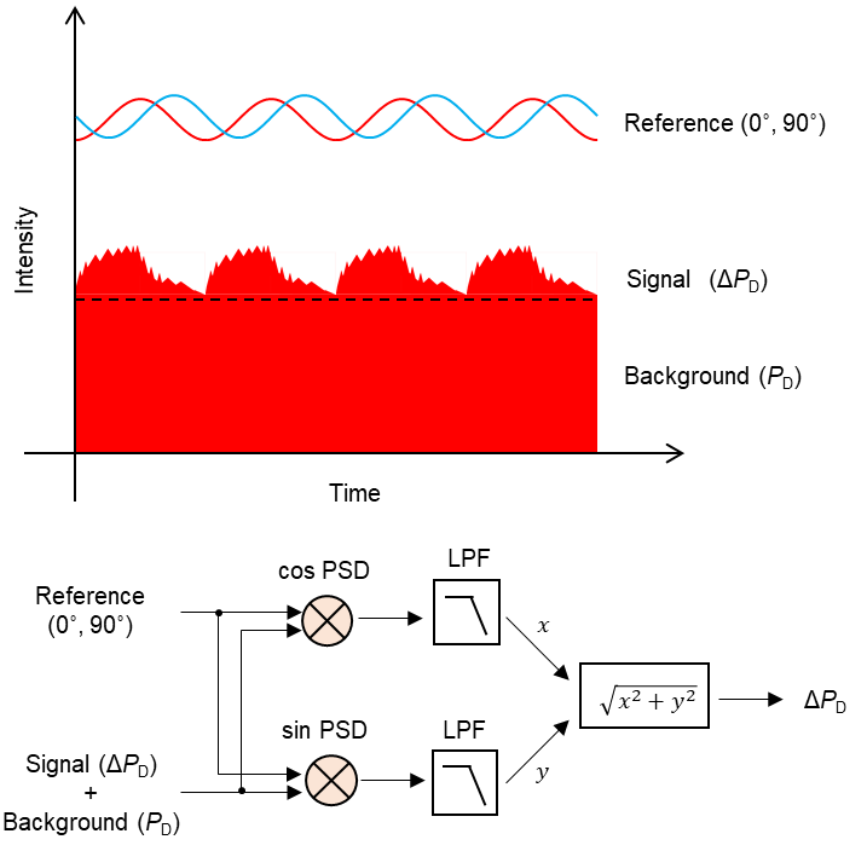


*Figure 2-4. Signal measurement system by a lock-in amplifier.*

### 2.2.3 Fabrication of Nanofluidics and Fluidic Control

Nanochannels were fabricated on a fused-silica glass substrate (70×30 $mm^2$, VIOSIL-SQ, Shin-Etsu Chemical Co., Ltd., Japan) by electron-beam lithography (ELS-7500, Elionix Inc., Japan) and plasma etching (NE-550, ULVAC Inc., Japan). The width and depth of fabricated nanochannels were measured by scanning electron microscope (equipped with ELS-7500), atomic force microscope (SPA-400, Seiko Instruments Inc., Japan), and stylus profilers (dektakXT, Bruker Corporation). For sample injection to the nanochannels, U-shaped microchannels were fabricated on another glass substrate by UV photolithography and plasma etching. Inlet holes were drilled at the endpoint of each microchannel. The width and depth of microchannels were 500 μm and 5 μm unless otherwise mentioned. By thermal bonding of the two glass substrates at 110 ºC for 3 hours, microchannels and nanochannels were connected. For sample introduction and flow velocity adjustment, a pressure-driven fluidic control system was used. Liquids in vials were pushed into microchannels via capillary (0.3 mm inner diameter) by pressure controller (MFCS-EZ, Fluigent Inc., France) which controls the pressure for up to four channels independently. The detailed fabrication process and fluidic control system are shown elsewhere.[4-6] The fluidic control system and a typical example of a fabricated nanofluidic device are shown in Fig. 2-5.

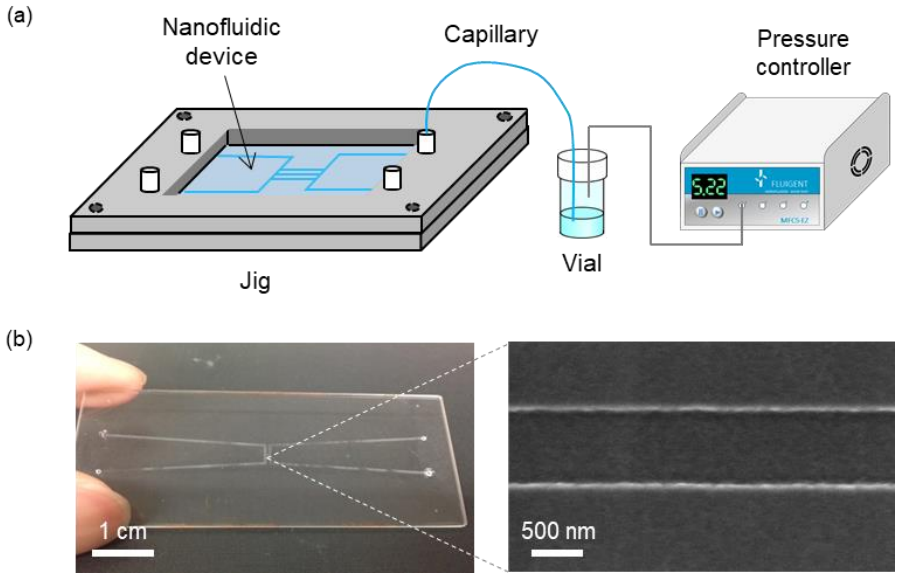


*Figure 2-5. Fluidic control system and example of the fabricated nanofluidic device: (a) Experimental setup for a pressure-driven fluidic control system. (b)Photograph of the nanofluidic device and SEM image of the nanochannel.*

## 2.3 Optical Diffraction by Nanochannels

### 2.3.1 Diffraction Theory

Understanding the mechanism of optical diffraction by a single nanochannel is important to develop and optimize the POD. The objective of this section is to derive the theoretical formula and elucidate optical diffraction by a single nanochannel from theoretical calculations and experiments. Generally, there are three possible procedures for theoretical calculations of light propagation: ray trace analysis, Fresnel-Kirchhoff diffraction theory, and electromagnetic rigorous theory based on Maxwell equations. Ray trace analysis is based on geometric optics and describes light propagation in terms of rays.[7] Ray trace analysis simply describes the light propagation and bending, while it does not consider optical diffraction and interference due to bold approximation of light. Therefore, ray trace analysis cannot be applied to optical diffraction by a single nanochannel which size is equal or smaller than the wavelength of visible light. Rigorous theory based on Maxwell equations describes light propagation without any approximation. However, analytical solutions can be obtained only under some special conditions, and numerical analysis is necessary in many cases. One of the rigorous theories that can be solved analytically is the Mie scattering theory.[8] The Mie scattering theory describes the scattering of an electromagnetic wave by a homogeneous spherical/cylindrical medium. Mie scattering theory can be applied to optical diffraction by a single nanochannel under the approximation that the cross-section of the nanochannel is circular. However, the actual cross-section is a rectangle, and the effect of channel width and depth cannot be fully investigated. Fresnel-Kirchhoff diffraction theory is based on wave optics and can describe the effect of optical diffraction and interference.[9] In the Fresnel-Kirchhoff diffraction theory, every point on an initial plane

is considered as a source of spherical wavelets (Huygens–Fresnel principle**)**. Then, the electromagnetic field at an observation plane is calculated from Kirchhoff–Helmholtz integral under Fresnel or Fraunhofer approximation. Although the Fresnel-Kirchhoff diffraction theory is not a rigorous theory and only valid under some approximations, it can be applied to optical diffraction by a single nanochannel to some extent. In this study, the Fresnel-Kirchhoff diffraction theory was used to derive the theoretical formula.

The derivation of the theoretical formula is as follows. Figure 2-6 shows the schematic diagram for the calculation of optical diffraction by a single nanochannel. The electromagnetic field of the focused $TEM_{00}$ mode laser beam at the channel position is expressed as follows:

$$f(x',y') = \sqrt{\frac{2P}{\pi\omega_z^2}}\, exp\left[-i\left\{kz_1 + arctan\left(\frac{z_1}{z_0}\right) - \frac{k(x'^2+y'^2)}{2R(z_1)}\right\} - \frac{x'^2+y'^2}{\omega_z^2}\right] \qquad (2-1)$$

where $P$ is the total power of the laser beam, $k = 2\pi/\lambda$ is the wavenumber, $R(z_1)$ is the phase front radius, $z_1$ is the distance from the beam waist to the channel position, $z_0$ =

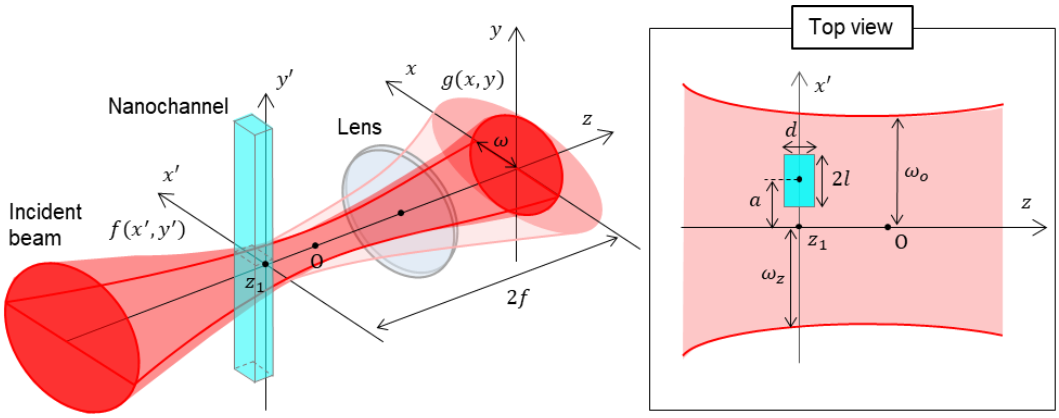


*Figure 2-6. Schematic diagram for the calculation of optical diffraction by a single nanochannel: (a) Overview and (b) Top view. Reproduced with permission.(P148, [2]) Copyright 2020, Springer Nature.*

$k\omega_0^2/2$ is the confocal parameter, $\omega_0$ is the radius ($1/e^2$) of the laser beam at its waist, and $\omega_z$ is the radius of the laser beam at the channel position defined by:

$$\omega_z = \omega_0 \sqrt{1 + \left(\frac{z_1}{z_0}\right)^2} \qquad (2-2)$$

At the channel position, a part of the laser beam passes through the nanochannel. The depth of a nanochannel is equal or smaller than the wavelength of visible light and several orders of magnitude smaller than the confocal length of the laser beam. Therefore, the nanochannel is approximately considered as a "phase filter", changing the phase of the beam by passing through the nanochannel. Under this assumption, the phase filter function $t(x', y')$ representing the relative phase shift by the nanochannel with width $2l$ and depth $d$ is expressed as follows:

$$t(x', y') = \begin{cases} e^{i\theta} \ (a - l \le x' \le a + l) \\ 1 \ (x' < a - l, x' > a + l) \end{cases} \qquad (2-3)$$

$$\theta = \frac{2\pi}{\lambda} \cdot (n_s - n_g) \cdot d \qquad (2-4)$$

where $a$ is the distance between the center of the beam and the channel position, $n_s$ is the refractive index of the solvent in the channel, and $n_g$ is the refractive index of the glass. The electromagnetic field after passing through the nanochannel is given by the product of incident electric field $f(x', y')$ and phase filter function $t(x', y')$. In the Fresnel-Kirchhoff diffraction theory under Fresnel approximation, the electromagnetic field of the laser beam at a back focal plane of a lens is equivalent to a Fourier transfer of the electromagnetic field at a front focal plane of the lens. If the front focal plane of the lens is set at the nanochannel position, the electric field at the back focal plane, $g(x, y)$ is given by:

$$g(x,y) = \frac{1}{i\lambda f}\iint f(x',\, y')t\,(x',\, y')exp\left\{-i\frac{2\pi}{\lambda f}(xx' + yy')\right\}dx'dy' \qquad (2-5)$$

where $f$ is the focal length of the lens. In this calculation, the lens diameter is assumed to be sufficiently large, and the pupil function is ignored. By using Eq. (2-3), $g(x, y)$ is divided into two terms:

$$g(x,y) = \{\mathcal{F}(x',\, y', \infty) + \left(e^{i\theta} - 1\right)\mathcal{F}(x',\, y', l)\} \qquad (2-6)$$

$$\mathcal{F}(x',\, y', l) = \frac{1}{i\lambda f}\iint_{a-l}^{a+l} f(x',\, y')\, exp\left\{-i\frac{2\pi}{\lambda f}(xx' + yy')\right\}dx'dy' \qquad (2-7)$$

By using Eq. (2-3), Eq (2-7) is transformed as follows:

$$\mathcal{F}(x',\, y', d) = \frac{1}{\lambda f}\sqrt{\frac{2P}{\pi\omega_z^2}}exp\left(-\frac{x^2 + y^2}{\omega^2}\right)$$
$$\times \int_{a-l}^{a+l} exp\left\{-\left(\frac{x'}{\omega_0 z_r} + i\frac{z_r x}{\omega}\right)^2\right\}dx' \cdot \int_{-\infty}^{\infty} exp\left\{-\left(\frac{y'}{\omega_0 z_r} + i\frac{z_r y}{\omega}\right)^2\right\}dy' \qquad (2-8)$$

where $\omega$ is the radius of the laser beam at the focal plane $z_r$ is defined by:

$$z_r = \sqrt{1 - i\frac{z_1}{z_0}} \qquad (2-9)$$

In Eq (2-8), terms related to phase only is ignored. The integral in Eq (8) is transformed by the following formula of Gaussian integral:

$$\int_s^t exp\{-(\alpha x + \beta)^2\}dx = \frac{\sqrt{\pi}}{2\alpha}\{\mathrm{erf}(\alpha t + \beta) - \mathrm{erf}\,(\alpha s + \beta)\} \qquad (2-10)$$

where *erf* $(x)$ is error function. By using Eq (2-8) and (10), $F(x', y', l)$ is described as follows.

$$\mathcal{F}(x',\, y', l) = \sqrt{\frac{2P}{\pi\omega^2}} exp\left(-\frac{x^2+y^2}{\omega^2}\right) \cdot \frac{1}{2}\left\{erf\left(\frac{a+l}{\omega_0 z_r} + i\frac{xz_r}{\omega}\right) - erf\left(\frac{a-l}{\omega_0 z_r} + i\frac{xz_r}{\omega}\right)\right\} (2-11)$$

By using Eq (2-6) and (2-11), $g(x, y)$ is described as follows:

$$g(x,y) = \sqrt{\frac{2P}{\pi\omega^2}} exp\left(-\frac{x^2+y^2}{\omega^2}\right)\{1 + (e^{i\theta} - 1)u(x,l)\} \qquad (2-12)$$

$$u(x,l) = \frac{1}{2}\left\{erf\left(\frac{a+l}{\omega_0 z_r} + i\frac{xz_r}{\omega}\right) - erf\left(\frac{a-l}{\omega_0 z_r} + i\frac{xz_r}{\omega}\right)\right\} \qquad (2-13)$$

The complex error function in Eq. (2-13) can be calculated by McLaughlin expansion. The intensity distribution of the laser beam $I(x, y)$ is given by the square of the electromagnetic field $g(x, y)$, which is expressed as:

$$I(x,y) = \frac{2P}{\pi\omega^2} exp\left\{-\frac{2(x^2+y^2)}{\omega^2}\right\}$$

$$\times [1 + 2|u(x,l)|^2(1 - cos\theta) - 2Re[u(x,l)](1 - cos\theta) - 2Im[u(x,l)]sin\theta\,] \qquad (2-14)$$

The first term of Eq. (2-14) represents the transmitted light which means intensity distribution of the laser beam without nanochannels. The second term represents the diffracted light. The third and fourth terms represent the effect of interference between transmitted light and diffracted light. Although the above calculation is based on the optical diffraction by a single nanochannel, this theoretical calculation can be applied to other nanostructures such as diffraction grating by changing $t(x', y')$, which leads to the change of $u(x, l)$. For example, when $TEM_{00}$ mode laser beam is focused on the symmetry center of the nanochannel diffraction grating with $n$ channels which width is $l$ and gap is $2l$, $g(x, y)$ is described as follows:

$$g(x,y) = \sqrt{\frac{2P}{\pi\omega^2}} exp\left(-\frac{x^2+y^2}{\omega^2}\right)\left\{1 + \left(e^{i\theta} - 1\right)\sum_{m=1}^{n} u_m(x,l)\,(-1)^{m+n}\right\} \qquad (2-15)$$

$$u_m(x,l) = \frac{1}{2}\left\{erf\left(\frac{(2m-1)l}{\omega_0 z_r} + i\frac{xz_r}{\omega}\right) - erf\left(-\frac{(2m-1)l}{\omega_0 z_r} + i\frac{xz_r}{\omega}\right)\right\} \qquad (2-16)$$

If optical diffraction by a single nanochannel is applied to a sensor or detector, the signal is diffracted light intensity change ($\Delta P_D$) caused by the refractive index change of solvent in the nanochannel ($\Delta n_s$) and the surrounding medium such as glass substrate ($\Delta n_g$). Assuming that $\Delta n_s$ and $\Delta n_g$ are small and $z_1 = 0$, $\Delta P_D(x, y)$ is expressed as follows:

$$\Delta P_D(x,y) \approx \frac{4Pd(\Delta n_s - \Delta n_g)}{\lambda\omega^2} exp\left\{-\frac{2(x^2+y^2)}{\omega^2}\right\} \cdot 2u(x,l)\,\{u(x,l) - 1\} sin\theta \qquad (2-17)$$

Assuming that initial diffracted light intensity ($P_D$).is constant for all measurements, the ratio of $\Delta P_D$ and $P_D$ which is equivalent sensing performance is described as follows:

$$\frac{\Delta P_D}{P_D} = \frac{sin\theta}{1 - cos\theta} \cdot \frac{2\pi d(\Delta n_s - \Delta n_g)}{\lambda} \approx \frac{2\left(\Delta n_s - \Delta n_g\right)}{\left(n_s - n_g\right)} \;\; (\theta \ll 1). \qquad (2-18)$$

These theoretical formulas indicate several important features of sensing systems utilizing nanochannel diffraction. First, the intensity distribution of diffracted light does not depend on the refractive indices if the channel depth is shallow. The relative value of the spot radius and the channel width determines the intensity distribution, in other words, diffraction patterns. Second, diffracted light intensity mainly depends on the channel depth and refractive indices. Third, sensing performance does not largely depend on the channel width and depth. Note that the spatial distribution of $\Delta n_s$ and $\Delta n_g$ needs to be considered for accurately calculating the signal of POD, which is a little difficult to calculate analytically.

### 2.3.2 Verification of Optical Diffraction

In the previous section, the theoretical formula of optical diffraction by nanochannels was derived based on the Fresnel-Kirchhoff diffraction theory. In this chapter, diffracted light intensity and distribution were calculated for various experimental conditions. For theoretical calculations, following numerical values were used: $\omega_0$ = 1.1 μm, $\lambda$ = 633 nm, $n_s$ = 1.33, $n_g$ = 1.46, $\omega$ = 2.5 mm, and the detection region was 5–15 mm from the center of the laser spot. These values were adjusted to the actual experiments. To compare the theoretical calculations and experimental results, calculated and experimental values were normalized by their maximized value.

First, optical diffraction by a single nanochannel was observed. Figure 2-7 shows the images of a probe laser after passing through the nanochannel and collective lens. The nanochannel was empty (filled with air). In this experiment, only a probe laser was focused on a nanochannel through an objective lens (NA = 0.30). The channel width is

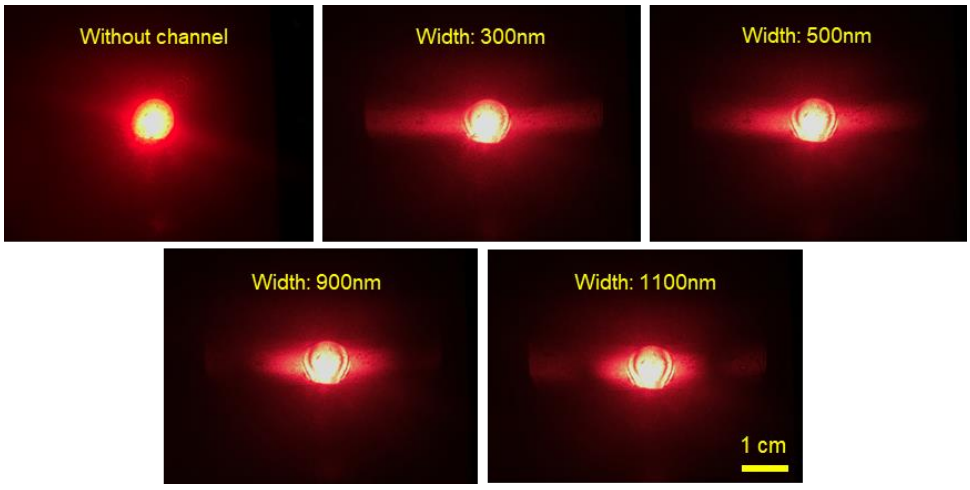


*Figure 2-7. Images of a probe laser after passing through the nanochannel and collective lens for different channel sizes. Partially reproduced with permission. (P148, [1]) Copyright 2020, American Chemical Society.*

300–1100 nm, and the channel depth was fixed at 300 nm. The diffracted light was observed in the direction perpendicular to the longitudinal direction of the nanochannel. No diffracted light was observed in the direction parallel to the longitudinal direction of the nanochannel because channel length is longer than the diameter of the probe beam spot which means no phase difference in the longitudinal direction of the nanochannel. As channel width became wider, the diffraction angle became smaller and the first-order maximum point was observed. This tendency indicates that a smaller nanochannel is suitable for the measurement of optical diffraction because a large diffraction angle enables the separation of diffracted light from the transmitted light.

Next, the effect of the relationship between channel size and diffracted light intensity was investigated. The measured range of channel width was 220–2500 nm, and the channel depth was fixed at 220 nm. These channels were filled with water. The results of calculations and experiments are shown in Fig. 2-8 (a). The diffracted light intensity

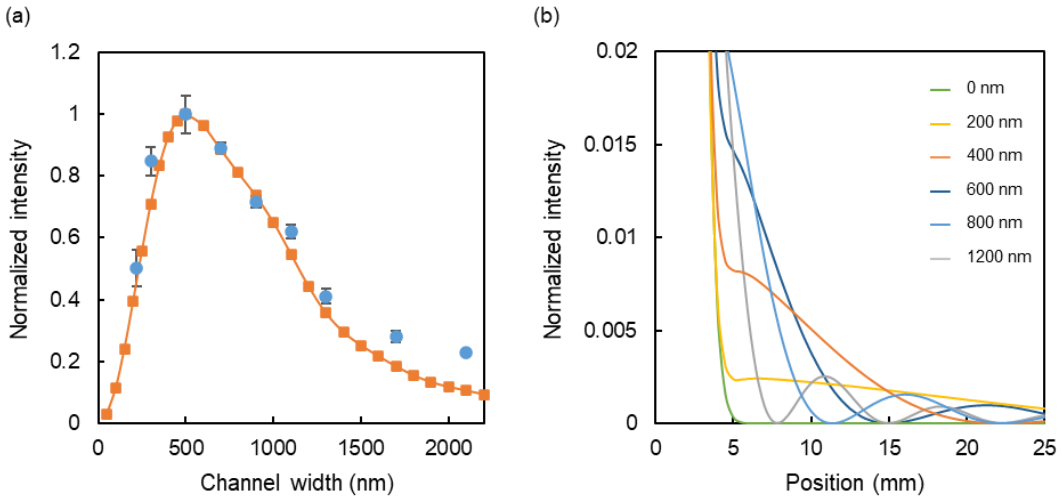


*Figure 2-8. Calculation of the channel width effect: (a) Normalized diffracted light intensity for different channel width. (b) Comparison of diffraction pattern at the detection position for several channel widths. Reproduced with permission. (P148, [2]) Copyright 2020, Springer Nature.*

was maximized at a certain channel width. The tendency is consistent with qualitative prediction. For narrow channels, most of the probe laser pass through the substrates, and the effect of wavefront distortion by refractive index difference between water and glass substrate becomes relatively small. For wide channels, most of the probe laser passes through the nanochannel, and the effect of wavefront distortion by refractive index difference also becomes relatively small. Thus, the optimum channel width depends on the spot size of the probe laser. For current experimental conditions, the optimum channel width was around 500 nm, which is almost the same as half of the spot radius. Note that the optimum channel width also depends on other factors such as the wavelength of the probe laser or the detection region of the diffraction pattern. Figure 2-8 (b) shows diffraction patterns for several channel widths. Calculated diffraction patterns show that the diffraction region becomes broader as channel width becomes smaller which is well consistent with experimental results shown in Fig. 2-7.

The effect of channel width was also investigated. The measured range of channel depth was 60–400 nm, and the channel width was fixed at 400 nm. The results are shown in Fig. 2-9. The diffracted intensity decreased in proportion to the channel depth due to the decrease of phase difference generated by nanochannels. These results show that phase filter approximation was valid in the range of measured channel depth. The calculated relationship between channel size and diffracted light intensity was almost consistent with experimental results.

The optical diffraction by a single nanochannel is sensitive to the focused position of the probe laser. Figure 2-10 (a) shows the dependency of diffracted light intensity on the relative position of the laser focus in the x-axis direction which is perpendicular to the longitudinal direction of the nanochannel. The channel position was adjusted by the

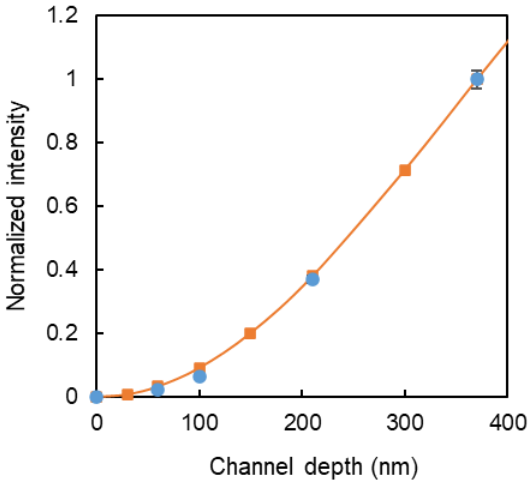


*Figure 2-9. Normalized diffracted light intensity versus channel depth. The orange line represents theoretical calculations, and the blue dots represent experimental results. Reproduced with permission. (P148, [2]) Copyright 2020, Springer Nature.*

electric stage with 100-nm steps. The diffracted light intensity was maximized when the center of the nanochannel coincided with the center of laser focus, and it decreased as the relative position between the nanochannel and the laser focus ($\Delta x$) becomes longer. The full width at half maximum was calculated to be approximately 1.4 μm. Figure 2-10 (b) shows the dependency of diffracted light intensity on the relative position of laser focus in the z-axis direction which is parallel to the laser propagation direction. The channel position was adjusted by a manual stage height controller with a 1 μm step. The diffracted light intensity was maximized at $\Delta z = 0$ and gradually decreased as $\Delta z$ becomes larger. The full width at half maximum was approximately 10 μm. These results show that the optimum position of the laser focus is at the center of the nanochannel. Precise position alignment is essential for optical diffraction by a single nanochannel. Enlarging the spot size by a lower NA objective lens can increase the tolerance for the position while it also affects diffracted light intensity and distribution. The calculated relationship between channel size and diffracted light intensity was almost consistent with experimental results.

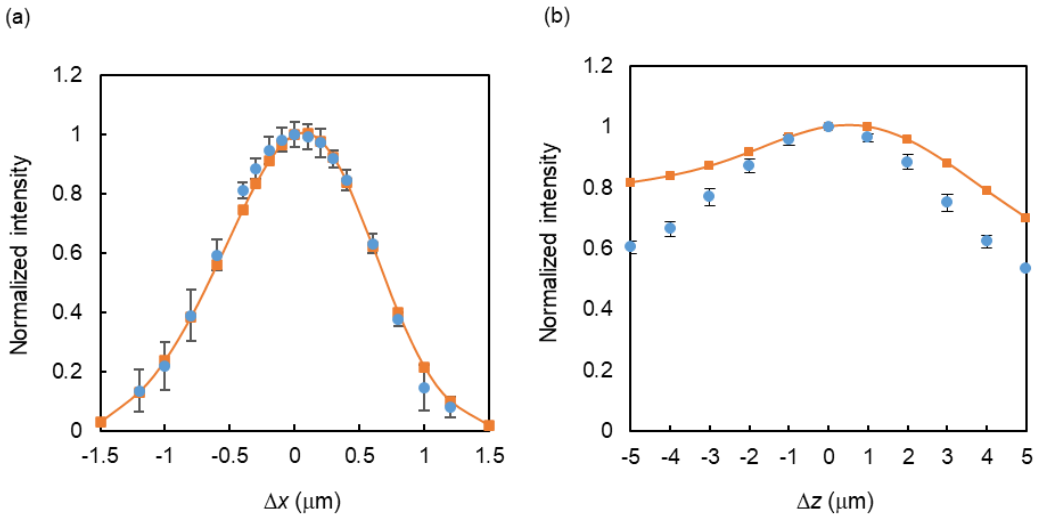


*Figure 2-10. Normalized diffracted light intensity on the relative position of the laser focus in the (a) x-axis direction and (b) z-axis direction. Reproduced with permission. (P148, [2]) Copyright 2020, Springer Nature.*

Diffracted light intensity also largely depends on the optical property of the solvent in the nanochannel. Figure 2-11 shows the relationship between the diffracted light intensity and the refractive index of the solvent. The diffracted light intensity was minimized when the refractive index of the solvent was close to that of the glass substrate ($n_g$ = 1.46) due to the decrease of phase difference generated by the refractive index difference. These results also suggest that optical diffraction by a single nanochannel can be used for refractive index measurement of the solvent in the channel.

To evaluate the limit of detectable refractive index change, diffracted light intensity was measured in a narrow refractive index range controlled by a mixture of solvents. The refractive indices of mixed solutions are slightly changed by changing the mixing ratio. Mixed solutions of water and ethanol were used with a mixing ratio of 10:0 to 6:4, corresponding to the refractive index range of 1.333 to 1.361. Each refractive index of the solvent was checked by a refractometer. Figure 2-12 shows the calibration curve of

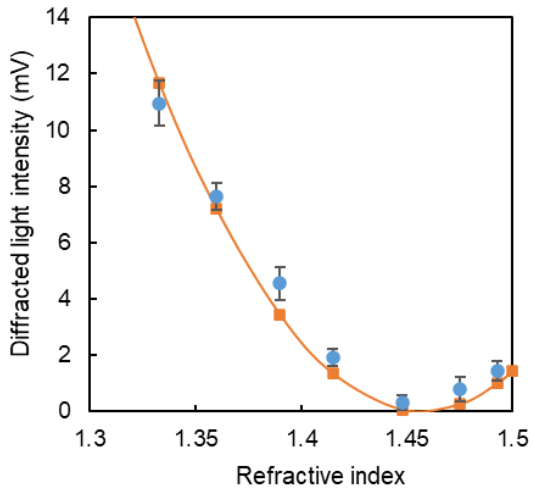


*Figure 2-11. Diffracted light intensity for refractive indices of solvents. The orange line represents theoretical calculations, and the blue dots represent experimental results. Reproduced with permission. (P148, [2]) Copyright 2020, Springer Nature.*

the refractive index for a nanochannel with 400 nm deep and wide. Diffracted light intensity changed linearly for a narrow range of refractive index change, and the sensitivity was -190 mV/RIU. The limit of detection (LOD) is defined as $\Delta n$ that gives diffracted light intensity change equivalent to $3\sigma$, and $\sigma$ is calculated from the average signal fluctuation of measured solvents. The calculated LOD was $7.4 \times 10^{-4}$ RIU. The detection volume calculated from spot size and channel size was 0.35 fL. These results show that the sub-femtoliter refractory was realized by single nanochannel diffraction. The LOD of our method is a little higher than those of other diffraction grating methods.[10,11] This is due to the large noise derived from the position sensitivity of single nanochannel diffraction.

The number of nanochannels also affects the diffracted light intensity. Figure 2-13 (a) shows calculated diffraction patterns for optical diffraction by different numbers of channels. The channel width and depth were set to 400 nm, and the gap was set to 800

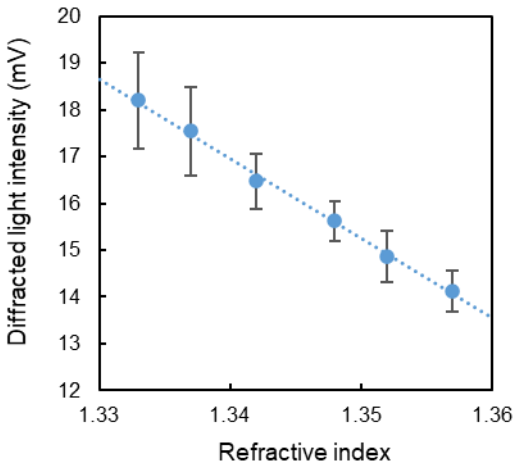


*Figure 2-12. Calibration curve of refractive index for a nanochannel with 400 nm deep and wide.*

nm (1:1). First-order maximum points derived from optical interference were observed for multiple nanochannels. This result shows that the tendency of optical diffraction by a single nanochannel is different from those of multiple nanochannels. Figure 2-13 (b) shows a comparison of theoretical calculations and experimental results. Theoretical calculations were almost consistent with experimental results, suggesting the derived theoretical formula is also valid for multiple nanochannels.

In summary, theoretical calculations showed good agreement with experimental results, suggesting it can be used for the estimation of the optical diffraction by nanochannels with various materials, shapes, and sizes. The theoretical formula can be applied to other nanostructures such as diffraction gratings or pillars. As mentioned in chapter 1, several unique properties in nanochannels have been reported. However, experimental results revealed no or little refractive index change of water in the nanochannel. Thus, the optical diffraction by nanochannels can be designed based on the Fresnel-Kirchhoff diffraction theory and liquid properties measured in the bulk.

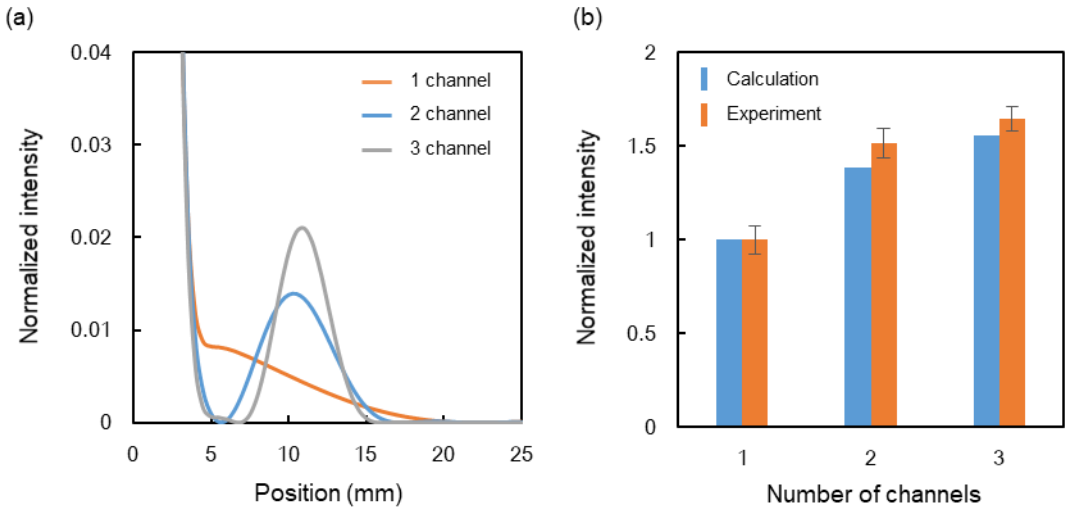


*Figure 2-13. (a) Calculated diffraction patterns for optical diffraction by different numbers of channels. (b) Comparison of theoretical calculations and experimental results.*

## 2.4 Principle Verification

### 2.4.1 Demonstration of Label-free Molecule Detection

To verify the signal generation by target molecules, an aqueous solution of the non-fluorescent dye, Sunset Yellow FCF (Wako Pure Chemical, Osaka, Japan) was introduced to the nanochannel as a sample. The absorption coefficient is 4800 $M^{-1}$ $cm^{-1}$ at 532 nm. The width and depth of the nanochannel were 400 nm, respectively. Figure 2-14 shows the results of signal measurement for 0 μM blank solutions and 100 μM sample solutions. The difference in signal intensity between the blank solution and the sample solution was observed when both probe and excitation lasers were focused on the nanochannel. Signals were not generated when either probe laser or excitation laser is off. These results show that the observed signals were derived from the photothermal effect of target molecules in the sample solution.

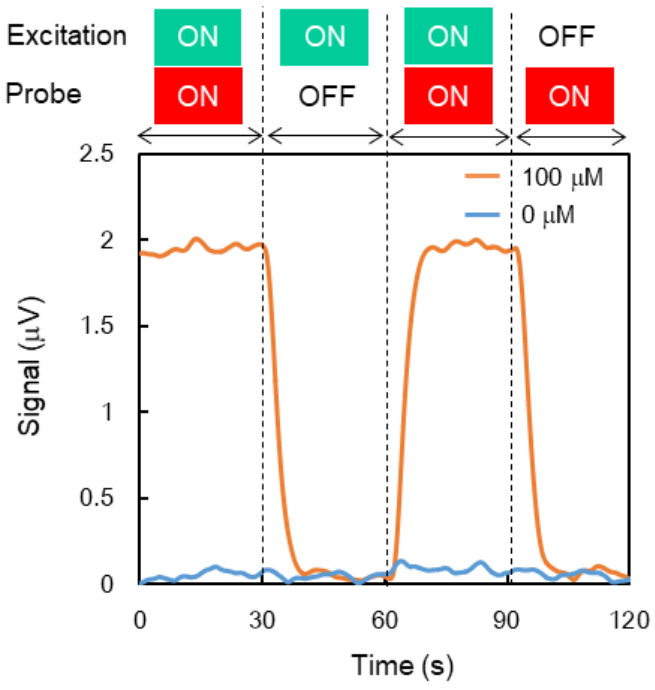


*Figure 2-14. POD signal for 0 μM blank solutions and 100 μM sample solutions.*

Furthermore, the relationship between signal intensity and excitation intensity was confirmed. As shown in Fig. 2-15, the signal intensity almost linearly increased for excitation intensity, suggesting signals were derived from the photothermal effect of target molecules. An optical saturation was observed for higher excitation intensity. From the above experiments, the non-fluorescent molecule detection by the POD was demonstrated for the first time.

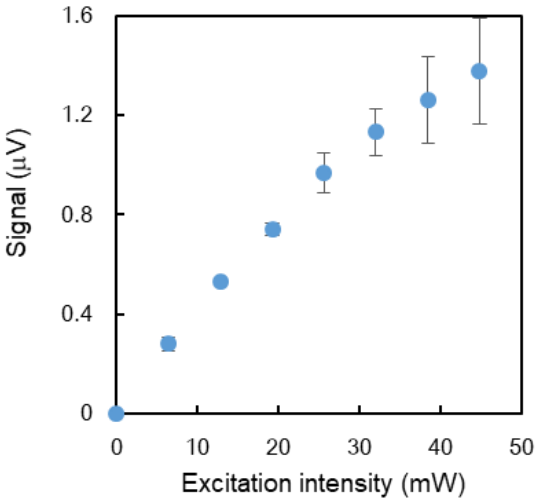


*Figure 2-15. Relationship between signal intensity and excitation intensity. Excitation intensity was measured by a power-meter under the objective lens.*

### 2.4.2 Elucidation of Signal Generation Mechanism

Although signals were obtained by experimental setup based on the detection principle, the signal generation mechanism was unknown. To confirm that obtained signals were based on the proposed detection principle, several experiments were designed and conducted.

First, the relationship between signal intensity and initial diffracted light intensity ($P_D$) was checked. The initial diffracted light intensity was defined as the difference of measured signal intensity with and without nanochannels. In this definition, the signal, diffracted light intensity change ($\Delta P_D$) should be proportional to $P_D$. To check the effect of $P_D$, the detection position defined by a slit position was scanned from a transmitted light region inside the probe laser spot to a diffracted light region outside the spot. At the transmitted light region, the effect of optical diffraction is negligible, and $P_D$ is low. At the diffracted light region, the effect of optical diffraction is dominant, and $P_D$ is high. For precise position measurement, the spot size of the probe laser was expanded to 9 mm in radius at a slit position by lenses, and slit width was set to 1 mm. Figure 2-16(a) shows $\Delta P_D$ for each detection position. High $\Delta P_D$ was obtained at the diffracted light region, and no or little $\Delta P_D$ was obtained at the transmitted light region. Figure 2-16(b) shows the relationship between $P_D$ and $\Delta P_D$. The $\Delta P_D$ almost linearly increased for $P_D$, suggesting obtained signals were derived from optical diffraction.

Although the above results suggested the signals were generated by photothermal effect and optical diffraction, it was still unknown that the signals were derived from the change of refractive index difference between water and glass substrate. Therefore, the signal generation mechanism was checked by measuring the signals of sample solutions with different refractive indices. Generally, $dn/dT$ of solvents is negative, and $dn/dT$ of

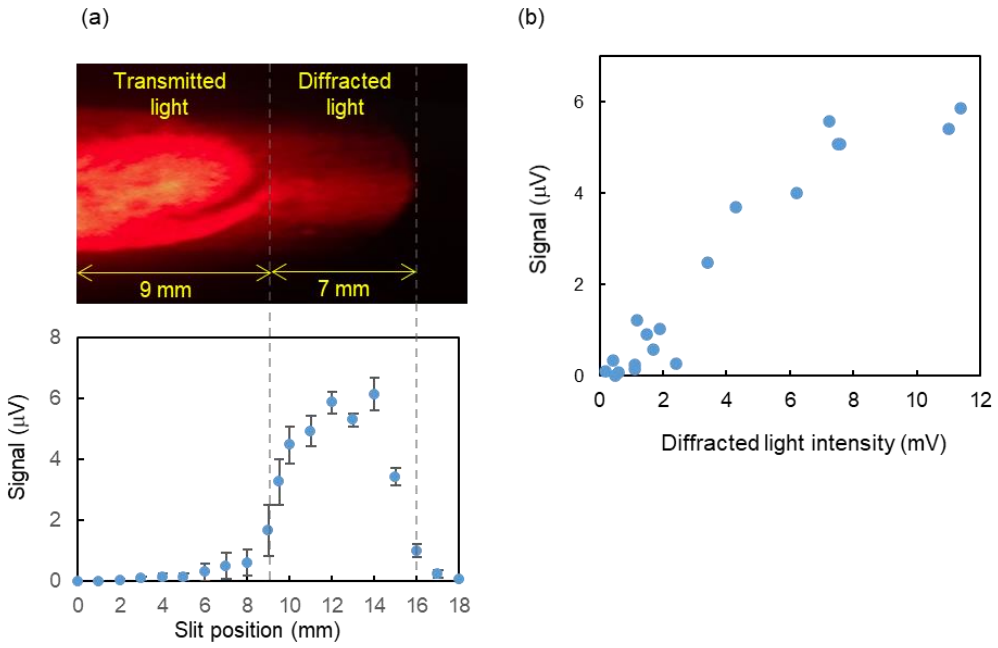


*Figure 2-16. (a) Signal intensity ($\Delta P_D$) for each detection position. (b) Relationship between diffracted light intensity ($P_D$) and signal intensity ($\Delta P_D$) for each detection position. Partially reproduced with permission. (P148, [1]) Copyright 2020, American Chemical Society.*

glass substrates is positive. Thus, the refractive index of the solvent ($\Delta n_s$) and the glass substrate ($\Delta n_g$) change in opposite directions. When the refractive index of the solvent is lower than the glass substrate ($n_s < n_g$), $\Delta n$ increases by temperature increase; $\Delta P_D$ should be positive for $n_s<n_g$. In contrast, when the refractive index of the solvent is higher than the glass substrate ($n_s > n_g$), $\Delta n$ decreases by temperature increase; $\Delta P_D$ is negative for $n_s > n_g$. Thus, the relative phase delay of the signal for the excitation laser modulation will invert depending on whether the refractive index of the solvent is higher or lower than the refractive index of the glass substrate ($n = 1.46$) as shown in Fig. 2-17. Based on these predictions, the time trace of signal and phase was measured for the replacement of the solution in the channel from hexane ($n = 1.38$) to toluene ($n = 1.50$). As a test sample,

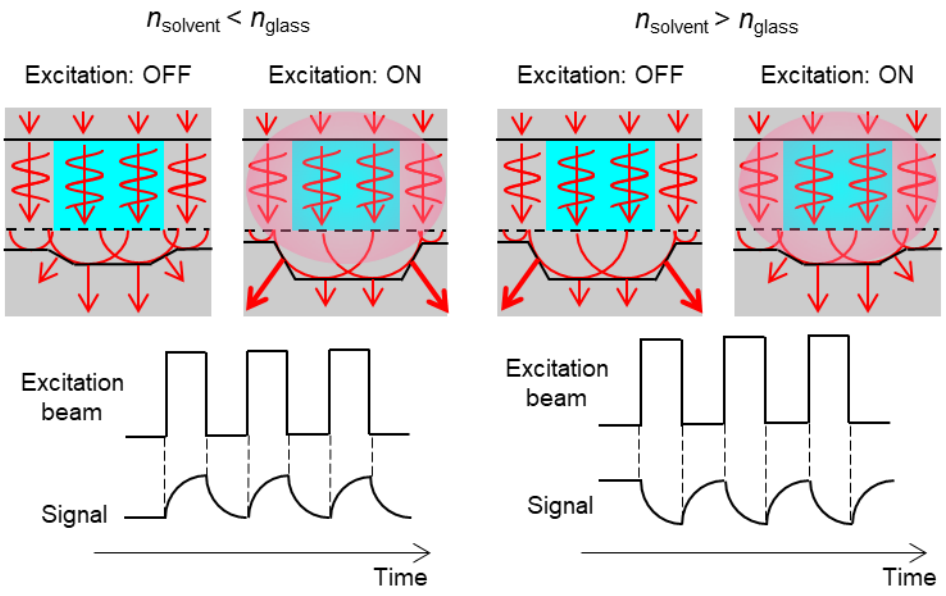


*Figure 2-17. Relationship between refractive indices of solvents and diffracted light intensity change by the photothermal effect.*

Sudan IV was used for both solvents. The experimental result is shown in Fig. 2-18 (a). The phase of the signal changed almost 180° when the solution in the nanochannel was replaced from hexane to toluene. Also, the signal intensity reached almost 0 at that time, suggesting the sign of the $\Delta P_D$ was inverted. The signal increase at the initial state of the replacement might be due to the mixing of hexane and toluene. As a control experiment, the time trace of signal and phase was measured for the replacement of the solution in the channel from hexane ($n$ = 1.38) to acetonitrile ($n$ = 1.34). The experimental result is shown in Fig.2-18 (b). No phase change was observed when the solution in the nanochannel was replaced from hexane to acetonitrile. From these results, it is proved that the POD signal was generated from the change of $\Delta n$.

As a follow-up experiment, the difference with the signal generation mechanism of other PTS such as thermal lens microscope (TLM) or photothermal deflection

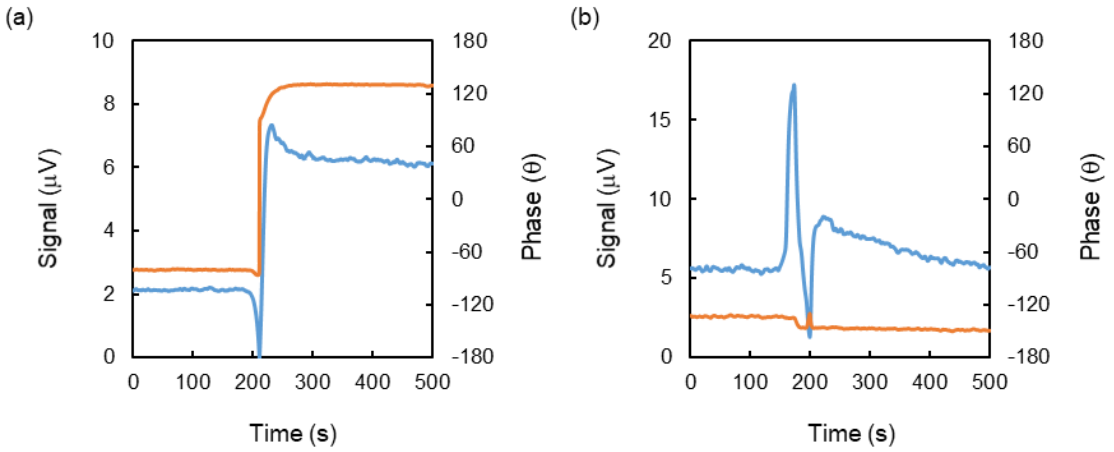


*Figure 2-18. Time trace of signal and phase for solution change: (a) from hexane to toluene. (b) from hexane to acetone.*

spectroscopy (PDS) was checked. In the case of dual-beam PTS, signal and phase dependency on the relative focal point of two beams is closely related to the signal generation mechanism, and the dependency can be used as proof of the detection principle. Figure 2-19 (a) shows the experimental arrangement. The center of the channel was set as $z = 0$. The focal point of the excitation beam was fixed at the channel position to maximize the photothermal effect by target molecules in the nanochannel. The focal point of the probe beam ($\Delta z$) was scanned along the z-axis by adjusting a beam expander. The position of the focal point was checked by a CCD camera and the scale of the z-axis stage. Experimental results are shown in Fig. 2-19 (b). The signal intensity reached a maximum at $\Delta z = 0$, and signal intensity decreased as $\Delta z$ becomes larger. These results are in good agreement with the proposed detection principle of the POD in which maximal diffracted light intensity is obtained when the probe laser is focused on the center of the nanochannel. These results also suggest that the signal generation mechanism is different from those of TLM and PDS in which the signal intensity reached the highest value when the focal point is adjusted to the confocal length.[12,13] Also, no phase shift was observed around $\Delta z$

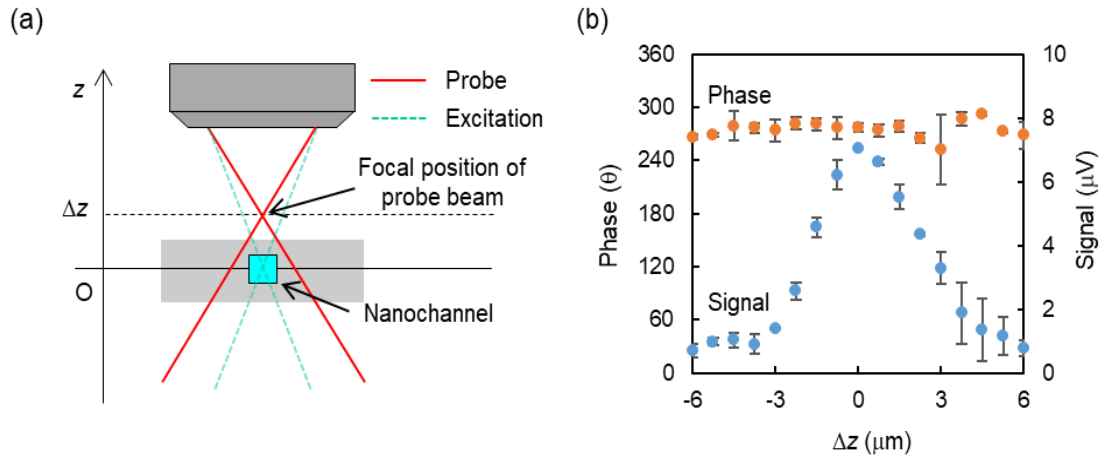


*Figure 2-19. Relationship between the focal position of the probe beam and POD signal: (a) experimental arrangement. (b) signal and phase for Δz. Reproduced with permission. (P148, [1]) Copyright 2020, American Chemical Society.*

= 0. As mentioned above, the phase of the signal is related to the sign of the signal, and no phase shift means that diffracted light intensity change by photothermal effect always increases or always decreases. This result is in good agreement with the proposed detection principle of the POD because diffracted light intensity always increases by photothermal effect for aqueous solutions, while the sign of the signal is reversed at $\Delta z$ = 0 for TLM and PDS. These signal and phase dependencies indicate that the detection principle of the POD is different from other photothermal detection methods such as TLM and PDS.

In summary, the signal generation mechanism was confirmed which was well consistent with the proposed detection principle of the POD. Thus, a label-free detection method for nanofluidics utilizing photothermal effect and optical diffraction was for the first time developed.

## 2.5 Summary

In this chapter, a novel detection method for nanofluidics named photothermal optical diffraction (POD) was developed. First, the detection principle of the POD was proposed, and the experimental setup was constructed. Next, the mechanism of optical diffraction by nanochannel was theoretically described and confirmed by experiments. Finally, the detection principle of the POD was verified, and the POD realized the detection of non-fluorescent molecules in nanochannels with 400 nm wide and deep. Furthermore, the signal generation mechanism was precisely investigated and elucidated by several experiments. Thus, a novel label-free molecule detection method for nanofluidics was developed.

## 2.6 References of Chapter 2


1. Shimizu, H., Mawatari, K. & Kitamori, T. Development of a differential interference contrast thermal lens microscope for sensitive individual nanoparticle detection in liquid. *Anal. Chem.* **81**, 9802–9806 (2009).
2. Shimizu, H., Miyawaki, N., Asano, Y., Mawatari, K. & Kitamori, T. Thermo-optical Characterization of Photothermal Optical Phase Shift Detection in Extended-Nano Channels and UV Detection of Biomolecules. *Anal. Chem.* **89**, 6043–6049 (2017).
3. Blair, D. P. & Sydenham, P. H. Phase sensitive detection as a means to recover signals buried in noise. *J. Phys. E.* **8**, 621–627 (1975).
4. Tsukahara, T. *et al.* Electrochemical studies on liquid properties in extended nanospaces using mercury microelectrodes. *Electrophoresis* **30**, 3212–3218 (2009).
5. Tsukahara, T., Mawatari, K., Hibara, A. & Kitamori, T. Development of a pressure-driven nanofluidic control system and its application to an enzymatic reaction. *Anal. Bioanal. Chem.* **391**, 2745–2752 (2008).
6. Morikawa, K. *et al.* Advanced Top-Down Fabrication for a Fused Silica Nanofluidic Device. *Micromachines* **11**, 995(11pp) (2020).
7. Doerner, E. C. General Ray-Tracing Procedure. J. Opt. Soc. Am. A **52**, 672–678 (1961).
8. Hulst, H. C. van de. *Light scattering by small particles*. (Courier Corporation, 1981).
9. Max, B. & Emil, W. *Principles of Optics*. (Cambridge University Press, 1999).
10. Purr, F. *et al.* Asymmetric nanofluidic grating detector for differential refractive index measurement and biosensing. *Lab Chip* **17**, 4265–4272 (2017).
11. Ajiri, T. *et al.* Optimization of the nanofluidic design for label-free detection of biomolecules using a nanowall array. *Sensors Actuators, B Chem.* **250**, 39–43 (2017).
12. Bertolotti, M., Liakhou, G., Li Voti, R., Michelotti, F. & Sibilia, C. Method for thermal diffusivity measurements based on photothermal deflection. *J. Appl. Phys.* **74**, 7078–7084 (1993).
13. Uchiyama, K., Hibara, A., Kimura, H., Sawada, T. & Kitamori, T. Thermal Lens Microscope. *Jpn. J. Appl. Phys.* **39**, 5316–5322 (2000).

# Chapter 3. Concentration Determination in $10^1$ nm Space

## 3.1 Introduction

To realize chemical/biological analyses by nanofluidic devices, concentration determination of analyte solutions in $10^1$–$10^2$ nm channels is essential. Generally, laser-induced fluorescence (LIF) is used for concentration determination due to high sensitivity and selectivity.[1,2] However, few molecules have native-fluorescence, and tedious labeling or tagging procedure is inevitable for a wide range of applications.[3] Electrical or electrochemical detection is a widely used label-free detection method.[4,5] However, the coexistence of complicated nanostructures such as an electrode and nanofluidic circuit is still challenging; a non-invasive yet highly sensitive detection method is strongly required for $10^1$–$10^2$ nm nanofluidic devices.

In the previous chapter, a novel photothermal detection method for nanofluidics: photothermal optical diffraction (POD) was developed which utilizes optical diffraction by a single nanochannel and photothermal effect of target analytes. Although the detection principle and signal generation mechanism were confirmed, experimental conditions are not optimized, and the detection performance is still unknown. Furthermore, whether the detection principle of the POD enables label-free detection method for $10^1$–$10^2$ nm channels without sensitivity degradation is not verified.,

In this chapter, concentration determination in $10^1$–$10^2$ nm channels by the POD is verified for the first time, and the detection performance is evaluated. First, experimental conditions are optimized to maximize the signal to noise ratio. Then, concentration determination in $10^2$ nm channels by the POD is demonstrated, and the detection performance is evaluated from the calibration curve. Furthermore, the detection performance of the POD and the DIC-TLM is compared for different channel sizes to clarify the characteristics of the POD. Next, the detection performance is further

improved by the solvent enhancement effect. The thermal/optical enhancement factor of organic solvents is investigated by thermal simulations, optical calculations, and experiments. Finally, concentration determination in $10^1$ nm channels by the POD is demonstrated, and the detection performance is evaluated.

### 3.2 Concentration Determination in $10^2$ nm Channels

#### 3.2.1 Optimization of Experimental Condition

First, the experimental conditions of the POD were optimized to improve the detection performance. First, the initial diffracted light intensity was optimized. As described above, the signal, diffracted light intensity change ($\Delta P_D$) is proportional to initial diffracted light intensity ($P_D$). However, higher $P_D$ also leads to larger background noise. To optimize $P_D$, the signal-to-noise ratio (S/N) was measured for different $P_D$ which was adjusted by changing the probe laser intensity, and the value was measured by a photodiode and a lock-in amplifier. Sunset Yellow FCF aqueous solution (100 μM) was introduced to nanochannels as a test sample. Experimental results are shown in Fig. 3-1. The S/N ratio reached a maximum value of around 15 mV. This result also shows that the noise derived from the initial diffracted light (background noise) mainly determines the performance of the POD. Note that $P_D$ also depends on the and laser spot size and the size

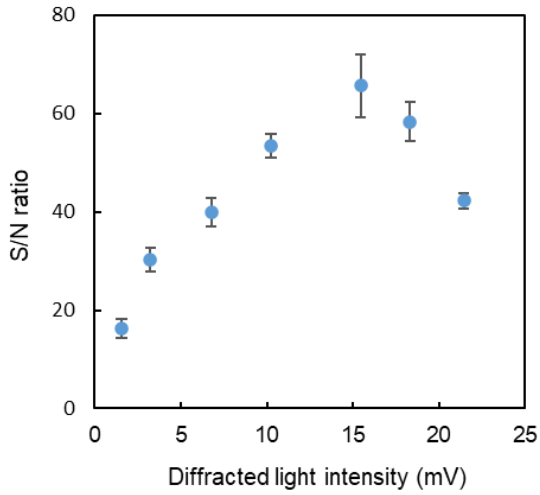


*Figure 3-1. S/N ratio versus diffracted light intensity. Reproduced with permission. (P148, [3]) Copyright 2020, American Chemical Society.*

of nanochannel, and $P_D$ measured by a photodiode and lock-in amplifier needs to be adjusted to the optimized value.

Next, the modulation frequency of the excitation laser was optimized. Generally, higher modulation frequency leads to signal intensity decrease due to shorter laser irradiation time. In contrast, lower modulation frequency leads to noise increase due to low signal selectivity. Furthermore, thermal diffusion length also depends on the modulation frequency and can be expressed as follows:

$$\mu = \sqrt{\frac{k}{\pi C \rho f}} \qquad (3-1)$$

where $\kappa$ is the thermal conductivity, $C$ is the specific heat, $\rho$ is the density of the solvent, and $f$ is the modulation frequency.[6] Figure 3-2 shows the signal intensity and the S/N ratio versus modulation frequency. The signal intensity is inversely proportional to the modulation frequency, which is well consistent with the general tendency of PTS.[7] The S/N ratio reached a maximum value at around 1.1 kHz modulation. The calculated thermal diffusion length in water at 1.1 kHz modulation frequency was about 6 μm, much longer than the width and depth of nanochannels. Thus, much of the generated heat diffuse to the glass substrate.

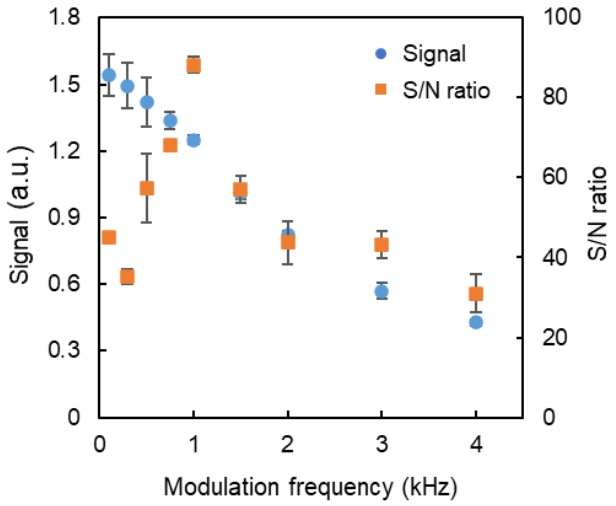


*Figure 3-2. Signal intensity and the S/N ratio versus modulation frequency. Reproduced with permission. (P148, [3]) Copyright 2020, American Chemical Society.*

### 3.2.2 Verification of Concentration Determination

Next, the detection performance of the POD for the concentration determination of solutions in nanochannels was evaluated at the optimized experimental condition. Figure 3-3 shows the calibration curve for the Sunset Yellow aqueous solution in nanochannels with 400 nm wide and deep. The power of the excitation laser was set to 50 mW. The concentration could be determined in the order of $10^{-5}$ M. The calculated LOD was 2.5 μM which corresponds to an average of 330 molecules in the detection volume of 0.23 fL. No other photothermal detection method realized concentration determination in $10^2$ nm channels in such high detection performance.

The POD was also applied to a nanocapillary with 12 cm length and 460 nm inner diameter. Concentration determination was successfully realized with a limit of detection of 12 μM (1600 molecules in the detection volume of 0.22 fL). Thus, the POD can be applied to any form of a diffractive object. The LOD might be improved by the optimization of the experimental system for nanocapillary.

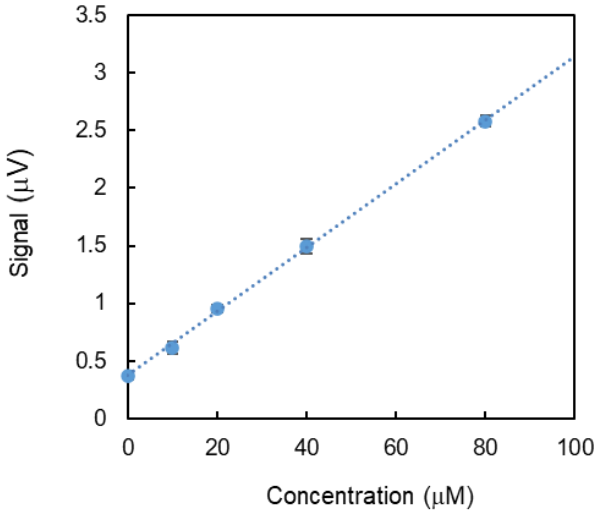


*Figure 3-3. Calibration curve for sunset yellow aqueous solution in 400 nm wide and deep channel.*

### 3.2.3 Comparison with Conventional PTS

*Comparison of POD and DIC-TLM by Experiments*

To confirm that the POD can be applied to nanochannels without sensitivity degradation which is reported for conventional PTS (DIC-TLM),[8] detection performance was measured at an optimized experimental condition for nanochannels with five different sizes ranging from 200 nm wide and deep to 1200 nm wide and deep. The power of the excitation laser was attenuated to 8 mW to avoid photodecomposition. Calibration curves for five different channels are shown in Fig. 3-4. Each calibration curve showed good linearity, and the sensitivity, the slope of the calibration curve decreased as the channel size became smaller. The sensitivity decrease is mainly due to the detection volume decrease: a decrease in the number of target molecules in the laser focus. The limit of detection (LOD) was calculated from calibration curves which were defined as a concentration that gives a signal equivalent to blank +3$\sigma$, and $\sigma$ is calculated from the

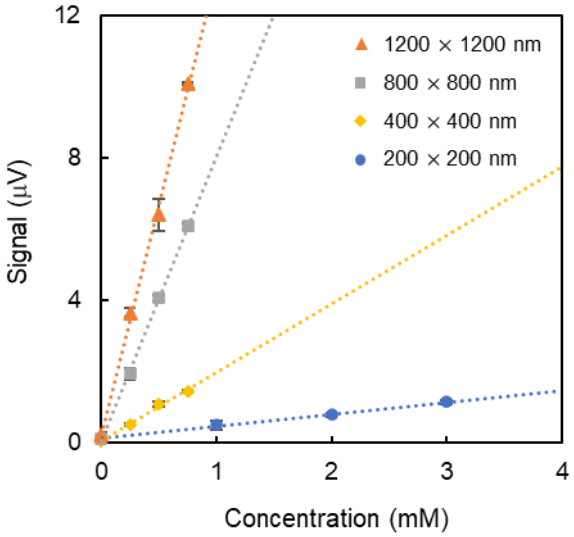


*Figure 3-4. Calibration curve for nanochannels with four different widths and depths. deep channel. Reproduced with permission. (P148, [1]) Copyright 2020, American Chemical Society.*

average signal fluctuation of the sample with the lowest concentration. The detection performance of DIC-TLM was also measured at the equivalent experimental condition and compared. Experimental results are shown in Fig. 3-5. The LOD of DIC-TLM increased for smaller channels, meaning the degradation of detection performance. This is due to the thermal loss and cancelation effect as explained above. In contrast, the LOD of the POD was almost constant even in the measured size range. These results suggest that the detection principle of the POD enables sensitive molecular detection even for ultra-small channels without performance degradation.

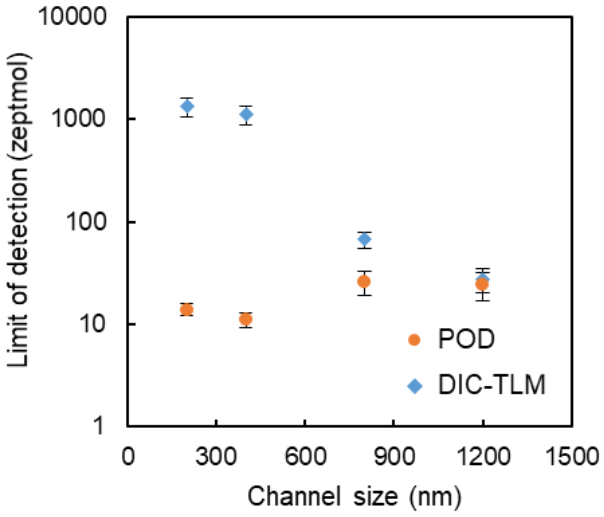


*Figure 3-5. Comparison of the detection performance for the POD and the DIC-TLM. The limit of detection was plotted for each channel size. Reproduced with permission. (P148, [1]) Copyright 2020, American Chemical Society.*

*Procedure for Comparison by Thermal Simulation*

Furthermore, the effect of channel size was investigated for the POD and the DIC-TLM utilizing thermal simulation by COMSOL Multiphysics 5.4. Figure 3-6 shows the geometry of nanochannels and probe and excitation lasers for the thermal simulation. The heat source distribution $Q(r, z, t)$ by the photothermal effect of target molecules in the nanochannel is described as follows:[9]

$$Q(r,z,t) = \frac{2P\alpha}{\pi^2\omega_{ex}^2}\exp(-\alpha z)\,exp\left(-\frac{2r^2}{\omega_{ex}^2}\right)\{1+cos(2\pi ft)\} \qquad (3-2)$$

$$\omega_{ex}^2 = \omega_{0,ex}^2\left(1+\frac{z^2}{z_{r,ex}^2}\right) \qquad (3-3)$$

where $P$ [W] is the excitation laser intensity, $\alpha$ [$m^{-1}$] is the absorption coefficient of the sample, $f$ [Hz] is the modulation frequency, $\omega_{0,ex}$ [m] is the waist radius of the excitation beam, and $z_{r,ex}$ [m] is the Rayleigh length of the excitation beam. This thermal source distribution is applied only inside the nanochannel. The thermal distribution $T(r, z, t)$ was

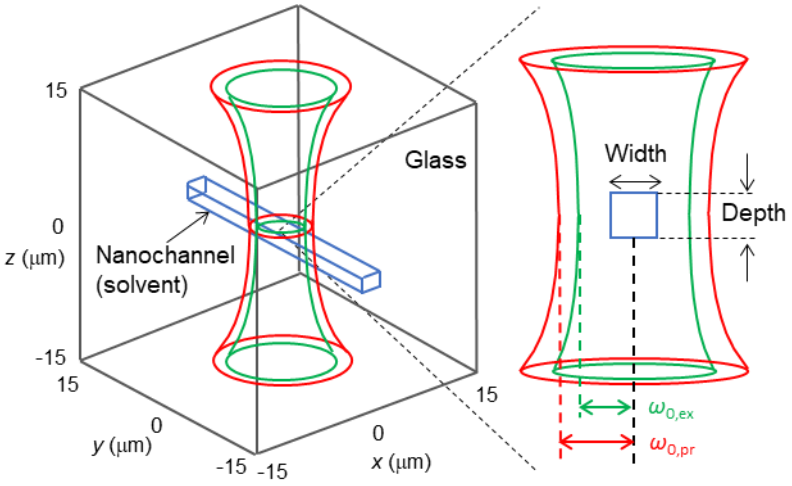


*Figure 3-6. The geometry of nanochannels and probe and excitation lasers for the thermal simulation.*

calculated by solving the heat conduction equation in the time-dependent model. The POD signal is roughly estimated by the difference of average refractive index change between the solvent region and the glass substrate region. Therefore, the relative POD signal is calculated from the integrated value of the refractive index change weighted by probe laser intensity. The integral values for the solvent $S(t)_s$ and the glass $S(t)_g$ are described as follows:

$$S(t)_{s/g} = \int \left(\frac{dn}{dT}\right)_{s/g} \{T(r,z,t) - T_0\} \left(\frac{\omega_{0,pr}}{\omega_{pr}}\right)^2 exp\left(-\frac{2r^2}{\omega_{pr}^2}\right) dV \qquad (3-4)$$

$$\omega_{pr}^2 = \omega_{0,pr}^2 \left(1 + \frac{z^2}{z_{r,pr}^2}\right) \qquad (3-5)$$

where $T_0$ [K] is the initial temperature, $\omega_{0,pr}$ [m] is the waist radius of the probe laser, $z_{r,pr}$ [m] is the Rayleigh length of the probe laser, and d$n$/d$T$ is the temperature coefficient of the refractive index. Note that the integral region is different for the solvent and the glass substrate. The relative POD signal $\Delta S(t)$ is defined as the difference of $S(t)_s$ and $S(t)_g$.

$$\Delta S(t) = \int \left|\frac{dn}{dT}\right| \{T(r,z,t) - T_0\} \left(\frac{\omega_{0,pr}}{\omega_{pr}}\right)^2 exp\left(-\frac{2r^2}{\omega_{pr}^2}\right) dV \qquad (3-6)$$

In Eq. (3-6), the value of d$n$/d$T$ varies based on the integral region. Since the heat source distribution has a component oscillating with the modulation frequency, $\Delta S(t)$ also oscillates at the same frequency. Therefore, the maximum value of $\Delta S(t)$ was defined as a POD signal. The above calculation after thermal simulation ignores the optical properties of solvents and indirectly estimates the POD signal. For the precise simulation of the absolute POD signal, the thermal diffusion simulation and laser propagation simulation should be combined while such calculation is a little difficult for the current simulation system.

On the contrary, the relative DIC-TLM signal $\Delta S'(t)$ is defined as follows based on the previous reports.[8]

$$\Delta S'^{(t)} = S'(r = 0\ \mu m, t) - S'(r = 5\ \mu m, t) \qquad (3-7)$$

$$S'(r,t) = \int \frac{dn}{dT}\{T(r,z,t) - T_0\}\left(\frac{\omega_{0,pr}}{\omega_{pr}}\right)^2 exp\left\{-\frac{2(r-r')^2}{\omega_{pr}^2}\right\} dV \qquad (3-8)$$

As with the case of the POD, the maximum value of $\Delta S(t)$ was defined as DIC-TLM signal. Note that calculated POD signals and DIC-TLM signals cannot be directly compared because the above calculation estimates the relative values by a different procedure. Thus, the above calculations provide a comparison of the tendency of the signal intensity of each detection method for different channel sizes.

*Comparison of POD and DIC-TLM by Thermal Simulation*

Figure 3-7 (a) shows the calculated POD signal intensity versus channel size and Fig. 3-7 (b) shows the calculated DIC-TLM signal intensity versus channel size. To evaluate the thermal loss and glass effect by thermal diffusion to glass substrates, signals without thermal loss effect and signals without glass effect were also plotted. Signals without thermal loss effect were calculated by changing d$n$/d$T$ of glass to that of water. Signals without glass effect were calculated by subtracting signals from glass substrates. In the POD, signal intensity decrease by thermal loss effect was partially compensated by glass effect because the refractive index change of glass substrates contributed to the POD signal, leading to little sensitivity decrease for smaller channels. In contrast, the DIC-TLM signal was further decreased by the glass effect because the refractive index change of glass substrates canceled the phase shift, leading to a large sensitivity decrease for smaller channels. To clarify the thermal loss effect and glass effect in detail, the

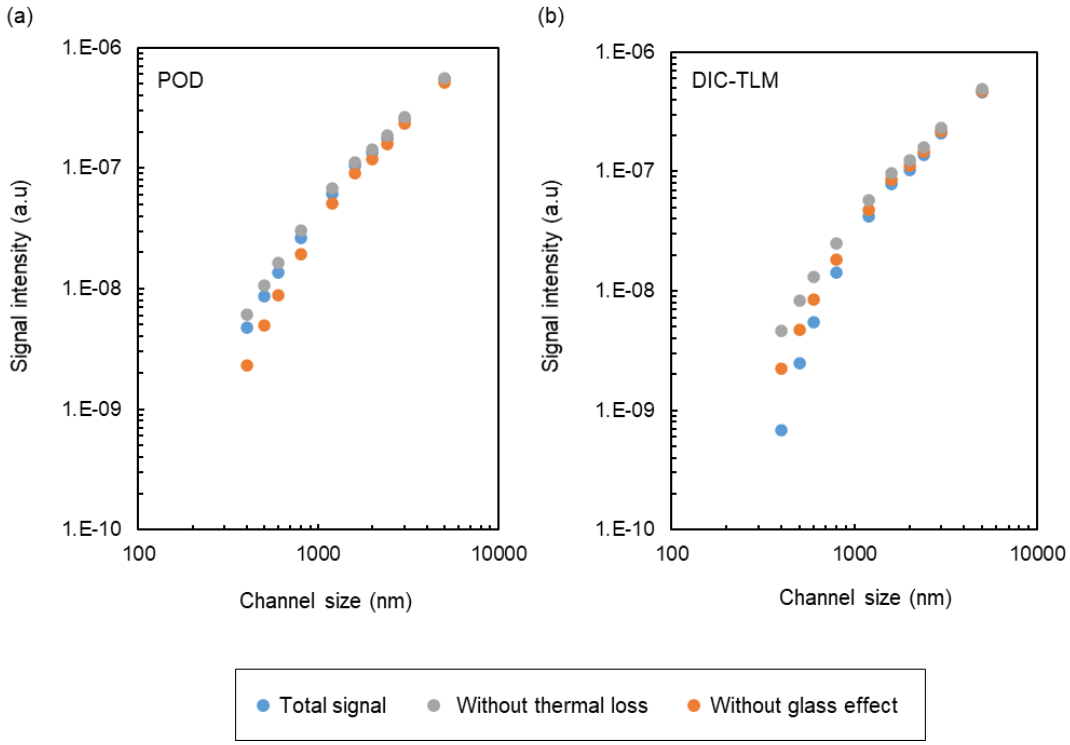


*Figure 3-7. Calculated signal intensity versus channel size for (a) the POD and (b) the DIC-TLM.*

contributions of thermal loss effect and glass effect was summarized in Fig. 3-8. The difference of compensation and cancellation by glass substrate largely affects the tendency of the signal intensity for smaller channels. These results were in good agreement with experimental results.

As shown in the above experimental results and thermal simulations, each signal intensity decreased for smaller channels which might be mainly due to the decrease of detection volume, a smaller number of molecules in smaller channels. To elucidate the factor in detail, the slope for the log-log plot was measured for experiments and thermal simulations and summarized in Table 3-1. Without the thermal loss effect, the slope of the POD and the DIC-TLM was 2.2–2.3, meaning the detection volume loss (1.0 for width

and depth) was the main factor. Including the thermal loss effect, each slope was estimated to be 3.0, meaning the thermal loss effect was proportional to the channel size. The total slope was 2.4 for the POD and 4.3 for the DIC-TLM, which was well consistent with experimental results (2.0 for the POD and 4.3 for the DIC-TLM) Thus, the glass effect was -0.6 for the POD and 1.2 for the DIC-TLM. These results show that the detection principle of the POD enables sensitive molecule detection for $10^1$–$10^2$ nm channels without large degradation of detection performance.

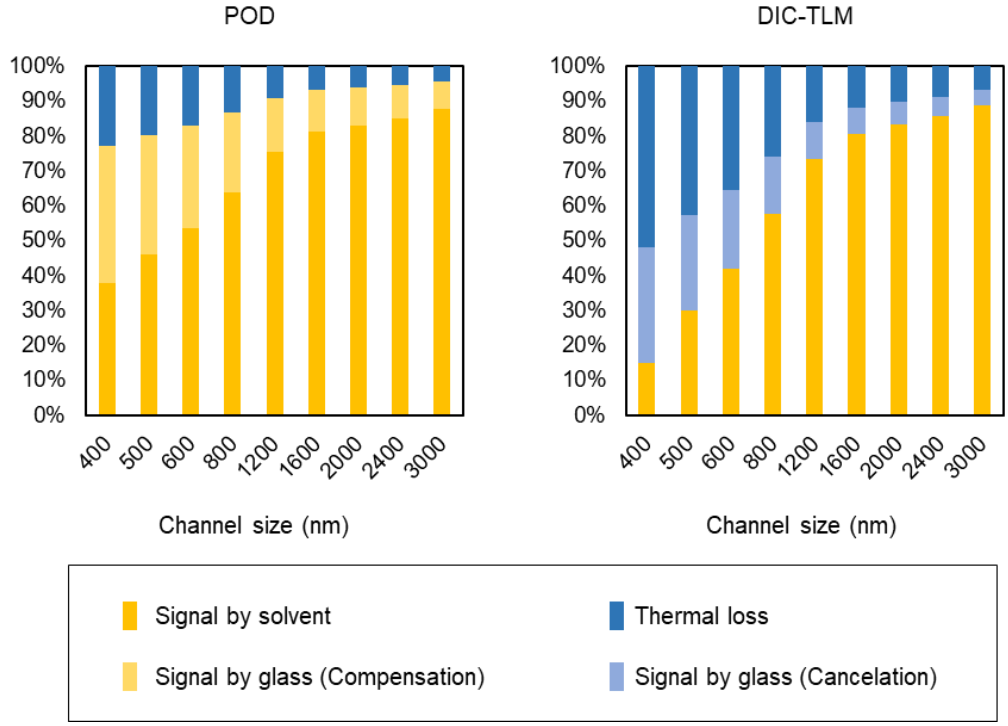


*Figure 3-8. Contributions of thermal loss effect and glass effect for the POD and the DIC-TLM.*

*Table 3-1. Summary of slope for the log-log plot thermal simulations and experimental results.*

| | POD | DIC-TLM |
|---|---|---|
| Calculation without thermal loss | 2.2 | 2.4 |
| Calculation including thermal loss | 3.0 | 3.0 |
| Calculation including glass effect | 2.4 | 4.3 |
| Experimental results | 2.0 | 4.3 |

## 3.3 Development of Solvent-enhanced POD

### 3.3.1 Theory of Solvent Enhancement Effect

Although the POD realized non-fluorescent molecule detection in $10^2$ nm channels, the measured concentration range of nonfluorescent molecules was in the order of μM ($10^2$−$10^4$ molecules), and further performance improvement is strongly required for concentration determination at a countable molecular level. Solvent enhancement effect is one of the methods to significantly improve the sensitivity of PTS.[7] Generally, the sensitivity of PTS can be improved by utilizing organic solvents with high thermal response, while the relationship between the sensitivity of the POD and thermal properties of solvents is unknown. Different from other photothermal detection methods, the optical properties of solvents also affect the POD signal, further complicating the effect of solvents. In addition to this, several unique liquid properties in nanochannels might affect the detection performance of the POD. Therefore, the solvent enhancement effect for the POD was estimated by thermal simulations and optical calculations.

To explain the signal enhancement by photothermal factor and diffraction factor, six different solvents: water, ethanol, acetonitrile, hexane, toluene, and chloroform were selected. Table 3-2 shows the thermal/optical properties of the selected solvents, where $n_s$ is the refractive index, d$n$/d$T$ is the temperature coefficient of the refractive index, $\kappa$ is the thermal conductivity, and $\alpha$ is the thermal diffusivity.[7] Generally, solvents with low $\alpha$ and high d$n$/d$T$ give high photothermal signals. Therefore, organic solutions will give a higher signal than aqueous solutions. The photothermal factor of organic solvents compared with aqueous solutions can be calculated by thermal simulations mentioned in 3.2.3. Figure 3-

*Table 3-2. Thermal/optical properties of the selected solvents.*[7]

| Solvent | $n_s$ | d$n$/d$T$ ($\times 10^{-4}$ /K) | k (W/m·K) | a ($\times 10^{-8}$ m$^2$/s) |
|---|---|---|---|---|
| Water | 1.33 | -0.91 | 0.60 | 14.3 |
| Ethanol | 1.36 | -4.00 | 0.17 | 8.8 |
| Acetonitrile | 1.34 | -4.55 | 0.21 | 20.7 |
| Hexane | 1.38 | -5.20 | 0.12 | 8.4 |
| Toluene | 1.50 | -5.68 | 0.14 | 9.2 |
| Chloroform | 1.44 | -6.03 | 0.12 | 8.1 |

9 shows the typical example of the results of thermal simulations. A large temperature rise was obtained for organic solvents. The calculated enhancement factor indicates that 3–6 times sensitivity improvement will be gained by utilizing organic solvents. Detailed values for each solvent are shown in the next section.

The optical properties of solvents also affect the sensitivity of the POD because optical diffraction by nanochannels largely depends on the refractive index of the solvent in the nanochannel. As mentioned in 2.3.1, for detection systems utilizing optical diffraction by single nanochannel, the signal (diffracted light intensity change: $\Delta P_D$) is approximately expressed as follows:

$$\Delta P_D \approx \frac{2P_D|\Delta n_s - \Delta n_g|}{|n_s - n_g|} \qquad (3-9)$$

where $n_s$ is the refractive index of the solvent in the channel, and $n_g$ is the refractive index of the glass. Note that the spatial distribution of $\Delta n_s$ and $\Delta n_g$ needs to be considered for accurate calculation of the POD signal. This equation indicates that solvents which refractive index is close to that of glass will give a higher signal. For example, toluene

solutions will give a 3.2 times higher signal than an aqueous solution. Although the value of $P_D$ also depends on the refractive index of solvents, $P_D$ is easily adjusted by changing the probe laser intensity.

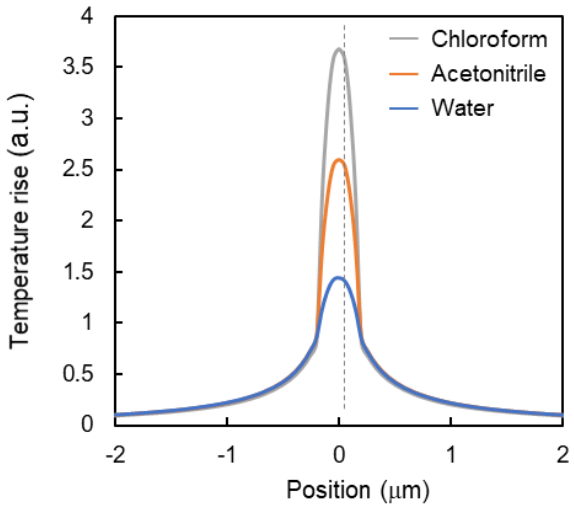


*Figure 3-9. Calculated temperature distribution perpendicular to the 400 nm wide and deep nanochannel at z=0 for different solvents.*

### 3.3.2 Verification of Solvent-enhanced POD

To confirm the signal enhancement by photothermal factor and diffraction factor, detection performance for the above six solvents (water, ethanol, acetonitrile, hexane, toluene, and chloroform) was investigated. The thermal enhancement factor was estimated from the sensitivity difference between water, ethanol, and acetonitrile solution because they have a similar refractive index. The optical enhancement factor was estimated from the sensitivity difference between hexane, toluene, and chloroform because these solvents have similar thermal properties. As a solute for acetonitrile, hexane, toluene, and chloroform, Sudan IV ($\varepsilon$=17700 $M^{-1}cm^{-1}$ for 532 nm excitation) was used due to high solubility, and Sunset Yellow FCF ($\varepsilon$=4700 $M^{-1}cm^{-1}$ for 532 nm excitation) was used for water and ethanol. To eliminate the effect of the difference of solutes, the sensitivity of Sunset yellow FCF in acetonitrile solution was also measured and the sensitivity for each solvent was normalized by that of acetonitrile. The initial diffracted light intensity ($P_D$) is not constant for solvents with different refractive indices. Therefore, $P_D$ was adjusted to an optimized value (15 mV) for all solvents by changing probe laser intensity.

Figure 3-10 (a) shows the calibration curves for four organic solvents. The size of the used nanochannels was 400 nm deep and wide. In repeated experiments, the variation of blank signals (0 μM) from day to day and device to device, was observed. However, the variation showed little effect on sensitivity. Therefore, blank signal for each solution was adjusted to 0 μV. Linear calibration curves were obtained for all solvents. Figure 3-10 (b) shows the normalized sensitivity for each solvent. The calculated values are also shown for comparison. Experimental results were almost consistent with the calculated values, suggesting that unique liquid properties of water in nanochannels have little effect

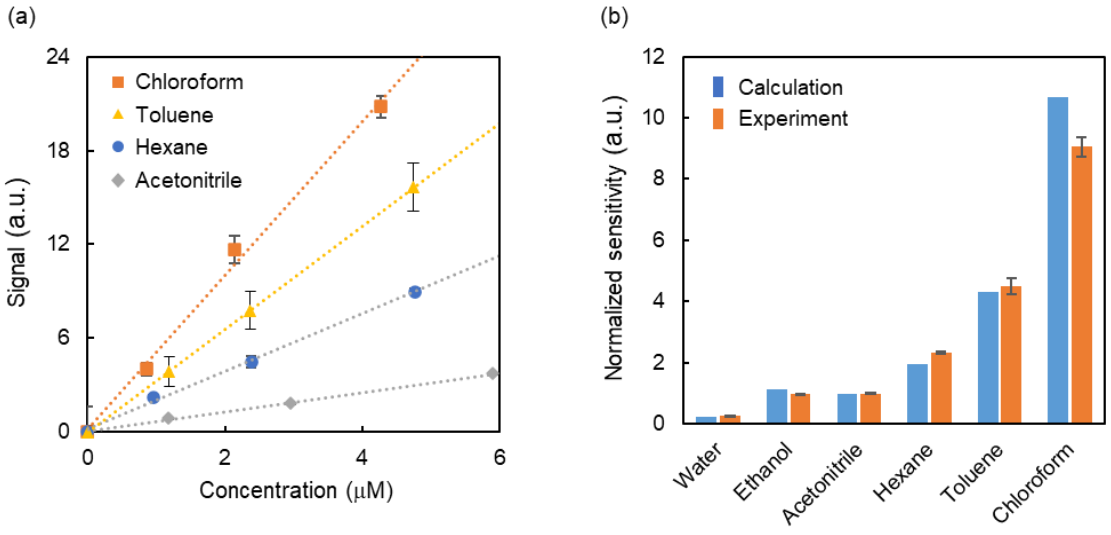


*Figure 3-10. (a) Calibration curve for four organic solvents. (b) Comparison of sensitivity for each solvent. Each sensitivity was normalized based on the sensitivity of the acetonitrile solution. Reproduced with permission. (P148, [3]) Copyright 2020, American Chemical Society.*

on the POD signal. Ethanol and acetonitrile solution showed 3.6–3.7 times higher sensitivity than the aqueous solution, suggesting the enhancement effect by photothermal factor. This enhancement effect is relatively small judging from high $\Delta T$ (×1.7−1.8) and d$n$/d$T$ (×4.4−5.0) of ethanol and acetonitrile, indicating thermal diffusion and temperature change of glass substrates also contributes to the sensitivity. Toluene and chloroform solutions showed 1.9 times and 3.8 times higher sensitivity than hexane solution, suggesting the enhancement effect by diffraction factor. The enhancement factor of organic solvents relative to water is summarized in Table 3-3. Compared with the aqueous solution, more than 30 times sensitivity improvement was realized by organic solvents. This tendency is different from those for conventional PTS,[7] suggesting that both thermal and optical properties of solvents contribute to the sensitivity of the POD. A little difference between calculations and experiments might be derived from the

*Table 3-3. Summary of the enhancement factor of five different solvents relative to water.*

| Solvent | Diffraction factor | Photothermal factor | Total (Calc.) | Total (Exp.) |
|---|---|---|---|---|
| Ethanol | ×1.3 | ×3.8 | ×4.8 | ×3.6 |
| Acetonitrile | ×1.1 | ×3.8 | ×4.2 | ×3.7 |
| Hexane | ×1.5 | ×5.4 | ×8.3 | ×8.6 |
| Toluene | ×3.2 | ×5.7 | ×18.2 | ×16.5 |
| Chloroform | ×7.5 | ×6.0 | ×45.0 | ×33.0 |

approximations in simulations and calculations.

Finally, the detection performance of the POD at the optimized condition was evaluated. Although chloroform solutions showed the highest sensitivity among six selected solvents, signal variation and noise also increased. This might be due to the high responsiveness for unexpected refractive index fluctuation. Therefore, detection performance for hexane solutions was evaluated at a low concentration range. Figure 3-11 shows the calibration curve for Sudan IV hexane solution in the nanochannel with 400 nm wide and deep. The average number of molecules in the detection volume was calculated from the concentration. The concentration determination was realized in the order of nM (10–100 molecules). The calibration curve showed good linearity in the measured concentration range. The calculated LOD was 75 nM, which corresponds to an average of 10 molecules in the detection volume of 0.23 fL. By the solvent enhancement effect, label-free concentration determination in $10^2$ nm channels at a countable molecular level by the POD was realized for the first time. Note that concentration determination

measures the average number of molecules in the detection volume, not the total number of molecules passing through the detection region. Thus, further sensitivity increase is necessary for single or countable molecular detection. The LOD of the solvent-enhanced POD is higher than that of previously reported thermal lens detection for microchannels.[10] In the previous experiment, the detection volume was calculated from the confocal volume of the excitation laser, which underestimated the number of molecules contributing to the signal. In this experiment, the detection volume was calculated from the excitation beam spot diameter and the channel size, which enables a more accurate estimation of the number of molecules contributing to the signal.

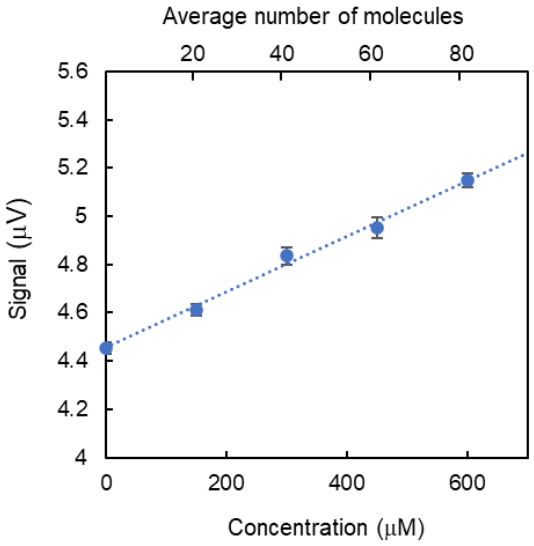


*Figure 3-11. Calibration curve for Sudan IV hexane solution. The average number of molecules was calculated from the concentration and the detection volume.*

### 3.4 Concentration Determination in $10^1$ nm Channel

#### 3.4.1 Optical Diffraction by $10^1$ nm Channel

Finally, concentration determination in $10^1$ nm channels was demonstrated. First, $10^1$ nm channels were fabricated, and optical diffraction by a single $10^1$ nm channel was confirmed. Since the size of $10^1$ nm channels is much smaller than the wavelength of visible light, we might consider the scattering effect.[11] Thus, there is a possibility that the above theoretical calculations based on the diffraction theory cannot be applied to $10^1$ nm channels. Sub-100 nm wide and deep were fabricated on a fused-silica glass substrate using electron-beam lithography (F7000S, Advantest Corp., Japan) and reactive-ion etching. Figure 3-12 shows the SEM images of nanochannels with 70 nm wide and 60 nm deep taken by Regulus8230 (Hitachi High-Tech Corp., Japan). The sample stage was tilted 45 degrees. The gap of nanochannels was designed to 700 nm for easy observation. For experiments, the gap of nanochannels was set to 50 μm to measure optical diffraction by a single nanochannel. Sub-100 nm wide and deep were successfully fabricated. Figure 3-13 shows diffracted light intensity for nanochannels with 70–400 nm wide and 60 nm deep. The calculated values by the theoretical formula described in chapter 2 were also

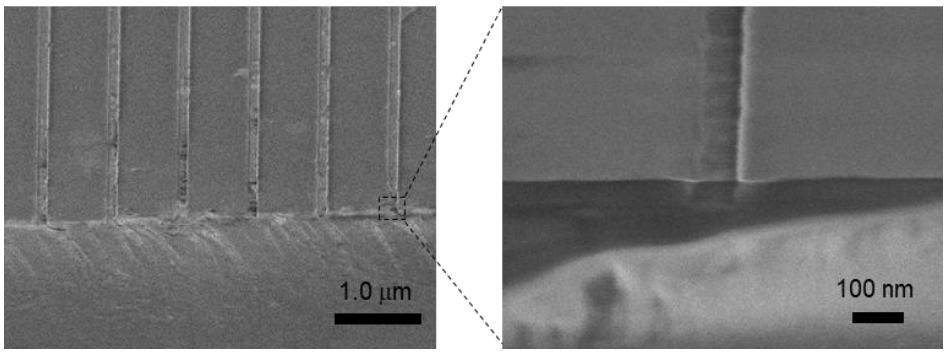


*Figure 3-12. Typical SEM image of fabricated sub-100 nm channels. The sample stage was tilted 45 degrees.*

plotted. To compare the theoretical calculations and experimental results, calculated and experimental values were normalized by their maximized value. Experimental results show good agreement with theoretical ones; optical diffraction is dominant even for nanochannels with 70 nm wide and deep. As predicted from theoretical calculations, the diffracted light intensity ($P_D$) greatly decreased for smaller channels. Although the decrease of $P_D$ leads to low signal intensity, the problem can be easily solved by using a high-power probe laser. Thus, the detection principle of the POD can be applied to $10^1$ nm channels. Note that more precise position control of the nanochannels was necessary for $10^1$ nm channels.

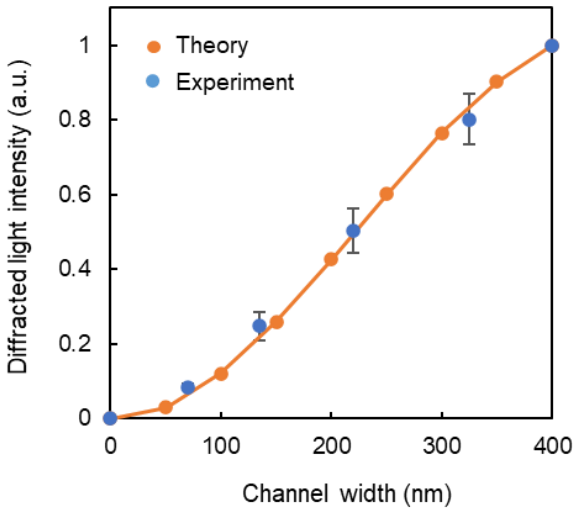


*Figure 3-13. Comparison of normalized diffracted light intensity versus channel width for theory and experiment.*

### 3.4.2 Evaluation of Detection Performance

To verify the POD can be applied to $10^1$ nm channels, the effect of channel size on the detection performance was investigated. As a test sample, Sunset Yellow FCF aqueous solution was introduced to nanochannels. The initial diffracted light intensity ($P_D$) was adjusted to 15 mV for all channels by tuning probe laser intensity to eliminate the effect of the background and noise of the probe laser. First, the relationship between channel depth and detection performance was investigated. The measured range of channel depth was 60–370 nm, and the channel width was fixed to 400 nm. The calibration curve for each channel size is shown in Fig. 3-14 (a). The calibration curve showed good linearity even for the 60 nm deep channel. The calculated LOD was 26 μM, which corresponds to 590 molecules in a detection volume of 38 aL. Figure 3-14 (b) shows the sensitivity for each channel depth. The sensitivity decreased for shallow channels, and the calculated slope was 1.5. Considering the effect of detection volume which is proportional to channel depth, the effect of thermal diffusion to glass substrates is estimated to be 0.5. Although

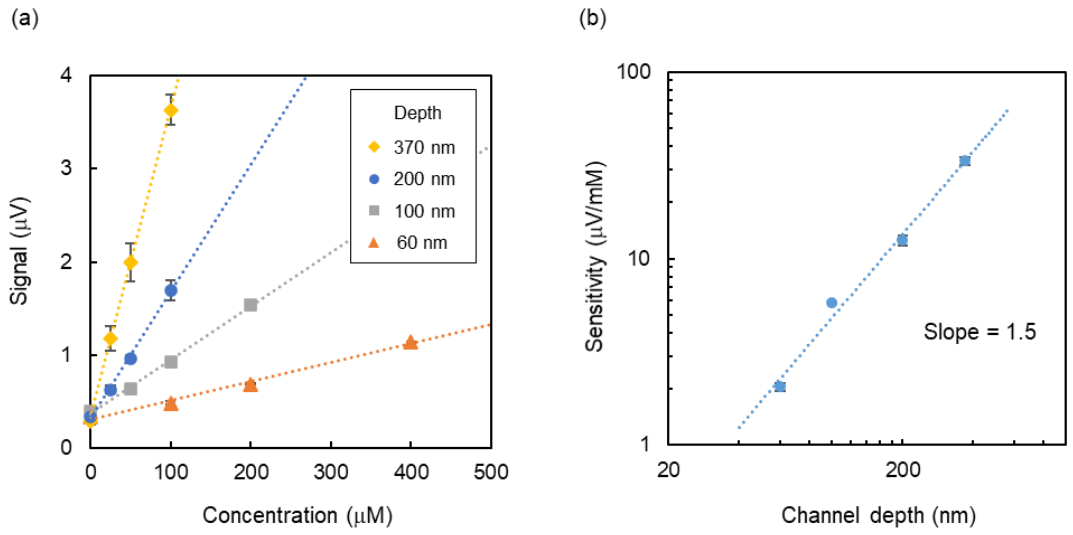


*Figure 3-14. (a) Calibration curves for nanochannels with different channel depths. (b) Sensitivity (slope of the calibration curve) versus channel depth.*

a slight sensitivity decrease was observed, the POD can be applied to nanochannels with $10^1$ nm depth.

Next, the relationship between channel width and detection performance was investigated. The measured range of channel width was 70–400 nm, and the channel depth was fixed to 70 nm. The calibration curve for each channel size is shown in Fig. 3-15 (a). The calibration curve showed good linearity even for the nanochannel with 70 nm wide and deep. The calculated LOD was 300 μM, which corresponds to 1200 molecules in a detection volume of 7 aL. These results suggest that the POD can be applied to chemical/biological analyses in $10^1$ nm channels. Figure 3-15 (b) shows the sensitivity for each channel depth. The sensitivity decreased for shallow channels, and the calculated slope was 1.3. Considering the effect of detection volume which is proportional to channel width, the effect of thermal diffusion to glass substrates is estimated to be 0.3. The sensitivity decrease for smaller channels can be explained as follows. Although the refractive index change of glass substrates also contributes to the POD signal, the thermal

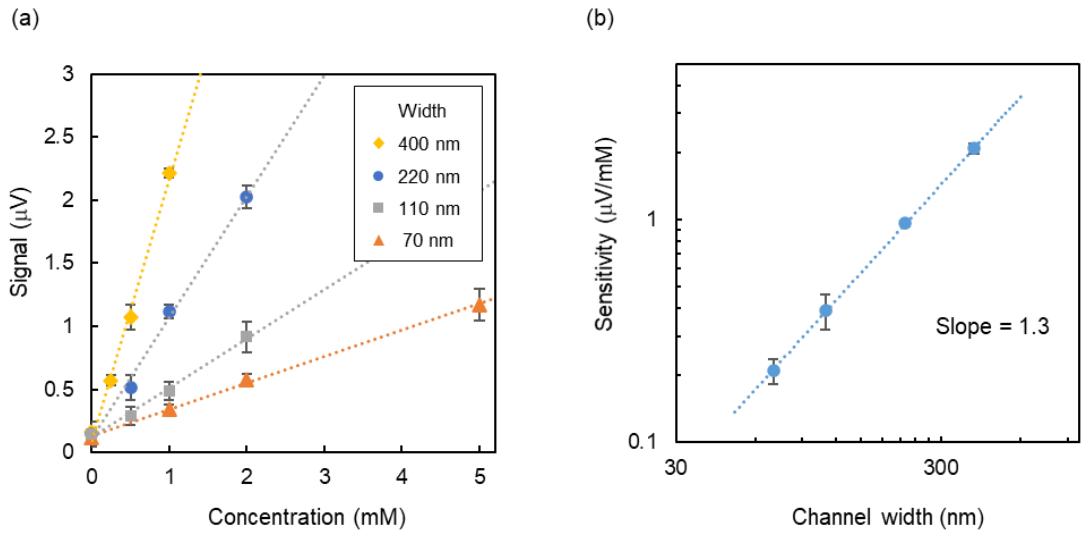


*Figure 3-15. (a) Calibration curves for nanochannels with different channel widths. (b) Sensitivity (slope of the calibration curve) versus channel width.*

loss effect is dominant for $10^1$ nm channels due to ultra-small volume. Thus, the thermal loss effect cannot be fully compensated by the glass effect.

Finally, concentration determination at a countable molecular level in $10^1$ nm channels was demonstrated by the solvent enhancement effect. Figure 3-16 shows the calibration curve of Sudan IV in acetonitrile solution for 70 nm wide and deep nanochannel. The calculated LOD was 7.8 μM, which corresponds to 30 molecules in the detection volume of 7 aL. Thus, the POD realized concentration determination at a countable molecular level even in $10^1$ nm channels. The lower LOD compared with that of 400 nm wide and deep nanochannel might be due to the improvement of experimental conditions and optical systems.

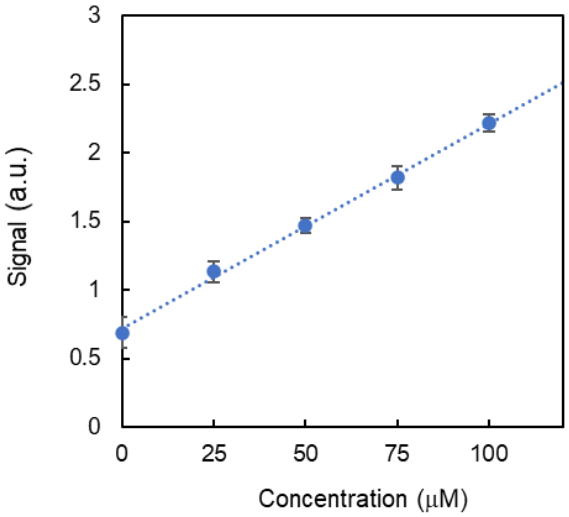


*Figure 3-16. Calibration curve of Sudan IV in acetonitrile solution for 70 nm wide and deep nanochannel.*

## 3.5 Summary

In this chapter, concentration determination in $10^1$–$10^2$ nm channels by the POD was verified for the first time. At the optimized experimental conditions, the POD enabled concentration determination of non-fluorescent molecules with the LOD of 2.5 μM, corresponding to 330 molecules (0.55 zeptomol) in the detection volume of 0.23 fL. Different from conventional PTS, the detection principle of the POD enabled concentration determination in $10^2$ nm channels without degradation of the detection performance. By utilizing the solvent enhancement effect, the detection performance of the POD was further improved, and label-free concentration determination in $10^2$ nm channels at a countable molecular level (LOD: 10 molecules) was realized. Finally, the POD was applied to $10^1$ nm channels. For nanochannels with 70 nm wide and deep, concentration determination was demonstrated with the LOD of 1200 molecules for aqueous solutions and 30 molecules for organic solutions. Although the diffracted light intensity largely decreases for even smaller nanochannels, this problem can be solved by using a probe laser with a shorter wavelength because the diffracted light intensity is proportional to the $-4^{th}$ power of the wavelength. Thus, the POD can be applied to concentration determination in $10^1$–$10^2$ nm channels and chemical/biological analyses in such ultra-small spaces.

## 3.6 References of Chapter 3


1. Szöko, É. & Tábi, T. Analysis of biological samples by capillary electrophoresis with laser induced fluorescence detection. *J. Pharm. Biomed. Anal.* **53**, 1180–1192 (2010).
2. Shera, E. B., Seitzinger, N. K., Davis, L. M., Keller, R. A. & Soper, S. A. Detection of single fluorescent molecules. *Chem. Phys. Lett.* **174**, 553–557 (2000).
3. Joo, C., Balci, H., Ishitsuka, Y., Buranachai, C. & Ha, T. Advances in Fluorescence Methods for Molecular Biology. *Annu. Rev. Biochem.* **77**, 51–76 (2008).
4. Duan, C. *et al.* Label-Free Electrical Detection of Enzymatic Reactions in Nanochannels. *ACS Nano* **10**, 7476–7484 (2016).
5. Kang, S., Nieuwenhuis, A. F., Mathwig, K., Mampallil, D. & Lemay, S. G. Electrochemical single-molecule detection in aqueous solution using self-aligned nanogap transducers. *ACS Nano* **7**, 10931–10937 (2013).
6. Shimizu, H., Mawatari, K. & Kitamori, T. Sensitive determination of concentration of nonfluorescent species in an extended-nano channel by differential interference contrast thermal lens microscope. *Anal. Chem.* **82**, 7479–7484 (2010).
7. Bialkowski, S. E. *Photothermal Spectroscopy Methods for Chemical Analysis*. (John Wiley & Sons, 1995).
8. Shimizu, H., Miyawaki, N., Asano, Y., Mawatari, K. & Kitamori, T. Thermo-optical Characterization of Photothermal Optical Phase Shift Detection in Extended-Nano Channels and UV Detection of Biomolecules. *Anal. Chem.* **89**, 6043–6049 (2017).
9. Jackson, W. B., Amer, N. M., Boccara, A. C. & Fournier, D. Photothermal deflection spectroscopy and detection. *Appl. Opt.* **20**, 1333–1344 (1981).
10. Tokeshi, M., Uchida, M., Hibara, A., Sawada, T. & Kitamori, T. Determination of subyoctomole amounts of nonfluorescent molecules using a thermal lens microscope: Subsingle-molecule determination. *Anal. Chem.* **73**, 2112–2116 (2001).
11. van de Hulst, H. C. *Light scattering by small particles*. (Courier Corporation, 1981).

# Chapter 4. Nanoparticle Counting

## 4.1 Introduction

In chapter 3, the detection performance of the POD was improved and evaluated, and concentration determination of non-fluorescent molecules in $10^1$–$10^2$ nm channels are verified. Another major target of chemical/biological analyses is nanoparticles such as metal nanoparticles, vesicles, viruses, and exosomes. Detection and characterization of these nanoparticles at a single nanoparticle level are important in the fields of semiconductor manufacturing, diagnostics, photothermal therapy, and drug delivery.[1-4] For the detection and characterization of individual nanoparticles, highly sensitive yet high-throughput nanoparticle detection is strongly required. Several nanoparticle detection methods have been developed so far. As direct and accurate observation methods, scanning electron microscopy (SEM) and transmission electron microscopy (TEM) are often used,[5] although these methods are time-intensive. For real-time and high-throughput analyses, individual nanoparticle detection in a fluid is necessary. As an optical detection method, the light-scattering detection method is widely used. By the combination with nanofluidics, sheath flow cytometry, and tracking analysis, detection and size measurement of individual sub-100nm particles have been realized in a fluid.[6-8] As an electrical detection method, resistive pulse sensing (RPS) by nanogaps or nanopores has been realized.[9,10] Although the above methods realized highly sensitive individual nanoparticle detection in liquid, these methods only give morphological information; no chemical or composition information cannot be obtained. In contrast, the POD has the potential to provide chemical information based on the absorbance of nanoparticles. However, it is still unknown that the detection principle of the POD can be applied to nanoparticle detection and characterization in nanochannels.

In this chapter, the detection principle of the POD is applied to nanoparticle

detection for the first time, and the counting-mode POD is realized. First, the detection principle of the counting-mode POD is verified. Then, experimental conditions are optimized, and the detection performance such as sensitivity and counting efficiency is evaluated. Finally, absorption-based size measurement of individual nanoparticles is demonstrated in $10^2$ nm channels.

## 4.2 Principle Verification of the Counting-mode POD

### 4.2.1 Principle of the Counting-mode POD

The detection principle of the counting-mode POD is shown in Fig. 4-1. The outline of the detection principle is the same as the POD. When individual nanoparticles pass through the focus position of the probe and excitation beam, the excitation beam is absorbed by the nanoparticle, followed by heat generation, temperature change, and temporal refractive index change. This temporal refractive index change is measured as a diffracted light intensity change which is monitored with millisecond scale resolution. Thus, individual nanoparticles can be detected as pulse signals.

The important feature of the nanoparticle detection by the counting-mode POD is as follows. First, the counting-mode POD can measure the absorbance of individual

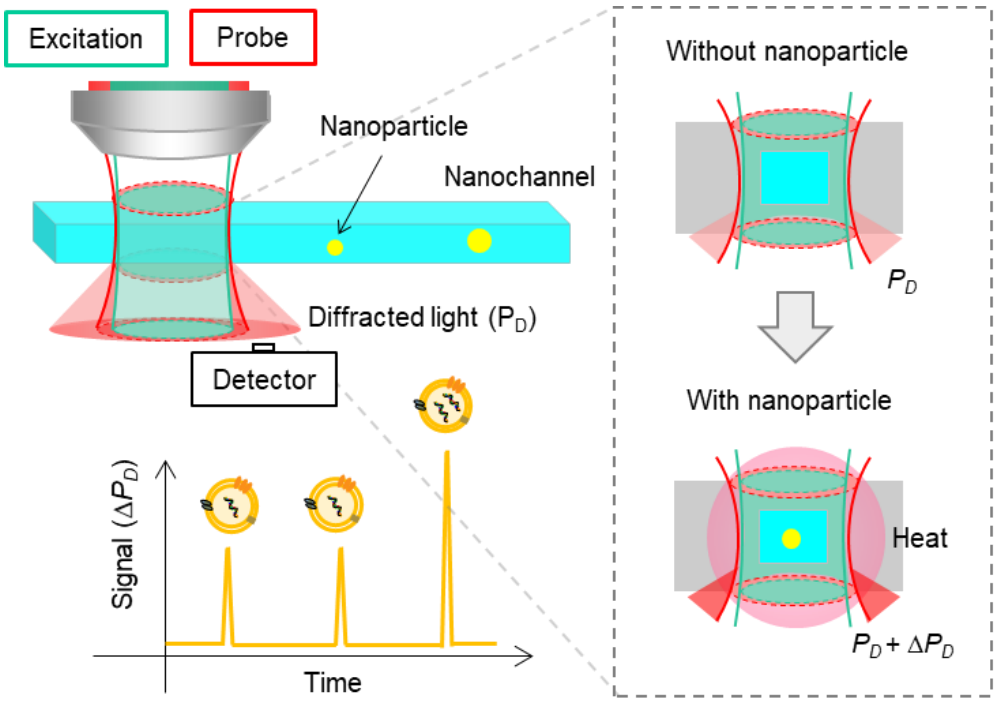


*Figure 4-1. Detection principle of the counting-mode POD.*

nanoparticles and discriminate various kinds of nanoparticles from their photothermal signal intensity. Generally, photothermal detection methods are highly position-sensitive because two focused laser beams are often used. Therefore, a photothermal signal mainly depends on the positions and trajectories of nanoparticles in the optical spots; each pulse signal has little information (size and absorbance) of individual nanoparticles. Thus, although conventional photothermal detection methods can detect individual nanoparticles,[11,12] the characterization of individual nanoparticles is difficult. Different from other photothermal detection methods, the counting-mode POD can be applied to nanochannels which is smaller than the focused excitation beam spot, and all nanoparticles flowing in nanochannels experience almost the same excitation beam intensity. Therefore, the obtained pulse signal has information about the absorbance of the nanoparticle. Second, the counting-mode POD and nanochannels enable high counting efficiency. In the optical configuration of the POD, all nanoparticles introduced to the nanochannel passes through the laser focus, and the detection efficiency defined as the number of detected nanoparticles/total number of introduced nanoparticles is almost 100%. Thus, the concentration of the nanoparticle solution can be calculated from the number of detected nanoparticles divided by the sample volume introduced to the channel without standard samples or laborious calibration procedures.

Figure 4-2 shows the difference between concentration determination mode (chapter 3) and counting mode (chapter 4). For concentration determination mode, the average number of molecules in a detection volume is measured, and sensitive measurement can be realized by long average time. Therefore, a time constant of 1 sec was used in chapter 2. For counting mode, in contrast, individual nanoparticles pass through the detection region within a few milliseconds, and a fast time response is

necessary to obtain pulse signals from nanoparticles without counting loss. Therefore, a time constant of milliseconds was used in chapter 4.

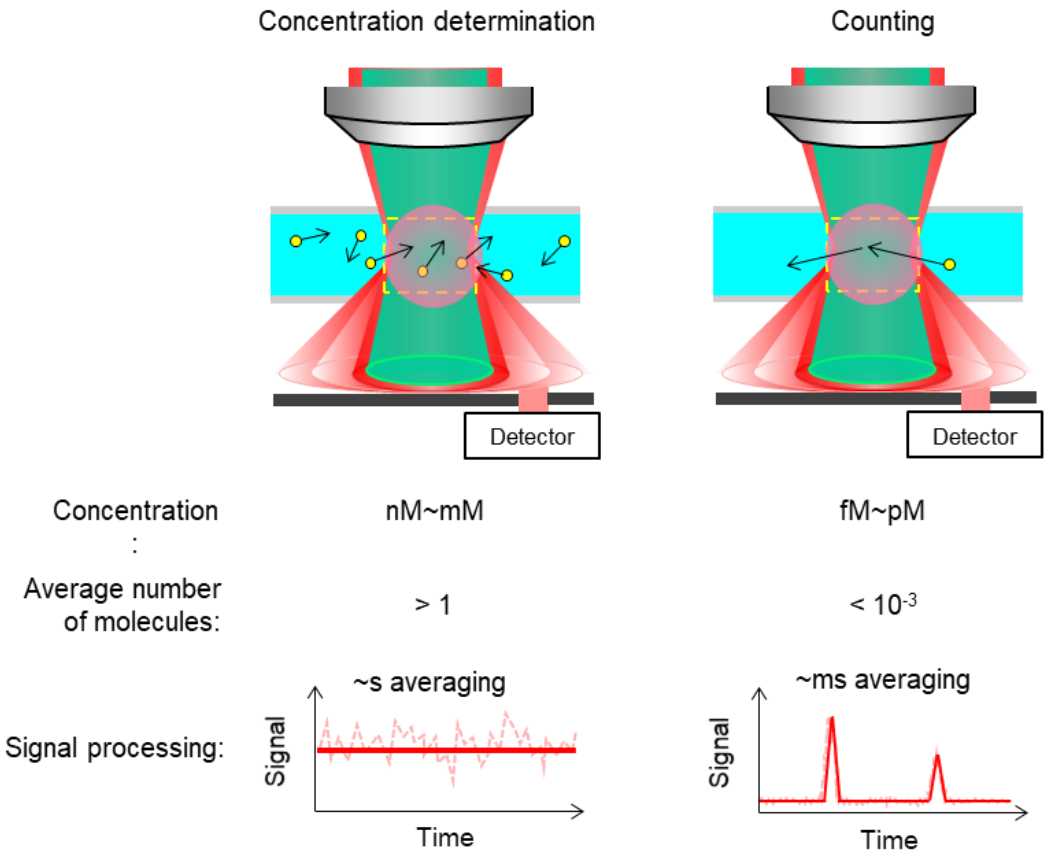


*Figure 4-2. Difference between concentration determination mode (Chapter 3) and counting mode (Chapter 4).*

### 4.2.2 Demonstration of Nanoparticle Counting

For verification of nanoparticle detection by the counting-mode POD, the photothermal signals from nanoparticles in a nanochannel were measured. An aqueous solution of Au nanoparticles with 20 nm in diameter (BBI Solutions, Crumlin, UK) was introduced to nanochannels with 800 nm wide and 700 nm deep. Figure 4-3 shows a typical time trace of the signal detected by the counting-mode POD. Clear pulse signals were observed above the background signal. The concentration of the solution was $3.6 \times 10^{10}$ particles/mL, and the expectation value of the number of molecules in the detection volume was $3.4 \times 10^{-2}$, much smaller than 1. Thus, each pulse signal describes an individual nanoparticle passing through the detection region. Furthermore, no pulse signals were observed without the excitation beam; observed signals were derived from the photothermal effect of nanoparticles.

As a follow-up experiment, the relationship between pulse signal and optical

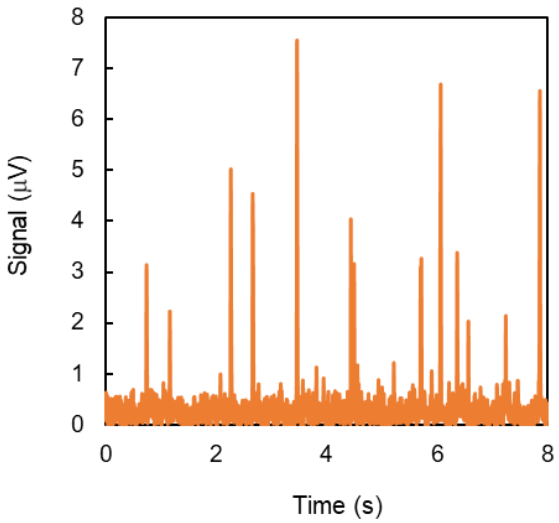


*Figure 4-3. Typical time trace of the signals for 20-nm Au nanoparticle aqueous solution.*

diffraction was investigated. If the signal generation is based on other detection principles such as photothermal heterodyne detection or thermal lens detection,[13,14] signals can be detected at the center of the probe beam spot. For POD, however, this position is not suitable because the diffraction effect is almost negligible. As a result, no pulse signals were observed at this configuration when the detection position of the slit was set at the center of the probe beam spot. Therefore, the observed pulse signals depend on the optical diffraction; the signal generation mechanism is different from other photothermal detection methods. From these results, the detection principle of the counting-mode POD was verified for the first time.

### 4.3 Optimization and Performance Evaluation

#### 4.3.1 Optimization of Experimental Condition

In the previous section, the detection principle of the POD was verified, and nanoparticle detection in $10^2$ nm channels was demonstrated. In this section, the experimental condition of the counting-mode POD was optimized for sensitive nanoparticle detection and accurate characterization. First, the intensity of the excitation beam was optimized. Figure 4-4 shows the relationship between excitation beam intensity and the average height of pulse signals. To count pulse signals, a signal was defined as a pulse signal higher than the background signal +5–10$\sigma$ with a duration time of more than 5–15 ms. These values were determined based on the background fluctuation for each measurement. Symbol $\sigma$ represents a standard deviation of a background signal. Data analyses were done by Excel and a home-made Python program. The average pulse signal was linearly increased for excitation beam intensity, which is consistent with the detection

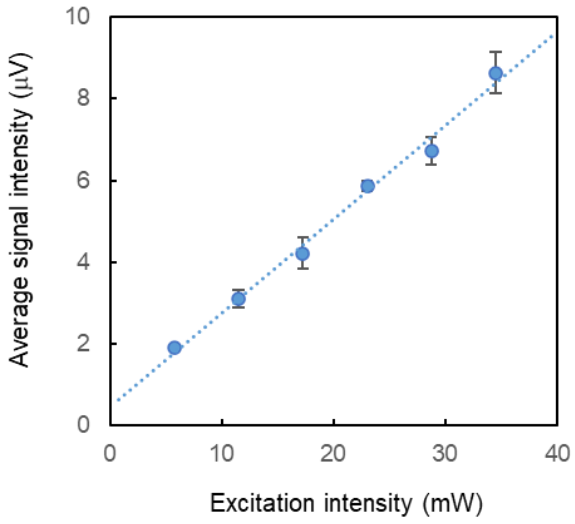


*Figure 4-4. Average peak signal intensity for different excitation beam intensity. Reproduced with permission. (P148, [4]) Copyright 2020, American Chemical Society.*

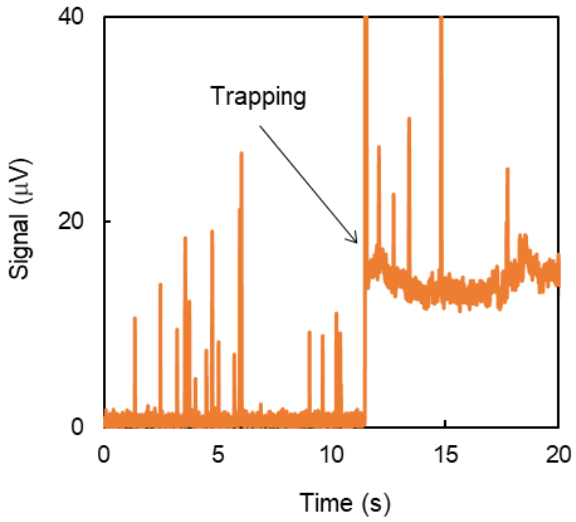


*Figure 4-5. Typical optical trapping effect for 20-nm Au nanoparticle aqueous solutions with the excitation beam intensity of 50 mW.*

principle. However, nanoparticle trapping and adsorption due to optical force were observed for high excitation beam intensity as shown in Fig. 4-5. Therefore, an excitation beam intensity needs to be adjusted for different experimental conditions and target nanoparticles. For 20-nm Au nanoparticles, the excitation beam intensity was adjusted to 20–30 mW in this study.

Next, a flow rate was optimized based on the number of counted nanoparticles and the average pulse signal intensity. Generally, a higher flow rate leads to many counts per unit time: high-throughput analysis of nanoparticles. However, it also leads to a low signal due to the short transit time of the detection area. Experimental results are shown in Fig 4-6. As expected, average signal intensity decreased, and the number of counted nanoparticles increased as the flow rate increased. Considering these two factors, the optimum flow rate was set to 0.17 mm/s.

Furthermore, the time constant (TC) and the modulation frequency of the lock-in amplifier was optimized. Figure 4-7 (a) shows the signal/noise ratio and the number of

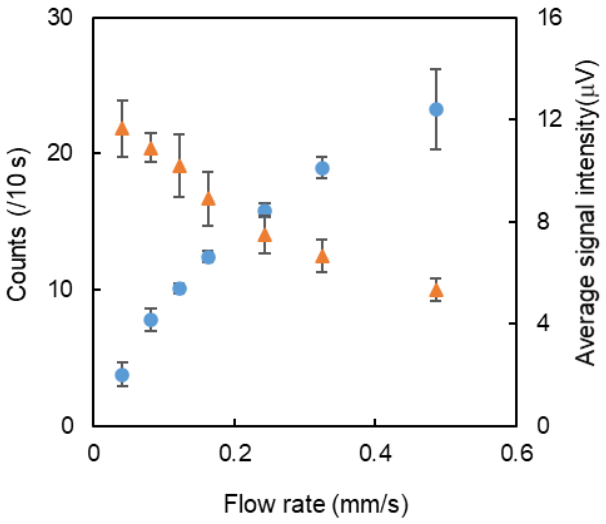


*Figure 4-6. Effect of flow rate on nanoparticle detection. Blue circles represent the number of counts per 10 s. Orange triangles represent the average peak signal intensity. Reproduced with permission. (P148, [4]) Copyright 2020, American Chemical Society.*

counted nanoparticles for different TC. Although short TC is necessary for nanoparticle counting because individual nanoparticles pass through the detection region within a few milliseconds, it also leads to a low signal/noise ratio: counting loss and false counting. Therefore, the optimized TC was set to 2 ms in this study which gives a high signal to noise ratio and a relatively large number of counts. As mentioned in chapter 3, higher modulation frequency leads to shorter laser irradiation time: signal intensity decrease. In contrast, lower modulation frequency leads to low signal selectivity: noise increase. Figure 4-7 (b) shows the signal to noise ratio for different modulation frequencies. The tendency was almost the same as in the case of concentration determination. Therefore, the optimum modulation frequency was set to 1.1 kHz.

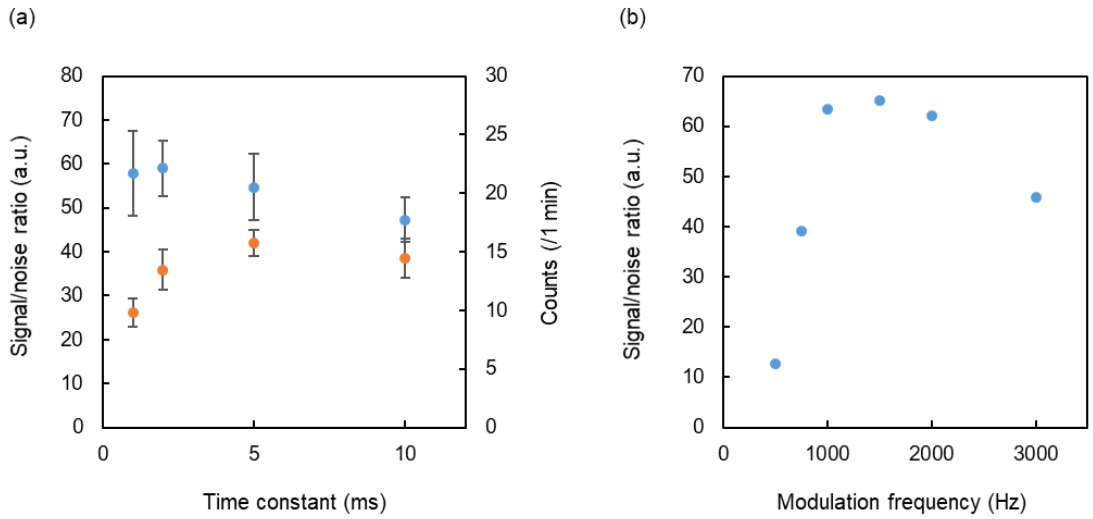


*Figure 4-7. (a) The number of counts and signal/noise ratio versus time constant. Blue circles represent the number of counts per 1 min. Orange circles represent the signal/noise ratio. (b) Signal/noise ratio versus modulation frequency.*

### 4.3.2 Evaluation of Counting Efficiency

To evaluate the detection performance of the counting-mode POD at the optimized experimental condition, concentration determination of Au nanoparticle solutions by pulse counting was demonstrated. If the concentration is low enough to avoid entering two or more nanoparticles in the detection volume at the same time, the number of pulse signals per unit time is proportional to the concentration, injected number of nanoparticles. Figure 4-8 shows the typical time trace of the signal for 20-nm Au nanoparticle solutions with different concentrations. The number of pulse signals increased for high concentration. The calibration curve is shown in Fig. 4-9. The unit time was set to 10 sec, and the total measurement time was 5 min for each concentration. The number of counts linearly increased for the concentration; concentration determination of nanoparticle solutions was successfully performed by the counting-mo0de POD. In this study, the

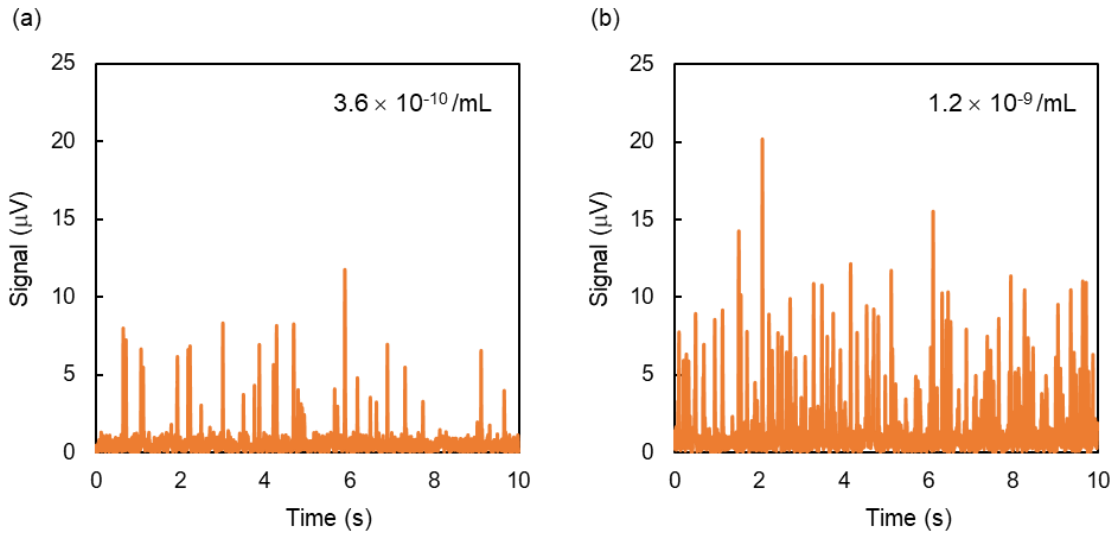


*Figure 4-8. Typical time trace of the signal for 20-nm Au nanoparticle solutions with different concentrations.(a) 3.6 × $10^{-10}$ particles/mL. (b) 1.2 × $10^{-9}$ particles/mL.*

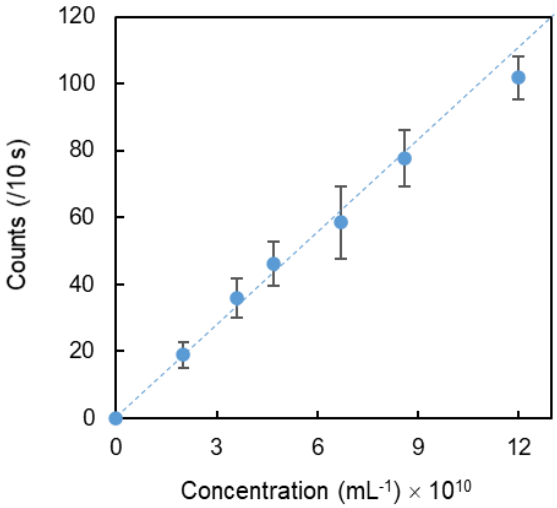


*Figure 4-9. Calibration curve for 20 nm Au nanoparticle aqueous solution. Partially reproduced with permission. (P148, [4]) Copyright 2020, American Chemical Society.*

measured concentration range was in the order of $10^{10}$ particles/mL. Since the detection volume of the counting-mode POD was aL–fL scale, individual nanoparticle detection can be realized in such high concentration samples. However, it also means that a long measurement time is necessary for dilute samples. The maximum throughput of nanoparticle detection in this experiment was ~600 particles/min. Although the throughput is higher than other detection methods requiring surface immobilization of nanoparticles such as SEM or TEM, it is lower than that realized by flow cytometry.[15,16] The dotted line in Fig. 4-9 shows the calculated total number of nanoparticles introduced into the channel which was estimated from the concentration, flow rate, and cross-section area of the nanochannel. Almost 100% detection efficiency was realized for each concentration. As mentioned above, the counting-mode POD enabled almost all nanoparticles flowing in the nanochannel, leading to high detection efficiency.

As a follow-up experiment, the time interval of measured pulse signals was

investigated. Each detection event occurs continuously and independently at a constant average rate; the time interval of pulse counts should obey exponential distribution. Figure 4-10 shows the distribution of the time interval of pulse signals. For comparison, theoretical exponential distribution was plotted which was calculated from the concentration, flow rate, and channel size. The experimental result was well consistent with theoretical exponential distribution. This result means little or no duplicate counting caused by Brownian motion of nanoparticles or optical trapping. Thus, the counting-mode POD can accurately detect individual nanoparticles flowing in the nanochannel. These results show that calibration-less concentration determination can be realized by dividing the number of pulse signals by the sample volume introduced into the nanochannel.

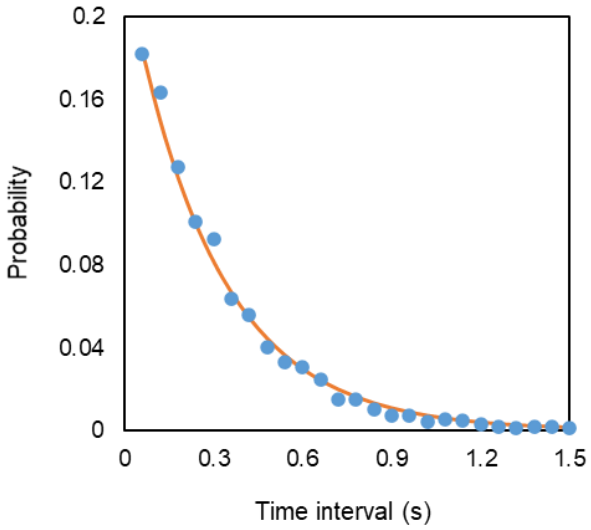


*Figure 4-10. Distribution of the time interval of pulse signals. Blue dots represent experimental results. The orange line represents exponential distribution.*

### 4.3.3 Size Measurement of Nanoparticles

As mentioned above, all nanoparticles flowing in nanochannels experience almost the same excitation beam intensity. Therefore, the obtained pulse signal by the counting-mode POD has information about the absorbance of the nanoparticle; the counting-mode POD enables size measurement of individual nanoparticles by their absorbance. Figure 4-11 shows the intensity distribution of 5000 peak signals from a 20 nm Au nanoparticle aqueous solution. Note that the bin width of the histogram was set based on the logarithm of signal intensity. According to Mie theory, the absorption cross-section of nanoparticles is almost proportional to their volume; the photothermal signal is proportional to the cube of the particle diameter.[17] The histogram showed unimodal distribution, with the coefficient variation (CV) of 13.8% around the average signal. The CV is a little larger than those reported by the manufacturer (<8%). This might be due to the spatial variation in laser intensity in the channel which is estimated to be ~12%. The CV calculated from

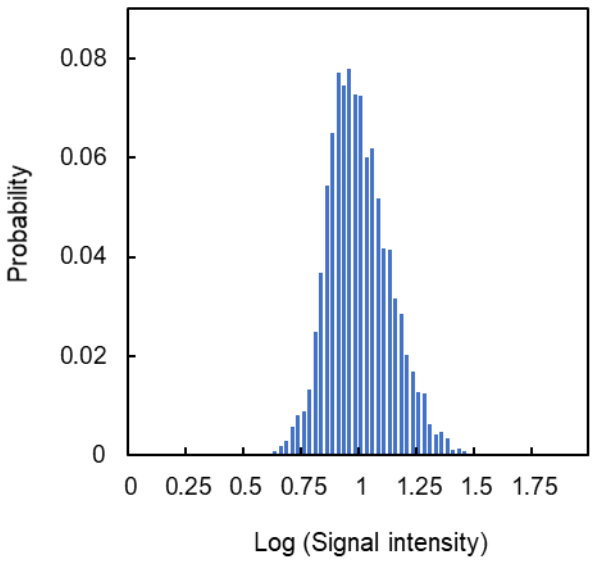


*Figure 4-11. Histogram of the signal intensity for 20-nm Au nanoparticles.*

error propagation theory is <14.6%, almost the same as the experimental results. However, the above estimation does not consider the effect of flow velocity distribution in the nanochannel and the Brownian motion of nanoparticles. Further investigation is needed to improve the performance of size measurement of individual nanoparticles.

Next, the counting-mode POD was applied to nanoparticles of different sizes. Figure 4-12 shows the typical time trace of the signal for an aqueous solution of Au nanoparticles with 10 nm in diameter (BBI Solutions, Crumlin, UK). Since the photothermal signal is proportional to the cube of the particle diameter, the excitation beam intensity was set to 50 mW. Clear pulse signals were observed above the background signal with an average signal/noise ratio of 6.3. This result shows sub-10 nm nanoparticle detection can be realized by the counting-mode POD with high excitation beam intensity. To clarify the relationship between particle size and signal intensity, the

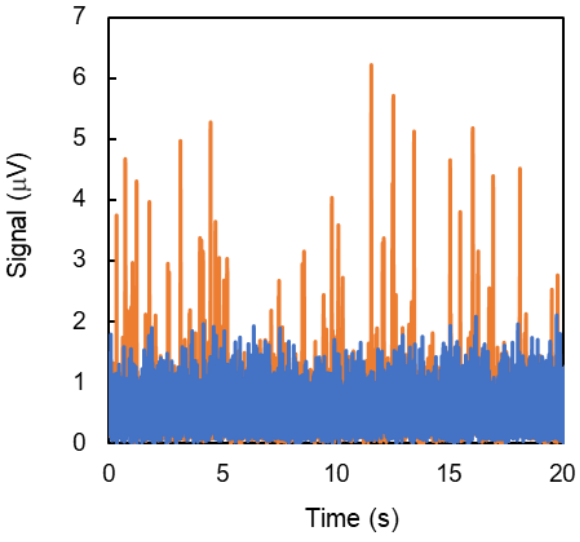


*Figure 4-12. Typical time trace of the signal for 10-nm Au nanoparticle solutions. Orange lines represent the signal with excitation. Blue lines represent the signal without excitation.*

intensity distributions for 10, 20, and 40-nm Au nanoparticles were investigated. As mentioned above, nanoparticle trapping and adsorption due to optical force were observed for large nanoparticles. Therefore, the excitation intensity was optimized for each particle size, and pulse signal intensity was compensated based on the excitation intensity. Experimental results are shown in Fig. 4-13 (a). A histogram with unimodal distribution was obtained for each particle size. Figure 4-13 (b) shows the logarithmic plot of the median signal intensity versus particle size. The slope of the plot was 3.4, which is consistent with the theory in which the photothermal signal is proportional to the cube of the particle diameter. Then, the particle diameter and deviation were calculated based on the signal intensity for 20-nm Au nanoparticles. The calculated particle diameter and deviation was 9.1 ± 5.8 nm for 10-nm Au nanoparticles and 44.8 ±3.0 nm for 40-nm Au nanoparticles. These results show that the counting-mode POD can be applied to the size measurement of individual nanoparticles from the absorbance. Although several papers

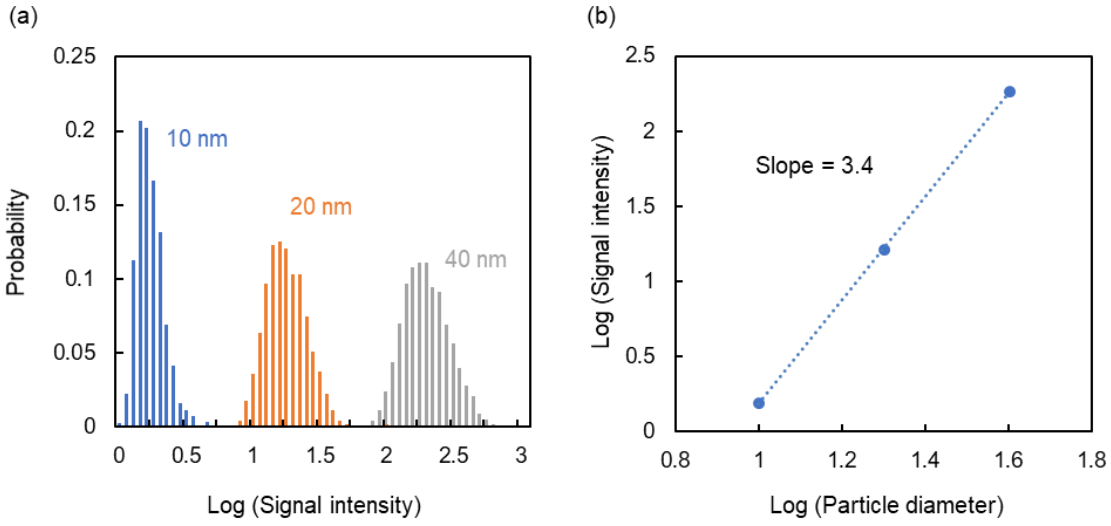


*Figure 4-13. (a) Histogram of the signal intensity for 10, 20, and 40-nm Au nanoparticles. (b) Logarithmic plot of the median signal intensity versus particle size.*

report the measurement of scattering efficiency of individual nanoparticles in a fluid, to the best of the author's knowledge, this is the first report of the measurement of absorption efficiency of individual nanoparticles in a fluid.

Finally, the counting-mode POD was applied to a mixture of nanoparticles of different sizes. Figure 4-14 shows the particle size distribution for a mixture of 20 and 40-nm Au nanoparticles. To avoid optical force trapping, the excitation intensity was set to 20 mW. Two particle sizes were resolved from the signal intensity. Thus, the counting mode POD can be applied to mixed samples and classify nanoparticles with different sizes.

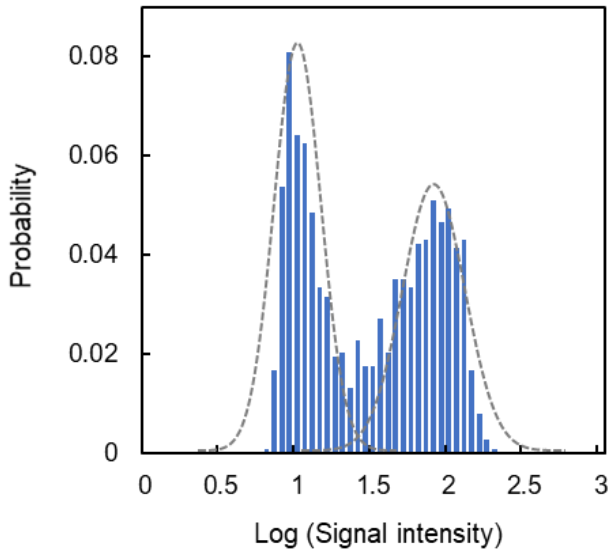


*Figure 4-14. Signal intensity distribution for a mixture of 20 and 40-nm Au nanoparticles.*

## 4.4 Summary

In this chapter, nanoparticle detection and characterization by the counting-mode POD was realized for the first time. The detection principle of the counting-mode POD was verified, and experimental conditions were optimized. Concentration determination of Au nanoparticle solutions by pulse counting was demonstrated, and almost 100% detection efficiency, calibration-less concentration determination was realized. Furthermore, the size of individual nanoparticles was evaluated based on the absorbance. Finally, 20 and 40-nm Au nanoparticles were classified based on the pulse signal intensity.

The important feature of counting-mode POD is label-free and real-time detection of individual nanoparticles in a fluid. These features enable online detection of synthesized nanoparticles such as drug-delivery carriers on micro-/nanofluidic devices. Furthermore, combining fluidic control systems such as pumps and valves will enable the sorting of individual nanoparticles based on the information obtained by the counting-mode POD. By introducing a UV laser as an excitation beam, biological samples such as viruses and exosomes can be detected, which will be useful for diagnoses. Thus, the counting-mode POD has the potential for a wide range of chemical/biological applications.

## 4.5 References of Chapter 4


1. Veiseh, O., Gunn, J. W. & Zhang, M. Design and fabrication of magnetic nanoparticles for targeted drug delivery and imaging. *Adv. Drug Deliv. Rev.* **62**, 284–304 (2010).
2. Moghimi, S. M., Hunter, A. C. & Murray, J. C. Nanomedicine: Current status and future prospects. *FASEB J.* **19**, 311–330 (2005).
3. Huang, X., El-Sayed, I. H., Qian, W. & El-Sayed, M. A. Cancer cell imaging and photothermal therapy in the near-infrared region by using gold nanorods. *J. Am. Chem. Soc.* **128**, 2115–2120 (2006).
4. Smith, A. M. & Nie, S. Semiconductor nanocrystals: Structure, properties, and band gap engineering. *Acc. Chem. Res.* **43**, 190–200 (2010).
5. Elazzouzi-Hafraoui, S. *et al.* The shape and size distribution of crystalline nanoparticles prepared by acid hydrolysis of native cellulose. *Biomacromolecules* **9**, 57–65 (2008).
6. Mitra, A., Deutsch, B., Ignatovich, F., Dykes, C. & Novotny, L. Nano-optofluidic detection of single viruses and nanoparticles. *ACS Nano* **4**, 1305–1312 (2010).
7. Liang, L., Zuo, Y. F., Wu, W., Zhu, X. Q. & Yang, Y. Optofluidic restricted imaging, spectroscopy and counting of nanoparticles by evanescent wave using immiscible liquids. *Lab Chip* **16**, 3007–3014 (2016).
8. Filipe, V., Hawe, A. & Jiskoot, W. Critical evaluation of nanoparticle tracking analysis (NTA) by NanoSight for the measurement of nanoparticles and protein aggregates. *Pharm. Res.* **27**, 796–810 (2010).
9. German, S. R., Hurd, T. S., White, H. S. & Mega, T. L. Sizing Individual Au Nanoparticles in Solution with Sub-Nanometer Resolution. *ACS Nano* **9**, 7186–7194 (2015).
10. Terejánszky, P., Makra, I., Fürjes, P. & Gyurcsányi, R. E. Calibration-less sizing and quantitation of polymeric nanoparticles and viruses with quartz nanopipets. *Anal. Chem.* **86**, 4688–4697 (2014).
11. Shimizu, H., Mawatari, K. & Kitamori, T. Development of a differential interference contrast thermal lens microscope for sensitive individual nanoparticle detection in liquid. *Anal. Chem.* **81**, 9802–9806 (2009).
12. Maceiczyk, R., Shimizu, H., Müller, D., Kitamori, T. & DeMello, A. A Photothermal Spectrometer for Fast and Background-Free Detection of Individual Nanoparticles in Flow. *Anal. Chem.* **89**, 1994–1999 (2017).

13. Berciaud, S., Lasne, D., Blab, G. A., Cognet, L. & Lounis, B. Photothermal heterodyne imaging of individual metallic nanoparticles: Theory versus experiment. *Phys. Rev. B - Condens. Matter Mater. Phys.* **73**, 1–8 (2006).
14. Mawatari, K., Kitamori, T. & Sawada, T. Individual detection of single-nanometer-sized particles in liquid by photothermal microscope. *Anal. Chem.* **70**, 5037–5041 (1998).
15. Yang, L., Zhu, S., Hang, W., Wu, L. & Yan, X. Development of an ultrasensitive dual-channel flow cytometer for the individual analysis of nanosized particles and biomolecules. *Anal. Chem.* **81**, 2555–2563 (2009).
16. Chen, C. *et al.* Multiparameter Quantification of Liposomal Nanomedicines at the Single-Particle Level by High-Sensitivity Flow Cytometry. *ACS Appl. Mater. Interfaces* **9**, 13913–13919 (2017).
17. van de Hulst, H. C. *Light scattering by small particles*. (Courier Corporation, 1981).

# Chapter 5. Application to Nanofluidic Analytical Device

## 5.1 Introduction

Integration of sequential analytical processes into microfluidic devices enables complex chemical/biological analyses at an ultra-small scale, which is a long-standing concept of miniaturized total analysis system (μ-TAS).[1] Several integrated microfluidic devices have been realized for metal ion analysis, single-cell analysis, and medical diagnostics.[2-4] Furthermore, methodologies of integration have been expanded into nanofluidics by T. Kitamori's group, and integrated nanofluidic devices have been developed. Their integration methodology is known as the micro-unit operation (MUO) and nano-unit operation (NUO). In this methodology, bulk scale analytical processes are broken down into multiple unit operations, converted into MUO and NUO, and integrated into the device by connecting these unit operations in series. These unit operations are roughly divided into three processes: sampling, chemical processing, and detection. For sampling, pressure-driven pinched injection, femtoliter volumetric pipette, and single-cell sampling interface has been developed.[5-7] For chemical processing, picoliter enzyme reactor and immunochemical reaction have been realized in $10^2$ nm channels.[8,9] For detection, differential interference contrast thermal lens microscope (DIC-TLM) has been used for sub-micron channels as a highly sensitive yet versatile detector.[10] By the integration of these unit operations, separation analysis, enzyme-linked immunosorbent assay, and single-cell analysis has been realized in $10^2$ nm space.[11-13] However, integration of sequential analytical processes into $10^1$ nm space is still challenging, despite $10^1$ nm fluidic devices have the potential to provide a novel platform that enables chemical/biological analyses at a single molecule/nanoparticle level. This is due to the lack of highly sensitive yet versatile detection methodology for such ultra-small space.

In the previous chapters, a novel detection methodology for $10^1$–$10^2$ nm channels:

photothermal optical diffraction (POD) was developed, and label-free molecule and nanoparticle detection was realized. The high detection performance of the POD for nanochannels is promising for the realization of analytical devices utilizing ultra-small space.

In this chapter, the proof-of-concept for $10^1$ nm fluidic devices is demonstrated by the POD. First, the POD is used as a detector for chemical/biological analyses in $10^2$ nm channels to show its applicability to nanofluidic analytical devices. Enzyme-linked immunosorbent assay and normal-phase chromatography are demonstrated, and the analytical performance is evaluated. Then, separation analysis in $10^1$ nm channels is demonstrated by the integration of sequential analytical processes: pressure-driven pinched injection, normal-phase chromatography, and label-free detection by the POD.

## 5.2 Enzyme-linked Immunosorbent Assay in $10^2$ nm Channel

### 5.2.1 Experimental

*Enzyme-linked Immunosorbent Assay (ELISA)*

Immunoassay is one of the most general chemical processing for biological samples because high biological affinity between antibody and antigen provides extremely high selectivity. Currently, enzyme-linked immunosorbent assay (ELISA) is most widely used because it provides high sensitivity and a low limit of detection. A principle of ELISA is shown in Fig.5-1. First, antigen in a sample solution is captured by antibody immobilized on a solid surface, and antigen-antibody immunocomplex is generated. Then, another enzyme-labeled antibody is introduced, and the antigen is sandwiched by two antibodies. After that, an enzymatic reaction is performed, and colored substrates are generated. Finally, colored substrates are quantified by a detector

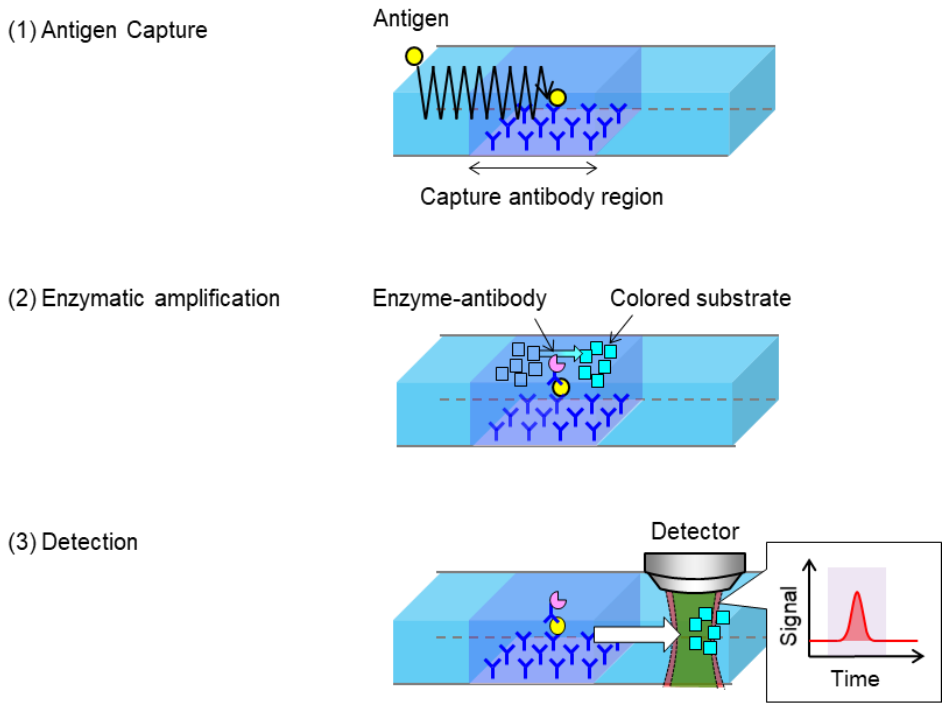


*Figure 5-1. Principle of enzyme-linked immunosorbent assay (ELISA).*

such as an absorptiometer. The obtained signal is proportional to the number of captured antigens. This procedure enables highly selective yet sensitive biomolecule detection.

Miniaturization of ELISA into micro/nanofluidic device has great advantages: short analysis time, reducing the consumption of samples, and sensitivity improvement by confining colored substrates in small spaces. Furthermore, immunoreaction in ultra-small space enables single or countable molecule analysis. K. Shirai et.al realized highly efficient (near 100%) immunochemical reaction in 3.3 μm wide and 200 nm deep channels, and single-molecule ELISA in 2 μm wide and 800 nm deep channels was demonstrated by using the DIC-TLM as a detector.[8,12]

In this section, the above nanofluidic ELISA was implemented by the POD, and standard C-reactive protein solution was quantified in $10^2$ nm wide and deep channels.

*Device Fabrication and Surface Modification*

The fabrication procedure of microchannels and nanochannels was almost the same as that explained in chapter 2. To immobilize capture antibody on the surface of nanochannel, the surface of a substrate in which microchannels were fabricated was modified with aminopropyltriethoxysilane (APTES). By irradiating Vacuum ultra-violet (VUV) light through a chromium photomask, a partially modified APTES layer was formed on the substrate. the APTES pattern and nanochannels were orthogonally aligned when bonding substrates. After bonding, the entire channel surface was modified with silanated polyethylene glycol (PEG) to avoid non-specific protein adsorption. Finally, capture antibodies were chemically immobilized by crosslinking the amino groups of APTES molecules using glutaraldehyde. Residual reactive groups were blocked with

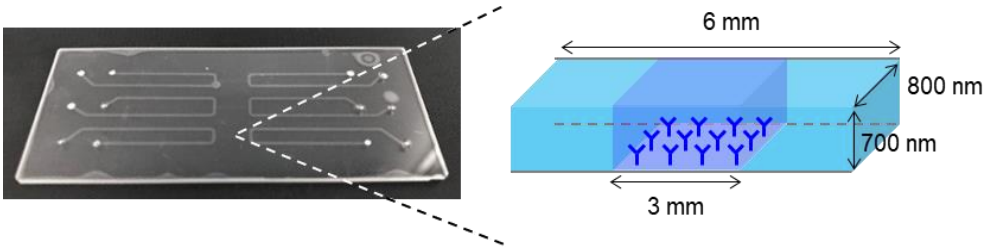


*Figure 5-2. Design and typical image of the fabricated nanofluidic device.*

ethanolamine. Figure 5-2 shows the fabricated nanofluidic device. In this study, the width, depth, and length of each nanochannel were 800 nm, 700 nm, and 6 mm, respectively. The length of the capture antibody region was 3 mm. Three sets of microchannels and nanochannels were fabricated for repeated measurements.

*Protocol of ELISA*

Figure 5-3 shows the experimental setup for ELISA in $10^2$ nm channels. Each operation of ELISA such as immunoreaction, bound/free separation, and enzymatic

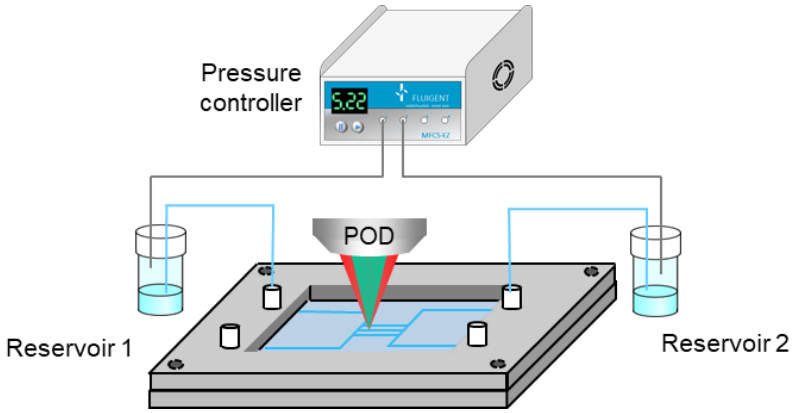


*Figure 5-3. Experimental setup for ELISA.*

reaction was performed and controlled by applying pressure to sample vials connected to microchannels. Table 5-1 shows the protocol of ELISA. First, the entire nanochannel surface was blocked by BSA (bovine serum album) by introducing a 2% BSA/PBS solution with 0.05% Tween-20. The blocking solution was also used as a buffer during the experiment. Next, standard C-reactive protein (CRP) solution was introduced to nanochannels. After 60 seconds of introduction, the CRP solution was washed out by the buffer solution. Then, horseradish peroxidase (HRP) labeled capture antibody solution (5 μg/mL) was introduced for 60 seconds and washed out by buffer solution. Subsequently, microchannels and nanochannels were washed with a buffer solution for bound/free separation. After washing, a non-colored tetramethylbenzidine (TMB) substrate solution was introduced, and the flow was stopped for 60 seconds for the enzymatic reaction. Finally, the flow was re-started, and the colored TMB substrates were detected by the POD at the end of the nanochannel. After finishing the measurement, captured antigens were washed out by glycine-HCl solution (pH 2.2). The above cycle was repeated for multiple measurements in a single device.

*Table 5-1. Protocol of ELISA.*

| | Reservoir 1 | Reservoir 2 |
|---|---|---|
| 1. Blocking (10 min) | Buffer | Buffer |
| 2. Antigen injection | CRP | Buffer |
| 3. Capture antibody injection | HRP-CRP | Buffer |
| 4. Washing (1.5min) | Buffer | Buffer |
| 5. TMB detection (x3~4 cycle) | Xylen Cyanol | TMB |
| 6. Glycine washing (20 min) | Gly-HCl pH 2.2 | Gly-HCl pH 2.2 |

(Buffer : 2% BSA/PBS, 0.05% Tween)

### 5.2.2 Results and Discussion

Before implementing ELISA experiments, the detection performance of the POD for colored TMB solution was evaluated. Colored TMB solution was prepared by enzymatic reaction in bulk and introduced to nanochannels. In previous chapters, a 532 nm solid-state laser was used as an excitation laser. However, TMB solution has a maximum absorbance wavelength around 630–660 nm. Therefore, a 633 nm He−Ne laser was used as an excitation laser, and a 532 nm solid-state laser was used as a probe laser. The intensity of the excitation laser was 4.8 mW, and the intensity of the probe laser was 0.5 mW under the objective lens. The time constant of the lock-in amplifier was set to 100 ms. Figure 5-4 shows a calibration curve for colored TMB solution. The calibration curve showed good linearity with the concentration measured by a conventional absorptiometer. The calculated LOD was 14.6 μM which corresponds to an average of 8,300 molecules in the detection volume of 0.95 fL. The high LOD was due to the low intensity of the excitation beam.

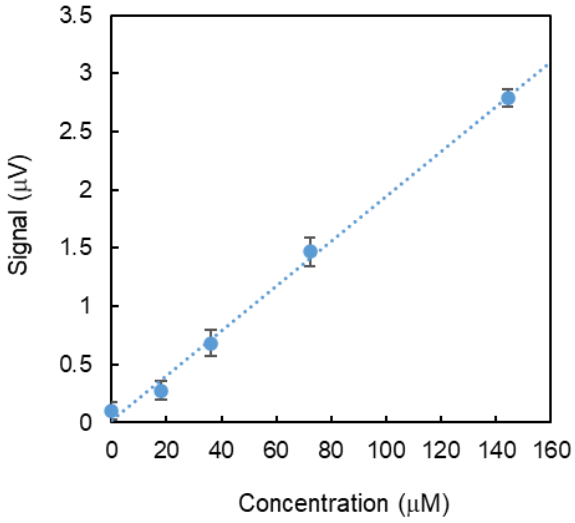


*Figure 5-4. Calibration curve for colored TMB solution.*

To confirm whether the detection performance of the POD is suitable for ELISA, the concentration of colored TMB solution produced by the enzymatic reaction of a single analyte molecule was calculated. The four HRP enzymes on the antibody produce $1.4\times10^6$ molecules of the colored-TMB for the reaction time of 60 seconds assuming the turnover of HRP as 6000 molecules/sec. The produced colored TMB molecules diffuse during the enzymatic reaction. The diffusion length can be calculated from the Einstein-Smoluchowski equation:

$$\sigma = \sqrt{2Dt} \qquad (5-1)$$

where $D$ is the diffusion coefficient. The diffusion coefficient of the TMB was estimated to be $3.6 \times 10^{-10}$ $m^2/s$ from the molecular weight and viscosity, and the calculated diffusion length was 208 μm at $t$ = 60 sec. Since 95% of the colored TMB molecules are within the distance of $2\sigma$, the calculated diffusion volume of colored TMB solution was 470 fL for 800 nm wide and 700 nm deep channels. Thus, the concentration of the colored TMB solution was calculated to be 5.2 μM for a single analyte molecule. Although the value is smaller than the LOD, sensitive concentration determination could be feasible by the POD.

Finally, nanofluidic ELISA was implemented by the POD, and standard CRP solutions were quantified. Figure 5-5 (a) shows the ELISA signal for standard CRP solutions with different concentrations. In this experiment, laser adjustment and introduction of TMB solution were performed in $t$ = 0–120 sec, and enzymatic reaction was performed in $t$ = 120–180 sec. The pink region in the graph shows the estimated peak arriving time which was calculated from flow velocity and length of capture antibody region. Peak signals were observed at this region; ELISA signals were obtained by the

POD. Figure 5-5 (b) shows the calibration curve of average signal intensity at peak arriving time. The average signal intensity linearly increased for concentration. The LOD was calculated from the sensitivity and fluctuation of the signal intensity for the blank solutions. The LOD was 7.0 ng/mL, which corresponds to 140 molecules of CRP introduced to the nanochannel. The high LOD was due to the high background signal and noise by non-specific adsorption. In this experiment, immunoassay conditions are followed by previous experiments conducted by 2 μm wide and 800 nm deep channels. Optimization of immunoassay conditions is necessary for further improvement. Although several conditions remain to be improved, nanofluidic ELISA was successfully demonstrated by the POD.

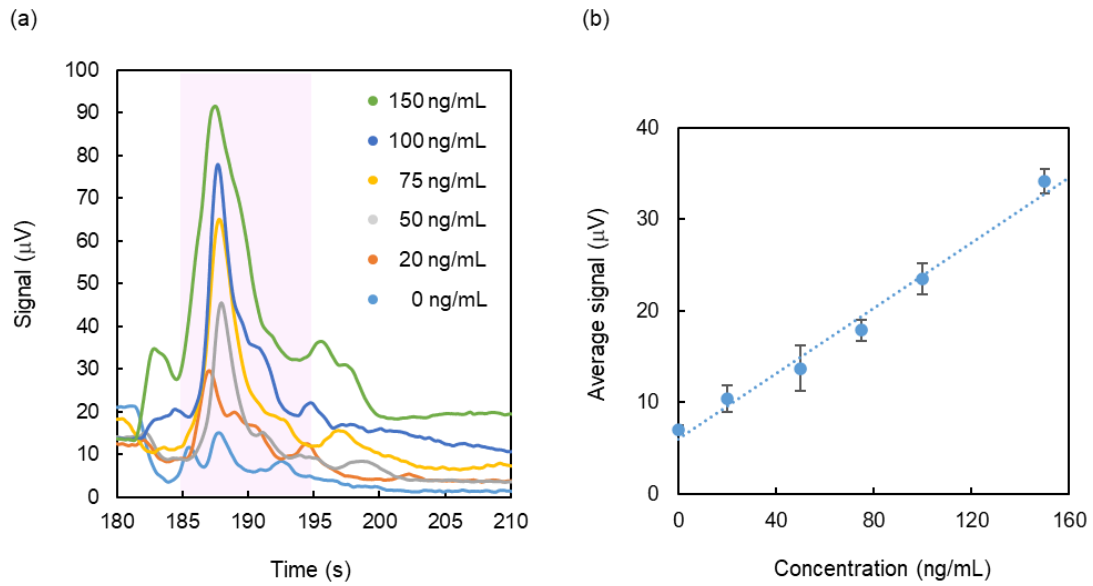


*Figure 5-5. (a) Time trace of signal for ELISA. (b) Calibration curve for standard CRP solution.*

## 5.3 Normal-phase Chromatography in $10^2$ nm Channel

### 5.3.1 Experimental

*Nanochannel Chromatography*

Column miniaturization of liquid chromatography is one of the major trends in the field of separation analysis due to the rising demand for single-cell proteomics and metabolomics which necessitate aL–pL sample analyses with high separation performance.[14,15] Nanochannels has attracted much attention as ultra-small open tubular columns for chromatography. The high surface-to-volume ratio of nanochannels enables efficient molecular-surface interaction, leading to high separation performance. The theoretical plate height ($H$) for rectangular open tubular chromatography is theoretically expressed as follows:[16,17]

$$H = \frac{2D_m}{u} + \frac{f_0}{105} \cdot \frac{d^2}{D_m} \cdot u \qquad (5-2)$$

where $u$ is the flow velocity, $f_0$ is a constant that is determined by the width-to-depth ratio of the separation column, and $d$ is the depth of the column. The first term represents the effect of molecular diffusion through the channel length direction, and the second term represents the effect of mass transfer through the channel depth direction. In nanochannel chromatography, the second term is negligible due to the ultra-small channel depth; high separation performance can be achieved for high flow velocity. Although nanochannel chromatography has been demonstrated by several researchers,[18,19] the problem is molecular detection. Generally, aL–pL chromatography necessitates the online detection of separated samples passing through the detection region within a few seconds without any labeling or chemical amplification. This limitation makes sensitive molecular detection difficult. For example, H. Shimizu et.al realized femtoliter sample separation

and label-free detection in 2.3 μm wide and 350 nm deep channels by DIC-TLM.[20] However, the LOD was in the order of $10^5$ molecules. Thus, a highly sensitive yet label-free detection method is essential for nanochannel chromatography.

In this section, the POD was applied to $10^2$ nm channel chromatography, and femtoliter sample separation and label-free zeptomole detection were demonstrated.

*Experimental Procedure*

In this study, a pressure-driven pinched injection was used for volumetric sampling, which was used in previous experiments.[5,21] The schematic procedure is shown in Fig. 5-6. A cross-shaped nanochannel was used for sample loading and volumetric injection.

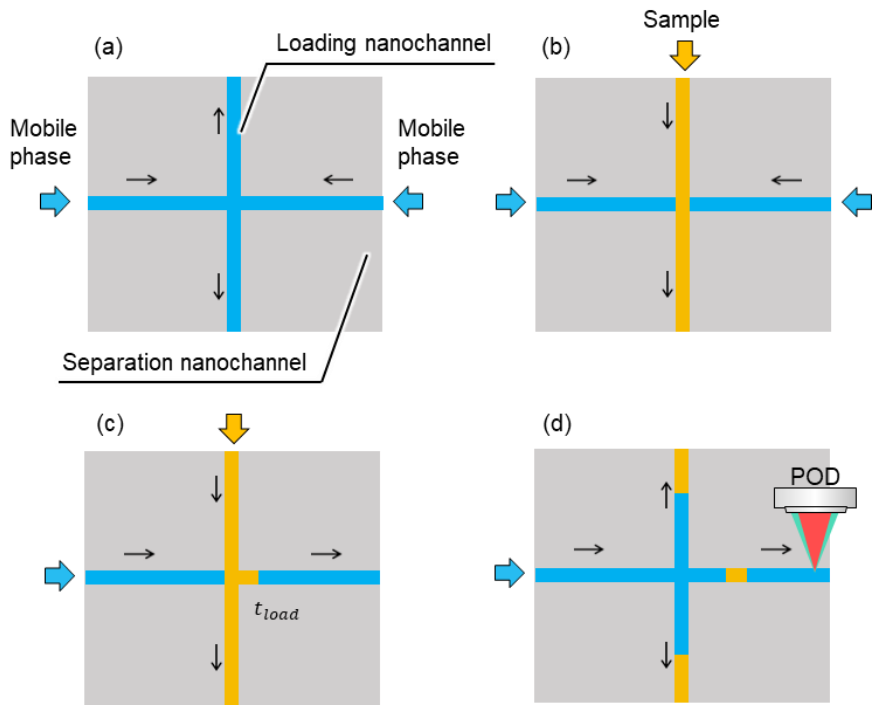


*Figure 5-6. Procedure of volumetric sample injection. (a) Before loading. (b) Sample Introduction to the loading channel. (c) Sample Introduction to separation channel. (d) Volumetric injection to separation channel.*

First, both loading nanochannel and separation nanochannel were filled with a mobile solution. For sample loading from microchannel to loading nanochannel, the pressure was applied from the top of the loading nanochannel and both ends of the separation nanochannel. Then, the pressure of the right side was turned off, and a sample solution was introduced to the separation nanochannel. After a few seconds of loading time, the pressure of the loading nanochannel was turned off, and the sample solution was injected into the separation nanochannel. By controlling the loading time, the introduced sample volume can be controlled at the aL−fL scale.

Figure 5-7 shows the experimental setup and fabricated device for nanochannel chromatography. The width, depth, and length of each nanochannel were 800 nm, 700 nm, and 2 mm, respectively. The POD was aligned at a point 1.0 mm downstream from the cross intersection of the nanochannel; The length of effective separation nanochannel was 1.0 mm. To realize secure fluidic operation, the applied pressures were automatically switched by a script module equipped with the software of the pressure controller.

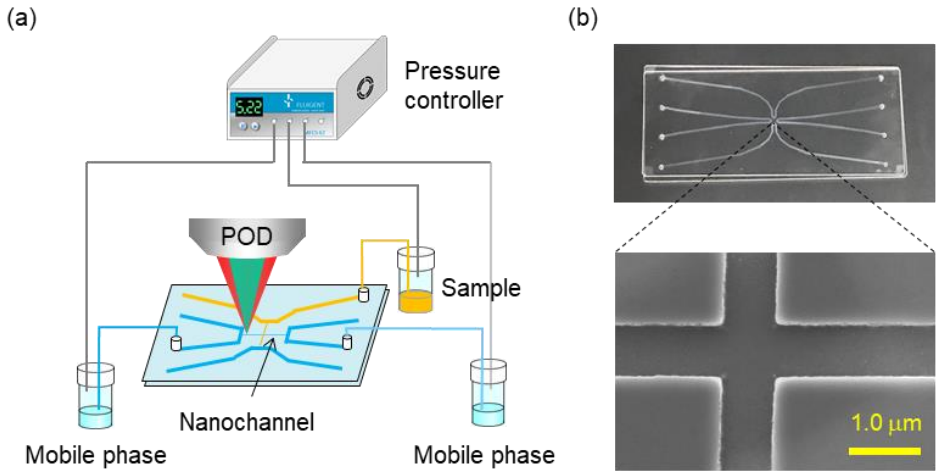


*Figure 5-7. (a) Experimental setup for nanochannel chromatography. (b) Typical images of the fabricated nanofluidic device.*

*Separation Mode and Sample Preparation*

In this study, normal-phase chromatography was demonstrated in which the stationary phase is hydrophilic (polar) and the mobile phase is hydrophobic (nonpolar). The stationary phase was a fused silica surface (silanol and siloxane groups) without any modification, and hexane was used as the mobile phase. Since hexane is an aprotic solvent with a very low dielectric constant, the effect of unique liquid properties in an ultra-small space was negligible. To control the polarity of the mobile phase, 2-propanol was added to hexane. As a test sample for separation, non-fluorescent dyes Sudan IV and Sudan Orange G were used, which chemical formulas were shown in Fig.5-8. Sudan Orange G has two hydroxy groups: more hydrophilic and retained on the silica surface. In contrast, Sudan IV has one hydroxy group: less hydrophilic and barely or not retained on the silica surface.

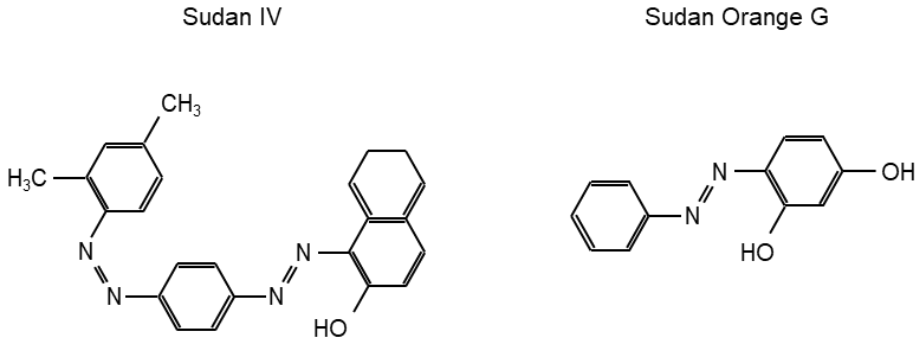


*Figure 5-8. Chemical formula of Sudan IV and Sudan Orange G.*

### 5.3.2 Results and Discussion

*Confirmation of Sample Injection*

First, sample injection by pinched injection system was confirmed. Before loading, the applied pressure for both ends of the separation channel was set to 150 kPa, and the applied pressure for the top of the loading nanochannel was set to 110 kPa. These values were determined to avoid sample solutions entering the separation channel before loading. The loading time of sample introduction was set to 0 sec to minimize the injected sample volume. In this condition, a sample solution in the center of the cross-shaped nanochannel was introduced to the separation nanochannel. Figure 5-9 shows the chromatogram for Sudan IV hexane solution. Clear peak signals were observed for three times measurements. The coefficient of variation (CV) of the three peak times was 1.6%, and the CV of the three peak areas was 1.5%. Thus, sample injection and label-free detection by the POD were successfully realized with high repeatability.

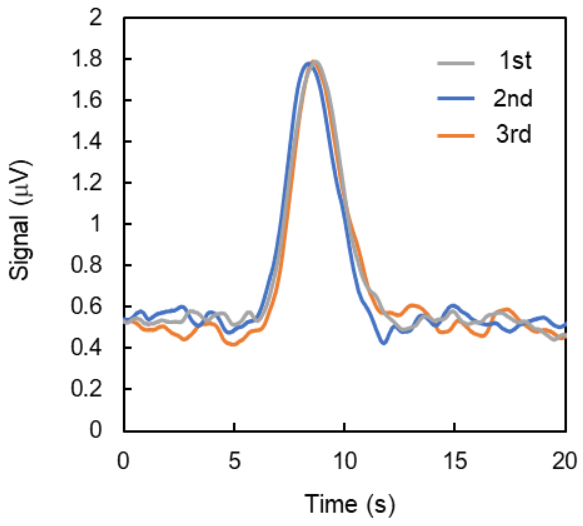


*Figure 5-9. Chromatogram for Sudan IV hexane solution. The experiment was repeated three times.*

*Demonstration of Normal-phase Chromatography*

Next, the separation of non-fluorescent molecules by normal-phase chromatography was demonstrated. Figure 5-10 shows chromatograms for Sudan IV, Sudan Orange G, and a mixture of these two samples. The concentrations of Sudan IV ($\varepsilon$=17700 $M^{-1}cm^{-1}$) and Sudan Orange G ($\varepsilon$=150 $M^{-1}cm^{-1}$) were 50 μM and 1.2 mM, respectively. The time constant of a lock-in amplifier was set to 100 ms. The ratio of 2-propanol in hexane was 0.25%. Two samples were successfully separated and detected by the POD, and peak positions coincided with those of pure samples. These chromatograms also revealed that the separation mode was the normal-phase mode because more hydrophilic Sudan Orange G showed longer retention time than Sudan IV.

Furthermore, the effect of the polarity of the mobile phase was investigated. Figure 5-11 shows the relationship between the chromatograms of mixed samples and ratios of 2-propanol. In this study, 2-propanol enhances the polarity of the mobile phase, leading

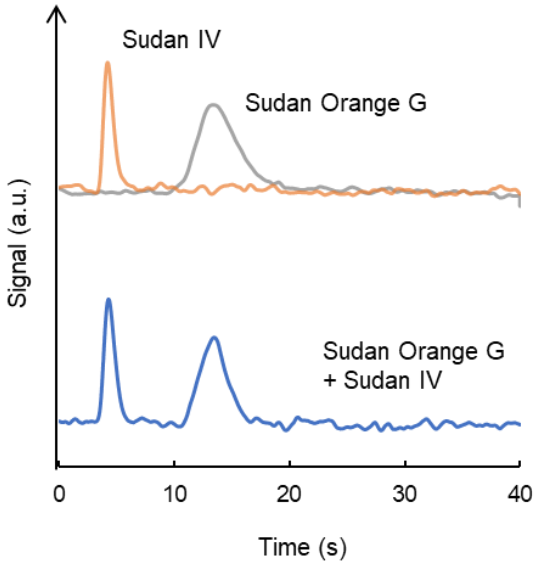


*Figure 5-10. Chromatogram for chromatograms for Sudan IV, Sudan Orange G, and a mixture of these two samples.*

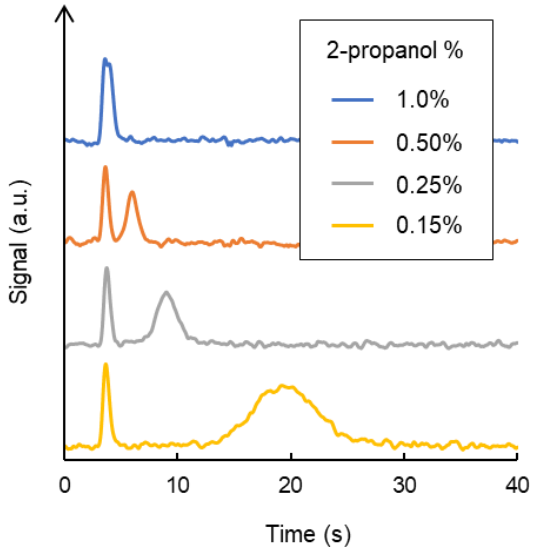


*Figure 5-11. Relationship between the chromatograms of mixed samples and ratios of 2-propanol. Reproduced with permission. (P148, [5]) Copyright 2020, Springer Nature.*

to a short retention time of retained samples. The retention time of Sudan Orange G was shifted from 4.9 s to 19.7 s depending on the ratio of 2-propanol from 0.15% to1.0%, while the retention time of Sudan IV was almost constant. These results mean that Sudan IV is less retained for a fused silica surface, well consistent with the theory of normal-phase chromatography by nanochannels. The appropriate ratio of 2-propanol in hexane was determined to be 0.25–0.50% in this study.

*Optimization of Experimental Condition*

Before evaluating the detection performance of the POD for chromatography, the time constant (TC) of the lock-in amplifier was optimized. Figure 5-12 shows chromatograms for different TC. The ratio of 2-propanol was 0.5%. The time constant (TC) of the lock-in amplifier is important for the detection system of chromatography

because the time response for peak signals is closely related to the measured bandwidth and resolution: separation efficiency. The separation efficiency of two peak signals is evaluated by the resolution $R$:

$$R = \frac{t_{R1} - t_{R2}}{\frac{1}{2}(W_1 + W_2)} \qquad (5-3)$$

where $t_R$ is the retention time of each chromatogram, and $W$ is the bandwidth at the detection position. Although the value of $R$ decreased from 2.1 to 0.5 depending on the TC, the base-line noise decreased for large TC. Thus, TC should be determined from both separation performance and detection performance.

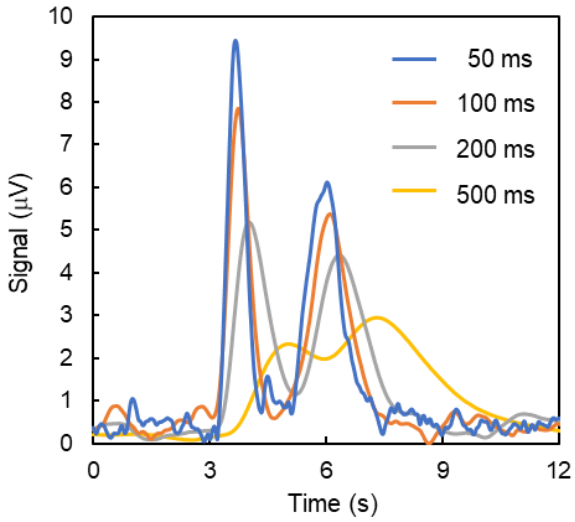


*Figure 5-12. Relationship between the chromatograms of mixed samples and ratios of 2-propanol. Reproduced with permission. (P148, [1]) Copyright 2020, Springer Nature.*

*Evaluation of Detection Performance*

Figure 5-13 (a) shows the chromatogram of Sudan IV solution for different concentrations. The TC was set to 200 ms. Each peak position was aligned based on the highest signal intensity for comparison. Figure 5-13 (b) shows the calibration curve of Sudan IV solution based on the peak area of chromatogram. Peak areas are derived by fitting the chromatograms to a Gaussian curve using Origin Pro 6.1J software. The peak area linearly increased for concentration. The limit of detection (LOD) was defined as a concentration that gives a peak area equivalent to blank $+3\sigma$, and $\sigma$ was calculated by multiplying the base-line noise and estimated peak width. The calculated LOD was 3.0 μM.

To estimate the number of detected molecules, the injected sample volume was calculated from the signal intensity. Figure 5-14 shows the calibration curve of Sudan IV in hexane solution (not injected but flowing in the nanochannel). Dividing peak signals

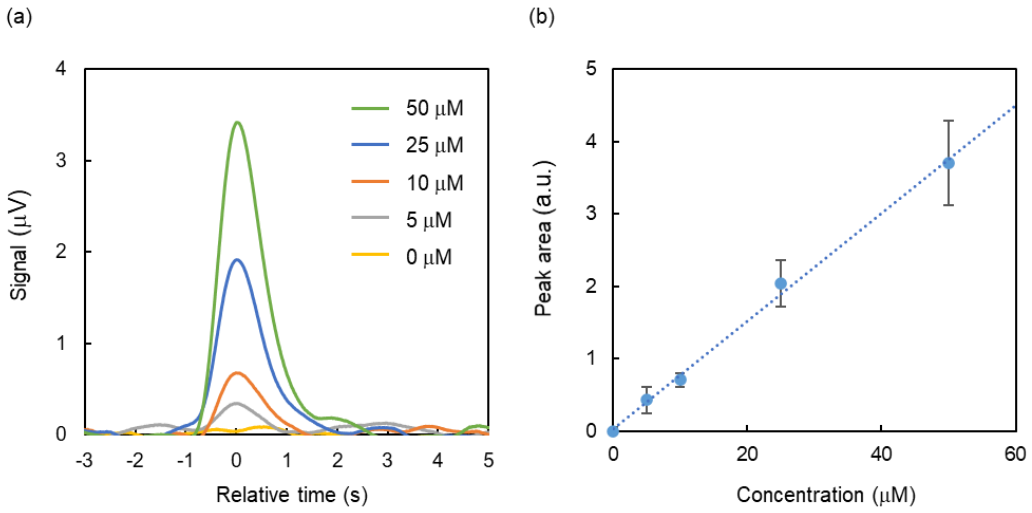


*Figure 5-13. (a) Chromatogram of Sudan IV solution for different concentrations. (b) Calibration curve of Sudan IV solution based on the peak area of chromatogram.*

by signals for solutions flowing in the nanochannel corresponds to time width of the injected sample, which can be converted to sample length by multiplying flow velocity. Then, the injected sample volume is calculated by the calculated sample length and the cross-section area of the nanochannel. By the above procedure, the Injected sample volume was calculated as 1.8±0.1 fL. This value was much larger than the volume of the nanochannel cross intersection (~0.2 fL). This might be due to the molecular diffusion before injection and residual pressure after pressure switching. The calculated LOD corresponds to 5.4 zmol (3300 molecules), approximately 50 times lower than the DIC-TLM applied to the channel with 2.2 μm width and 350 nm depth. Thus, the POD realized highly sensitive label-free molecule detection for nanochannel chromatography.

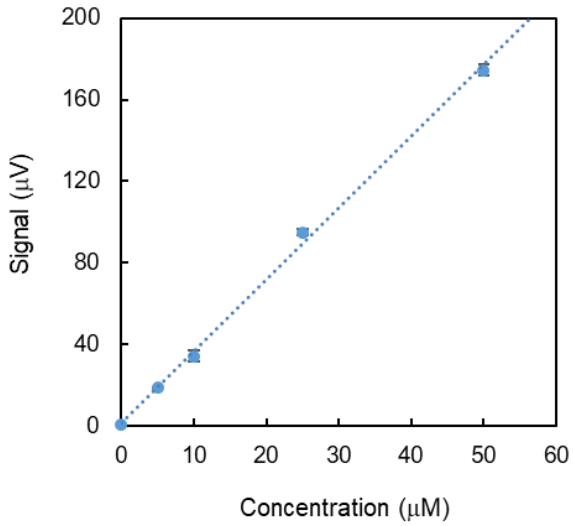


*Figure 5-14. Calibration curve of Sudan IV in hexane solution (not injected but flowing in the nanochannel).*

*Evaluation of Separation Performance*

Finally, the separation performance of the $10^2$ nm channel was evaluated from the POD signal. The separation performance of the chromatography was evaluated by the theoretical plate height ($H$), which was calculated as:

$$H = \frac{\sigma_b^2}{L} \qquad (5-4)$$

where $\sigma_b$ is band variance at the detection region and $L$ is the length of the separation nanochannel. Generally, band broadening during chromatographic separation can be extracted by subtracting the contribution of the initial sample length. However, the calculated initial sample length was 7.5 μm, much narrower than the band variance at the detection region. Therefore, the effect of the initial sample length was ignored, and $\sigma_b$ was calculated by fitting the chromatograms to a Gaussian curve. Figure 5-15 shows the Van Deemter plot (plate height versus flow velocity) of the two samples. The TC was set to 200 ms, and the ratio of 2-propanol was set to 0.5%. The flow velocity was determined by the retention time of Sudan IV because it has little or no retention on the fused silica surface. The applied pressure at injection was changed from 75 to 400 kPa, and the flow velocity linearly increased against the applied pressure. The minimum plate height of Sudan IV and Sudan Orange G were 14.3 and 10.0 μm, which correspond to 70,000 and 100,000 plates/m (70 and 100 plates/mm). The separation performance can be further improved by applying high pressure (~MPa) and increasing flow velocity.

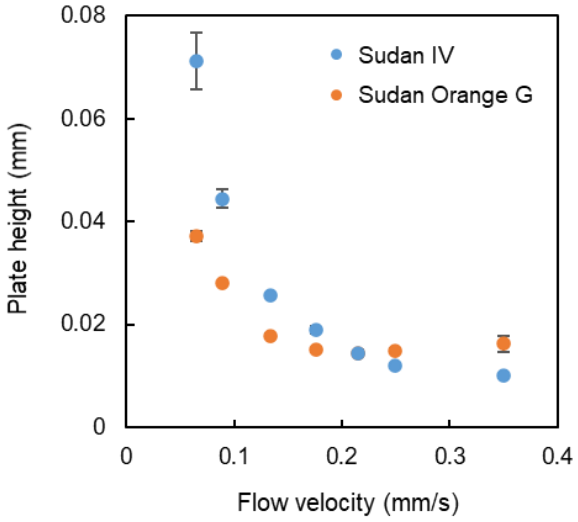


*Figure 5-15. Plate height versus flow velocity (Van Deemter plot) for Sudan IV and Sudan Orange G.*

## 5.4 Demonstration of Sequential Analytical Processes in $10^1$ nm Channel

### 5.4.1 Experimental

*$10^1$ nm Fluidic Device*

Downscaling the analytical space into sub-100 nm ($10^1$ nm) enables chemical/biological analyses at a single molecule/nanoparticle level. To realize such analyses, several nanostructures have been developed: nanopore, carbon nanotube, nanowire, and nanomembrane.[22-24] Although the above nanostructures realized specific recognition and highly sensitive detection of molecules/nanoparticles, only a single function or operation such as detection can be implemented in nanostructures; integration of sequential analytical processes such as sampling, chemical processing, and detection in nanostructures is still difficult. In contrast, micro/nanofluidic devices have been realized multistep chemical/biological analyses in micro/nanochannels by precisely designed fluidic circuits and the integration of multiple functions.[3,13] However, the scale of integration is still in the order of $10^2$–$10^3$ nm, and integration of multiple functions into $10^1$ nm channels has not been realized, despite the advantage of nanochannels for nanopores or nanomembranes. This is due to the difficulty in each fundamental analytical operation such as sampling, chemical processing, and molecule detection in $10^1$ nm channels.

In previous chapters and sections, the POD realized sensitive concentration determination in $10^1$ nm channels and chemical/biological analyses in $10^2$ nm channels. In this final section, $10^1$ nm fluidic separation analysis was demonstrated for the first time by the integration of pressure-driven pinched injection, chromatographic separation, and label-free molecule detection by the POD.

*Experimental Procedure*

To realize separation analysis in $10^1$ nm space, three nano-unit operations (NUO) were connected and implemented in $10^1$ nm channels: volumetric sampling, chromatographic separation, and label-free detection. The schematic design is shown in Fig. 5-16. For volumetric sampling, a pressure-driven pinched injection was applied to $10^1$ nm channels. For chromatographic separation, normal-phase chromatography was performed in $10^1$ nm channels. These operations and conditions were the same as those for $10^2$ nm channels demonstrated in section 5.3. For label-free detection, the POD was applied to $10^1$ nm channels with a time constant of 500 ms.

In this study, the width, depth, and length of nanochannels were 800 nm, 90 nm, and 1 mm, respectively. To avoid the clogging of such shallow channels, five separation nanochannels were fabricated with a gap of 30 μm. The pressure-driven pinched injection was performed in the same procedure as shown in Fig. 5-6. The applied pressure for each channel was 220 kPa at loading. The POD was aligned at a point 0.5 mm downstream from the cross intersection of the nanochannel; The length of effective separation nanochannel was 0.5 mm.

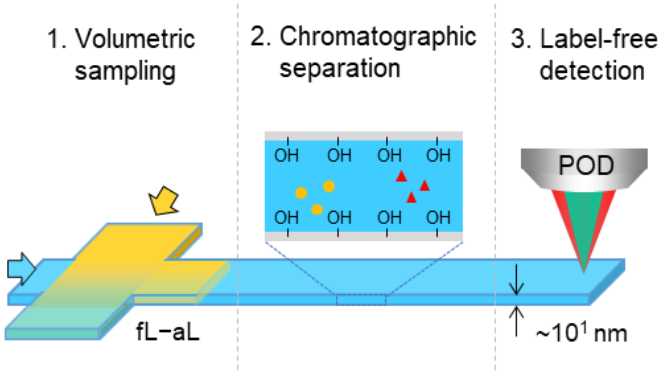


*Figure 5-16. Schematic design of sequential analytical processes for separation analysis in $10^1$ nm channels.*

### 5.4.2 Results and Discussion

*Volumetric Sampling in $10^1$ nm Channel*

First, pressure-driven pinched injection in $10^1$ nm channels was verified. As a test sample, Sudan IV in hexane solution (500 μM) was used to avoid the effect of the electric double layer and unique liquid phenomena. Figure 5-17 shows the time trace of the signal for different loading times ($t_{load}$). As mentioned in section 5.3.1, the injected sample volume can be controlled by changing the loading time. For $t_{load}$=0 sec, no peak signal was observed. For $t_{load}$=0.1 sec, a small peak signal was observed, and signal intensity increased for longer loading time. The broadening and the position shift of the peak signal were observed for a long loading time. Which is explained by the initial sample length. The sample length calculated from the flow velocity and channel size was ~10 μm for $t_{load}$=0.1 s. However, the calculated sample length for $t_{load}$=3 s was ~300 μm, which is the same order as the length of the separation nanochannel. Thus, the effect of the initial sample length was not negligible for long loading time.

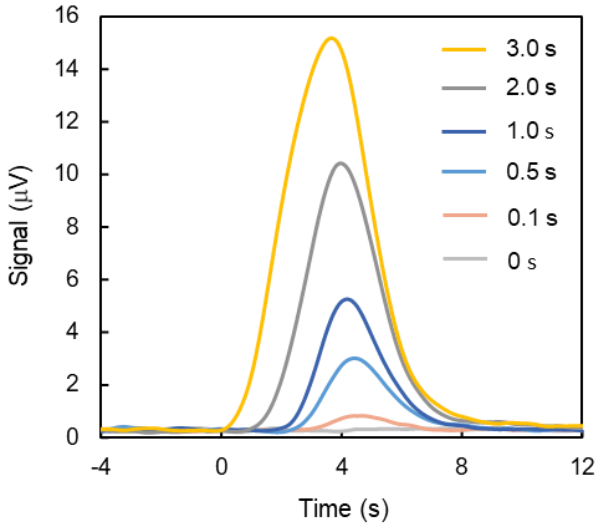


*Figure 5-17. Time trace of the signal for different loading times. The horizontal axis shows the time from the start of injection.*

Figure 5-18 shows the relationship between loading time and the area of the peak signal. The predicted peak area and injected sample volume were calculated by the same procedure as shown in section 5.3.2. The area of peak signal linearly increased for loading time, and experimental results were almost consistent with the predicted values. The injected sample volume was 360±80 aL for $t_{load}$=0.1 s and 25±2 fL for $t_{load}$=3 s. Thus, the volumetric injection of the aL−fL sample in $10^1$ nm channels was demonstrated by pressure-driven pinched injection.

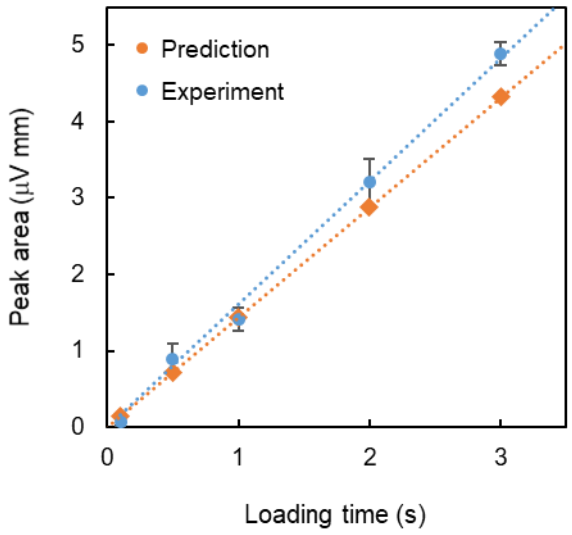


*Figure 5-18. Loading time versus area of peak signal.*

*Separation analysis in $10^1$ nm Channel*

Finally, a series of operations for separation analysis was demonstrated in $10^1$ nm channels. As a test sample, the mixture of Sudan IV (80 μM) and Sudan Orange G (3.1 mM) in a hexane solution was used. The loading time was set to 4 s, and the calculated injected sample volume was 25 fL. These values were determined based on the detection performance of the POD. The result of chromatographic separation is shown in Fig. 5-19. Femtoliter sample injection, chromatographic separation, and label-free detection of two types of non-fluorescent molecules were successfully realized in $10^1$ nm channels within 30 seconds. Thus, the proof-of-concept of $10^1$ nm fluidic devices by nanofluidic circuit and pressure-driven fluidic control was demonstrated for the first time.

The dotted line in Fig. 5-19 shows the start of the injection. In this experiment, the rise of signal for Sudan IV was observed before switching the pressure. The result suggests that part of the sample reached the detection region during sample loading. The

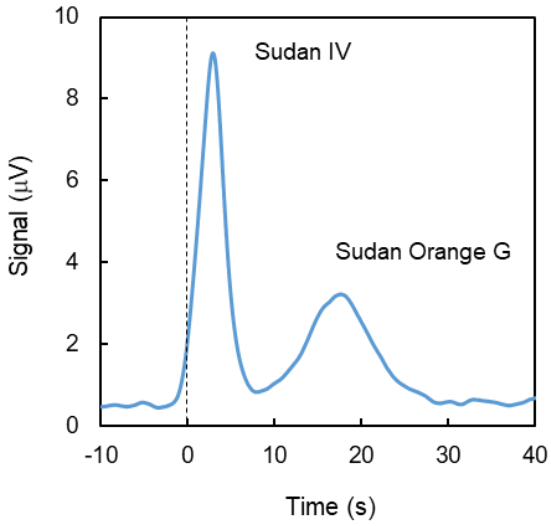


*Figure 5-19. Chromatogram of Sudan IV and Sudan Orange G in hexane solution for a 90-nm deep channel.*

calculated flow velocity at sample loading was 85 μm/sec for Sudan IV and 14μm/sec for Sudan Orange G. Therefore, the calculated initial sample length was 340 μm for Sudan IV and 60 μm for Sudan Orange G without considering the effects of diffusion. Thus, the sample was already separated during sample loading due to the long loading time. These separated samples were further separated after switching the pressure and detected by the POD.

Although accurate evaluation of separation performance was difficult in this study due to the above two-step separation, the theoretical plate height for Sudan Orange G was calculated without considering initial band variance and separation during sample loading. The Van Deemter plot is shown in Fig. 5-20. The horizontal axis is the flow velocity after switching the pressure. The theoretical plate height is inversely proportional to the flow velocity, consistent with the theory of nanochannel chromatography. The minimum theoretical plate height was 16 μm for a flow velocity of 0.11 mm/s. In the current experimental condition, the separation performance is limited by the low flow velocity derived from a large pressure drop of $10^1$ nm channels. A high-pressure fluidic control system is necessary for further advancement of $10^1$ nm fluidic separation analyses.

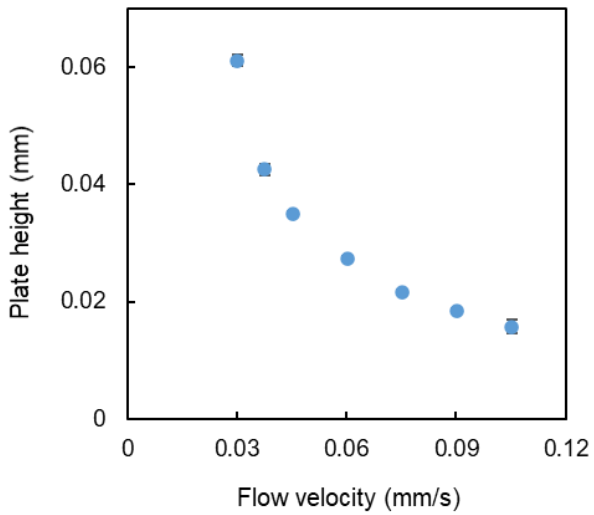


*Figure 5-20. Plate height versus flow velocity (Van Deemter plot) for Sudan Orange G in hexane solution.*

## 5.5 Summary

In this chapter, a proof-of-concept for $10^1$ nm fluidic devices was demonstrated for the first time. First, the POD was applied to ELISA and normal-phase chromatography in $10^2$ nm channels. ELISA was successfully performed in 800 nm wide and 700 nm deep channels, and CRP was quantified with the LOD of 7.0 μg/mL, corresponding to 140 molecules. Normal-phase chromatography was demonstrated in 800 nm wide and 300 nm deep channels, and two non-fluorescent dyes were successfully separated and detected. The LOD was 5.4 zmol (3300 molecules), approximately 50 times improvement for the conventional photothermal detection method. Finally, separation analysis in $10^1$ nm channels was demonstrated by the integration of pressure-driven pinched injection, normal-phase chromatography, and label-free detection by the POD. The experimental results will be the first step in the development of $10^1$ nm fluidic devices which provide a novel platform for chemical/biological analyses.

## 5.5 References of Chapter 5


1. Manz, A., Graber, N. & Widmer, H. M. Miniaturized Total Analysis Systems: a Novel Concept for Chemical Sensing. *Sensors Actuators, B Chem.* **1**, 244–248 (1990).
2. Brouzes, E. *et al.* Droplet microfluidic technology for single-cell high-throughput screening. *Proc. Natl. Acad. Sci. U. S. A.* **106**, 14195–14200 (2009).
3. Tokeshi, M. *et al.* Continuous-flow chemical processing on a microchip by combining microunit operations and a multiphase flow network. *Anal. Chem.* **74**, 1565–1571 (2002).
4. Eyer, K., Stratz, S., Kuhn, P., Küster, S. K. & Dittrich, P. S. Implementing enzyme-linked immunosorbent assays on a microfluidic chip to quantify intracellular molecules in single cells. *Anal. Chem.* **85**, 3280–3287 (2013).
5. Ishibashi, R., Mawatari, K., Takahashi, K. & Kitamori, T. Development of a pressure-driven injection system for precisely time controlled attoliter sample injection into extended nanochannels. *J. Chromatogr. A* **1228**, 51–56 (2012).
6. Nakao, T. *et al.* Femtoliter Volumetric Pipette and Flask Utilizing Nanofluidics. *Analyst* **145**, 2669–2675 (2020).
7. Lin, L. *et al.* Micro/extended-nano sampling interface from a living single cell. *Analyst* **142**, 1689–1696 (2017).
8. Shirai, K., Mawatari, K. & Kitamori, T. Extended nanofluidic immunochemical reaction with femtoliter sample volumes. *Small* **10**, 1514–1522 (2014).
9. Yamamoto, K., Morikawa, K., Imanaka, H., Imamura, K. & Kitamori, T. Picoliter enzyme reactor on a nanofluidic device exceeding the bulk reaction rate. *Analyst* **145**, 5801–5807 (2020).
10. Shimizu, H., Mawatari, K. & Kitamori, T. Sensitive determination of concentration of nonfluorescent species in an extended-nano channel by differential interference contrast thermal lens microscope. *Anal. Chem.* **82**, 7479–7484 (2010).
11. Ishibashi, R., Mawatari, K. & Kitamori, T. Highly efficient and ultra-small volume separation by pressure-driven liquid chromatography in extended nanochannels. *Small* **8**, 1237–1242 (2012).
12. Shirai, K., Mawatari, K., Ohta, R., Shimizu, H. & Kitamori, T. A single-molecule ELISA device utilizing nanofluidics. *Analyst* **143**, 943–948 (2018).
13. Nakao, T. *et al.* Cytokine Analysis at Countable Number of Molecules from

Living Single Cell on Nanofluidic Device. *Analyst* **144**, 7200–7208 (2019).
14. Forcisi, S. *et al.* Liquid chromatography-mass spectrometry in metabolomics research: Mass analyzers in ultra high pressure liquid chromatography coupling. *J. Chromatogr. A* **1292**, 51–65 (2013).
15. Xie, F., Liu, T., Qian, W. J., Petyuk, V. A. & Smith, R. D. Liquid chromatography-mass spectrometry-based quantitative proteomics. *J. Biol. Chem.* **286**, 25443–25449 (2011).
16. Vankrunkelsven, S. *et al.* Ultra-rapid separation of an angiotensin mixture in nanochannels using shear-driven chromatography. *J. Chromatogr. A* **1102**, 96–103 (2006).
17. Poppe, H. Mass transfer in rectangular chromatographic channels. *J. Chromatogr. A* **948**, 3–17 (2002).
18. De Bruyne, S. *et al.* Exploring the speed limits of liquid chromatography using shear-driven flows through 45 and 85 nm deep nano-channels. *Analyst* **138**, 6127–6133 (2013).
19. Smirnova, A., Shimizu, H., Pihosh, Y., Mawatari, K. & Kitamori, T. On-Chip Step-Mixing in a T-Nanomixer for Liquid Chromatography in Extended-Nanochannels. *Anal. Chem.* **88**, 10059–10064 (2016).
20. Shimizu, H., Mawatari, K. & Kitamori, T. Femtoliter-scale separation and sensitive detection of nonfluorescent samples in an extended-nano fluidic device. *Analyst* **139**, 2154–2157 (2014).
21. Bai, X. *et al.* Pressure pinched injection of nanolitre volumes in planar micro-analytical devices. *Lab Chip* **2**, 45–49 (2002).
22. Schroeder, V., Savagatrup, S., He, M., Lin, S. & Swager, T. M. Carbon nanotube chemical sensors. *Chem. Rev.* **119**, 599–663 (2019).
23. Hou, X., Guo, W. & Jiang, L. Biomimetic Smart Nanopores and Nanochannels. *Chemi Soc Rev* **40**, 2385–2401 (2011).
24. Zhang, Z., Wen, L. & Jiang, L. Bioinspired smart asymmetric nanochannel membranes. *Chem. Soc. Rev.* **47**, 322–356 (2018).

# Chapter 6. Concluding Remarks

## 6.1 Conclusion

In this thesis, a novel label-free molecule/nanoparticle detection method for $10^1$–$10^2$ nm fluidic devices: photothermal optical diffraction (POD) was developed. Firstly, the detection principle of the POD was proposed, label-free molecule detection in $10^2$ nm channels was verified. Furthermore, the signal generation mechanism was elucidated from several experiments. Next, concentration determination and nanoparticle counting in $10^1$–$10^2$ nm was realized by the POD with high detection performance. Finally, the POD was applied to nanofluidic analytical devices, and separation analysis in $10^1$ nm space was demonstrated by the integration of sequential analytical processes (sampling, chemical processing, and detection) into $10^1$ nm channels.

In chapter 2, photothermal optical diffraction (POD) was developed. First, the detection principle of the POD was proposed, and the experimental setup was constructed. Next, the mechanism of optical diffraction by a single nanochannel was theoretically described and experimentally elucidated. Finally, the detection principle of the POD was verified, and the POD realized non-fluorescent molecule detection in 400 nm wide and deep channels. Furthermore, the signal generation mechanism was precisely investigated and elucidated by several experiments. Thus, a novel photothermal label-free molecule detection method for nanofluidic devices was developed.

In chapter 3, concentration determination in $10^1$–$10^2$ nm channels by the POD was demonstrated for the first time. The POD realized concentration determination of non-fluorescent molecules with the LOD of 2.5 μM, corresponding to 330 molecules (0.55 zeptomol) in the detection volume of 0.23 fL. Furthermore, concentration determination in $10^2$ nm channels at a countable molecular level (LOD: 10 molecules) was realized by utilizing the solvent enhancement effect. Finally, the POD was applied to $10^1$ nm channels,

and concentration determination was demonstrated in 70 nm wide and deep nanochannels with the LOD of 1200 molecules for aqueous solutions and 30 molecules for organic solutions. Thus, ultra-sensitive label-free molecule detection in $10^1$ nm channels was realized by the POD.

In chapter 4, nanoparticle detection and characterization by the counting-mode POD was realized for the first time. First, the detection principle of the counting-mode POD was verified, and experimental conditions were optimized. Next, concentration determination of Au nanoparticle solutions by pulse counting was demonstrated, and almost 100% detection efficiency, calibration-less concentration determination was realized. Furthermore, the size of individual nanoparticles was evaluated based on the height of pulse signals which correlated with absorbance. Finally, 20 and 40-nm Au nanoparticles were classified based on the height of pulse signals. Thus, individual nanoparticle detection and absorption-based classification were realized for the first time by the POD.

In chapter 5, the POD was applied to nanofluidic analytical devices, and a proof-of-concept for $10^1$ nm fluidic devices was demonstrated for the first time. First, the POD was applied to ELISA and normal-phase chromatography in $10^2$ nm channels. ELISA was successfully performed in 800 nm wide and 700 nm deep nanochannels, and C-reactive protein was quantified with the LOD of 7.0 ng/mL, corresponding to 140 molecules. Then, normal-phase chromatography was demonstrated in 800 nm wide and 300 nm deep nanochannels, and two non-fluorescent dyes were successfully separated and detected with the LOD of 5.4 zmol (3300 molecules). Finally, separation analysis in $10^1$ nm channels was demonstrated by the integration of pressure-driven pinched injection, normal-phase chromatography, and label-free detection by the POD.

## 6.2 Future Prospects and Open Problems

### 6.2.1 Scientific Insights of Chemistry and Biology in $10^1$–$10^2$ nm Space

The development of the non-invasive detection methodology for $10^1$ nm space leads to the understanding of chemistry and biology in such ultra-small space. Several unique phenomena of liquid confined in $10^1$–$10^2$ nm space: high proton mobility, low dielectric constant, high viscosity, and ion concentration polarization.[1-4] Further understanding of such phenomena provides insight into biology because there are many such ultra-small spaces in the biological system such as synaptic gaps and extracellular vesicles. Furthermore, $10^1$–$10^2$ nm space enables chemical/biological analyses at a single or countable molecule/nanoparticle level, which is different from bulk and micro spaces in which statistical behavior of ensembles is the target of interest. Although kinetic analyses of single enzymes have been reported so far, the enzymes were immobilized on a surface, and kinetic analyses of single enzyme versus multiple substrates have been investigated.[5] In contrast, $10^1$–$10^2$ nm fluidic devices have the potential to provide an analytical platform for genuine single-molecule kinetic analysis, in which chemical reaction between single molecules in a fluid is investigated in detail. Thus, $10^1$–$10^2$ nm fluidic devices will provide new scientific insights of chemistry and biology, and the POD will contribute these advances as a detection methodology for $10^1$ nm space, although further sensitivity improvement is necessary for single-molecule detection.

### 6.2.2 Chemical/biological Applications in $10^1$–$10^2$ nm Space

In terms of chemical/biological applications, $10^1$–$10^2$ nm space enables various operations and analyses at a single molecule/nanoparticle level by further miniaturizing conventional lab-on-a-chip technologies. For example, a nanofluidic synthesis platform will be realized by combing the POD with the nanofluidic reactor and sorter. Synthesis, online characterization, and selective sorting of individual nanoparticles will boost current trends of synthesized functional nanoparticles such as lipid vesicles and drug delivery carriers. For separation analysis, unique liquid properties and strong analytes/channel surface interaction in $10^1$–$10^2$ nm space have the potential to establish novel chromatographic separation modes that cannot be performed in conventional separation columns.[6,7] For biological analyses, $10^1$–$10^2$ nm space is suitable for single-cell analyses because of chemical processing at ultra-small volume (aL–fL) without sample loss. Furthermore, the integration of analytical processes into $10^1$ nm space leads to further miniaturization of target analytes. As microfluidic devices have targeted μm-scale cell analysis, nanofluidic devices will target nm-scale analytes such as extracellular vesicles. Thus, $10^1$–$10^2$ nm fluidic devices and the POD will enable chemical/biological analyses at unprecedented resolution in terms of both size and sensitivity.

### 6.2.3 Remaining Challenges for the POD

Although chemical/biological analysis in $10^1$–$10^2$ nm channels was demonstrated by the POD, several challenges remain to be solved. First, the detection performance is still insufficient for single-molecule detection. A large background signal is an issue for the further sensitivity improvement of the POD. Since the POD measures minute diffracted light intensity change by photothermal effect, the estimated ratio of photothermal signal and background signal (initial diffracted light intensity) is in the order of $10^{-5}$–$10^{-4}$. Therefore, the detection performance is highly restricted by the fluctuation of the background signal. To overcome this limitation, background-free detection principle such as interference needs to be introduced into the POD.[8]

Another challenge is the expansion of the application range. In this thesis, a visible light laser was applied as an excitation beam. However, the introduction of UV excitation is essential for a wide range of biological applications because DNAs and proteins have absorbance in the UV region. The UV excitation system has already been introduced into conventional photothermal detection methods, and biomolecule detection was realized without labeling.[9,10] Thus, the introduction of UV excitation into POD will provide label-free biomolecule detection in $10^1$–$10^2$ nm space.

## 6.3 References of Chapter 6


1. Fumagalli, L. *et al.* Anomalously low dielectric constant of confined water. *Science.* **360**, 1339–1342 (2018).
2. Li, L., Kazoe, Y., Mawatari, K., Sugii, Y. & Kitamori, T. Viscosity and wetting property of water confined in extended nanospace simultaneously measured from highly-pressurized meniscus motion. *J. Phys. Chem. Lett.* **3**, 2447–2452 (2012).
3. Kim, S. J., Wang, Y. C., Lee, J. H., Jang, H. & Han, J. Concentration polarization and nonlinear electrokinetic flow near a nanofluidic channel. *Phys. Rev. Lett.* **99**, 1–4 (2007).
4. Ahmed, Z., Bu, Y. & Yobas, L. Conductance Interplay in Ion Concentration Polarization across 1D Nanochannels: Microchannel Surface Shunt and Nanochannel Conductance. *Anal. Chem.* **92**, 1252–1259 (2020).
5. Lu, H. P. Single-Molecule Enzymatic Dynamics. *Science.* **282**, 1877–1882 (1998).
6. Wang, X., Kang, J., Wang, S., Lu, J. J. & Liu, S. Chromatographic separations in a nanocapillary under pressure-driven conditions. *J. Chromatogr. A* **1200**, 108–113 (2008).
7. Kato, M. *et al.* Femto liquid chromatography with attoliter sample separation in the extended nanospace channel. *Anal. Chem.* **82**, 543–547 (2010).
8. Kussrow, A., Enders, C. S. & Bornhop, D. J. Interferometric methods for label-free molecular interaction studies. *Anal. Chem.* **84**, 779–792 (2012).
9. Shimizu, H., Takeda, S., Mawatari, K. & Kitamori, T. Ultrasensitive detection of nonlabelled bovine serum albumin using photothermal optical phase shift detection with UV excitation. *Analyst* **145**, 2580–2585 (2020).
10. Hiki, S., Mawatari, K., Hibara, A., Tokeshi, M. & Kitamori, T. UV excitation thermal lens microscope for sensitive and nonlabeled detection of nonfluorescent molecules. *Anal. Chem.* **78**, 2859–2863 (2006).

**List of Abbreviation**

| | |
|---|---|
| μ-TAS | Miniaturized total analysis system |
| PDMS | Polydimethylsiloxane |
| CFCP | Continuous-flow chemical processing |
| MUO | Micro-unit operation |
| LIF | Laser-induced fluorescence |
| SPR | Surface plasmon resonance |
| PTS | Photothermal spectroscopy |
| TLS | Thermal lens spectroscopy |
| TLM | Thermal lens microscope |
| DIC-TLM | Differential interference contrast thermal lens microscope |
| LOD | Limit of detection |
| POD | Photothermal optical diffraction |
| PDS | Photothermal deflection spectroscopy |
| SEM | Scanning electron microscopy |
| TEM | Transmission electron microscopy |
| RPS | Resistive pulse sensing |
| TC | Time constant |
| CV | Coefficient variation |
| NUO | Nano-unit operation |
| ELISA | Enzyme-linked immunosorbent assay |
| APTES | Aminopropyltriethoxysilane |
| VUV | Vacuum ultra-violet |
| PEG | Polyethylene glycol |

| | |
|---|---|
| CRP | C-reactive protein |
| HRP | Horseradish peroxidase |
| TMB | Tetramethylbenzidine |

**List of Related Publications**

*Original Papers*

[1] Y. Tsuyama and K. Mawatari
"Nonfluorescent Molecule Detection in $10^2$ nm Nanofluidic Channels by Photothermal Optical Diffraction"
*Analytical Chemistry*, 91(15), 9741-9746 (2019) [Chapter 2, Chapter 3]

[2] Y. Tsuyama and K. Mawatari
"Characterization of Optical Diffraction by Single Nanochannel for aL-fL Sample Detection in Nanofluidics"
*Microfluidics and Nanofluidics*, 24, 28, 1-8, (2020) [Chapter 2]

[3] Y. Tsuyama and K. Mawatari
"Concentration Determination at a Countable Molecular Level in Nanofluidics by Solvent-Enhanced Photothermal Optical Diffraction"
*Analytical Chemistry*, 92(21), 14366-14372, (2020) [Chapter 3]

[4] Y. Tsuyama and K. Mawatari
"Detection and Characterization of Individual Nanoparticles in a Liquid by Photothermal Optical Diffraction and Nanofluidics"
*Analytical Chemistry*, 92(4), 3434-3439, (2020) [Chapter 4]

[5] Y. Tsuyama, K. Morikawa, and K. Mawatari
"Nanochannel chromatography and photothermal optical diffraction: Femtoliter sample separation and label-free zeptomole detection"
*Journal of Chromatography A*, 1624, 461265, 1-6 (2020) [Chapter 5]

Reviewed Proceedings

[1] Y. Tsuyama, K. Mawatari, and T. Kitamori
"Ultra-sensitive Optical Detection Method of Non-Fluorescent Molecules in Extended-nano Spaces Utilizing Light Diffraction"
*The Proceedings of μTAS 2016*, 1, 1358-1359 (2016)

[2] Y. Tsuyama, K. Mawatari, and T. Kitamori
"Simple and Ultra-sensitive Detection Method of Non-fluorescent Molecules in Extended-nano Spaces Utilizing Light Diffraction: Investigation of Signal Generation Mechanism"
*The Proceedings of μTAS 2017*, 1, 537-538 (2017)

[3] Y. Tsuyama, K. Mawatari, and T. Kitamori
"Simple and Label-Free Ultra-sensitive Concentration Determination Method in $10^1$-$10^2$ nm Space Utilizing Optical Diffraction"
*The Proceedings of μTAS 2018*, 1, 953-954 (2018)

[4] Y. Tsuyama and K. Mawatari
"Label-free Nanoparticle Detection in $10^2$ nm Channel by Utilizing Photothermal Optical Diffraction"
*The Proceedings of μTAS 2019*, 1, 1370-1371 (2019)

[5] Y. Tsuyama, K. Morikawa, and K. Mawatari
"Solvent-enhanced photothermal molecule detection method for nanofluidics and its application to femtoliter normal-phase chromatography"
*The Proceedings of μTAS 2020*, 1, 550-551 (2020)

**Acknowledgment**

I would like to express my great gratitude to Professor Kazuma Mawatari for his guidance and supervision throughout this work, and his sincere advice and criticism on my research. I am also grateful to him for carefully reading and commenting on the revisions of the manuscripts and presentations.

I also would like to express my great gratitude to Prof. Takehiko Kitamori for his useful advice and criticism on my research, and the laboratory management to accomplish the doctoral research.

I am deeply grateful to Prof. Ryo Miyake, Prof. Madoka Takai, Prof. Hiroaki Matsui, and Prof. Kazuhito Tabata for their helpful advice and criticism for the improvement of this thesis. Especially, I would like to express my sincere gratitude to Prof. Matsui for fruitful discussion about optics.

I am also deeply grateful to Prof. Yutaka Kazoe, Prof. Hisashi Shimizu, Prof. Kyojiro Morikawa, and Prof. Ryoichi Ohta for their cooperation and expertise in this research.

I would also like to show my gratitude to Dr. Adelina Smirnova, Dr. Pihosh Yuriy, Dr. Tatsuro Nakao, Dr. Koki Yamamoto, Mr. Yuto Takagi, Mr. Hiroki Sano, Ms. Emi Mori, and Ms. Takako Asaoka for their tremendous help and constant encouragement. I also wish to express my gratitude to all other laboratory members for meaningful discussion and daily exciting conversation.

Finally, I am deeply indebted to my parents and families for their support of my work.

Yoshiyuki Tsuyama

February 2nd, 2021